

30 MAY 2000

# SRI International

---

Final Report • May 2000

## EXPERIMENTAL STUDIES ON SUPERCRITICAL FLOWS

Prepared by:

Gregory W. Faris  
Molecular Physics Laboratory

SRI Project 1970

Contract Number F49620-97-C-0002

MP 00-028

Prepared for:

Air Force Office of Scientific Research  
801 North Randolph Road, Room 732  
Arlington VA 22203-1977

Attn: Dr. Julian Tishkoff

**DISTRIBUTION STATEMENT A**  
Approved for Public Release  
Distribution Unlimited

20000614 067

# REPORT DOCUMENTATION PAGE

AFRL-SR-BL-TR-00-

Public reporting burden for this collection of information is estimated to average 1 hour per response, including the time for reviewing the data needed, and completing and reviewing this collection of information. Send comments regarding this burden estimate or any reducing this burden to Washington Headquarters Services, Directorate for Information Operations and Reports, 1215 Jefferson Davis Highway, Management and Budget, Paperwork Reduction Project (0704-0188), Washington, DC 20503

0202

1. AGENCY USE ONLY (Leave blank)		2. REPORT DATE 14 May 2000		3. REPORT TYPE AND DATES COVERED Final Technical Report	
4. TITLE AND SUBTITLE Experimental Studies on Supercritical Flows				5. FUNDING NUMBERS PE - 61102F PR - 2308 SA - BS C - F49620-97-C-0002	
6. AUTHOR(S) Gregory W. Faris					
7. PERFORMING ORGANIZATION NAME(S) AND ADDRESS(ES) SRI International 333 Ravenswood Avenue Menlo Park, CA 94025				8. PERFORMING ORGANIZATION REPORT NUMBER MP 00-028	
9. SPONSORING / MONITORING AGENCY NAME(S) AND ADDRESS(ES) AFOSR/NA 801 North Randolph Road Room 732 Arlington VA 22203-1977				10. SPONSORING / MONITORING AGENCY REPORT NUMBER	
11. SUPPLEMENTARY NOTES					
12a. DISTRIBUTION / AVAILABILITY STATEMENT Approved for public release; distribution is unlimited				12b. DISTRIBUTION CODE	
<p>Stimulated scattering was performed with infrared lasers at 1064 nm and with a ring dye laser at 532 nm. For the measurements at 1064 nm, a Nd:YAG laser was used as the pump laser and a tunable diode laser was used as the probe laser. With this apparatus stimulated Brillouin and stimulated Rayleigh scattering were observed in hexane and other liquids. These were the first high resolution stimulated scattering performed without a ring dye laser and the first stimulated scattering gain spectroscopy in the infrared to our knowledge. Both electrostrictive and absorptive versions of Brillouin and Rayleigh scattering were obtained. The transition from electrostrictive to absorptive Rayleigh scattering was observed for the first time to our knowledge. The influence of scattered pump light was determined not to be a problem for our measurements. A supercritical cell was designed and constructed capable of operation up to 600 K and 2000 psi. A second generation cell was built to reduce the effects of convection at the windows. The first stimulated scattering measurements in a supercritical fluid were performed.</p>					
14. SUBJECT TERMS Supercritical fluids, stimulated scattering, Raman scattering, Brillouin scattering, Rayleigh scattering.				15. NUMBER OF PAGES 125	
				16. PRICE CODE	
17. SECURITY CLASSIFICATION OF REPORT Unclassified	18. SECURITY CLASSIFICATION OF THIS PAGE Unclassified	19. SECURITY CLASSIFICATION OF ABSTRACT Unclassified		20. LIMITATION OF ABSTRACT UL	

## CONTENTS

OBJECTIVES .....	1
STATUS OF EFFORT .....	1
INTRODUCTION .....	2
Optical Diagnostics for Supercritical Fluids .....	3
Stimulated Scattering .....	4
ACCOMPLISHMENTS / NEW FINDINGS.....	7
Stimulated Scattering Measurements .....	7
Supercritical Cell .....	11
Infrared Stimulated Scattering Measurements .....	12
REFERENCES .....	17
PERSONNEL.....	19
PUBLICATIONS .....	20
INTERACTIONS / TRANSITIONS.....	21
Presentations.....	21
Interactions .....	21
Transitions.....	23
DISCOVERIES .....	24
HONORS / AWARDS.....	24
APPENDIX A — High Spectral Resolution Stimulated Rayleigh / Brillouin Scattering at 1- $\mu$ m, Manuscript in Preparation.	
APPENDIX B — Electrostrictive and Thermal Stimulated Rayleigh Spectroscopy in Liquids, manuscript in preparation.	
APPENDIX C — Two-Photon-Resonant Difference-Frequency Mixing with an ArF Excimer Laser: VUV Generation and Multi-photon Spectroscopy, submitted to J. Opt. Soc. Am. B (2000).	
APPENDIX D — High Power Lyman Alpha Source Generated with an ArF Excimer Laser, Opt. Lett. 23, 204-206 (1998).	
APPENDIX E — Absolute Concentration, Temperature, and Velocity Measurements in a Diamond Depositing dc-Arcjet Reactor, Diamond and Diamond Related Mat., 7, 165 (1998).	
APPENDIX F — Excited State Density Distributions of H, C, C <sub>2</sub> , and CH by Spatially Resolved Optical Emission in a Diamond Depositing dc-Arcjet Reactor, J. Vacuum Sci. and Tech. A., 16 397 (1998).	

## OBJECTIVES

The objectives of this research are to develop stimulated scattering as a diagnostic for supercritical fluids, and use this technique to improve our understanding of fluids in the supercritical state.

The study of supercritical fluids and flows requires new diagnostic techniques. Currently available techniques such as laser-induced fluorescence (LIF) and coherent anti-Stokes Raman scattering (CARS) are complicated by increased molecular interactions, leading to stronger quenching, larger absorption and refractive index, and incomplete understanding of the influence of local conditions on spectroscopic parameters such as linewidths, nonresonant background contributions, and quenching rates. This research shows that stimulated scattering techniques hold great promise for studying supercritical fluids.

## STATUS OF EFFORT

Research was performed on stimulated scattering as a diagnostic for supercritical fluids. New diagnostics are needed in the supercritical regime because low pressure diagnostics do not work well. Using stimulated scattering measurements, thermal, compressional, and compositional properties of supercritical fuels may be determined *in situ*. These techniques should improve our knowledge of fluid properties in the supercritical state.

Stimulated scattering was performed with infrared lasers at 1064 nm and with a ring dye laser at 532 nm. Because of strong absorption by thermally-stressed jet fuel in the visible, measurements at 1064 nm are preferred. For the measurements at 1064 nm, a Nd:YAG laser was used as the pump laser and a tunable diode laser was used as the probe laser. Modifications performed to allow sensitive measurements in the infrared include substitution of an InGaAs detector for a silicon detector and substitution of an optical fiber for the pinhole spatial filter. With this apparatus stimulated Brillouin and stimulated Rayleigh scattering were observed in hexane and other liquids. These were the first high resolution stimulated scattering performed without a ring dye laser and the first stimulated scattering gain spectroscopy in the infrared to our knowledge. Both electrostrictive and absorptive versions of Brillouin and Rayleigh scattering were obtained. The transition from electrostrictive to absorptive Rayleigh scattering was observed for the first time to our knowledge. The influence of scattered pump light was determined not to be a problem for



our measurements. Scattered pump light had been a significant concern because our infrared measurements were performed with 10 times less probe beam power and over four times smaller gain coefficient than previous measurements at 532 nm. A supercritical cell was designed and constructed capable of operation up to 600 K and 2000 psi. Titanium bolts and glass windows were used to avoid leaks associated with differential expansion at high temperatures. A second-generation cell was built to reduce the effects of convection at the windows. The first stimulated scattering measurements in a supercritical fluid were performed.

## INTRODUCTION

Supercritical fuels and mixing are becoming very important for Air Force projects such as advanced air breathing propulsion systems and advanced launch boosters. The relative lack of experience with and understanding of the fluid properties, fluid dynamics and mixing, and chemical kinetics under such conditions requires the development and application of diagnostic techniques that are well suited to characterize the new features and processes that may occur. These techniques are especially important because diagnostic approaches for low pressures cannot be easily adapted to supercritical conditions. This research on stimulated scattering is very well suited to performing diagnostics on supercritical fluids.

Supercritical conditions are important in two significant areas. For air breathing propulsion, increasing demands are being placed on fuel as a coolant for the engine, environmental control systems, electronics, and at high Mach numbers, even the airframe. These cooling needs will heat the fuel into the supercritical phase. Relatively little is known about the properties of fuels in the supercritical regime or the effects of injecting supercritical fuel into subcritical turbines or ramjets. Diagnostics are required to understand the state and properties of the fuel as it is heated and to help understand the effect of these supercritical fuels on engine performance.

For high pressure rocket propulsion, fuel or oxidant may transform from a subcritical to a supercritical state during injection into the combustion chamber. For example, in liquid oxygen-hydrogen rockets, liquid oxygen is injected at supercritical pressure and subcritical temperature and is heated to supercritical temperature in the combustion chamber. Improved diagnostics are required to study the significance of this transcritical mixing on rocket engine performance.

High temperatures create many unusual problems for fuel systems. Thermal cracking changes fuel properties and can produce gums and solids that freeze valves and foul fuel nozzles and heat exchangers. In the supercritical regime, fuels have liquid-like densities and gas-like diffusivities and viscosities. The changing heat load during the flight of advanced aircraft will lead

to widely varying fuel properties during a mission; fuel systems must perform well under all these conditions. In the region of the critical point, destructive flow and pressure instabilities can arise. These various effects demand thorough investigation of proposed fuels and fuel systems under anticipated conditions.

We performed research into new diagnostic techniques that can aid the design and diagnostic evaluation of new supercritical fuel systems for next generation Air Force propulsion systems. These techniques may be used for obtaining a better understanding of supercritical fuels behavior and mixing and for evaluating fuel delivery systems and supercritical fuel mixing. This information is critical in ensuring reliable performance of next generation aircraft.

### **Optical Diagnostics for Supercritical Fluids**

Traditional optical diagnostic techniques can be broadly grouped into two classes:

(1) *hydrodynamic* diagnostics, including schlieren, interferometry, and tracer particles, and  
(2) *molecular* diagnostics, including laser-induced fluorescence (LIF) and coherent anti-Stokes Raman scattering (CARS). Techniques from these two classes will continue to be important in characterizing supercritical mixing and combustion. Hydrodynamic diagnostics will be useful for determining qualitative behavior, gross structure, and mapping of flow fields. Indeed, this type of diagnostic has been used for several studies of supercritical mixing.<sup>1-4</sup>

Molecular diagnostics provide a fine-scale picture of the details of molecular interactions, radical concentrations, local temperature, and velocities. Quantitative interpretation of molecular diagnostics remains a relative weakness, especially in the supercritical regime. Extending techniques such as LIF and CARS to high pressure, multiphase environments is complicated by increased molecular interactions, leading to stronger quenching, larger absorption and refractive index, broader linewidths, and incomplete understanding of the influence of local conditions on spectroscopic parameters such as linewidths, nonresonant background contributions, and quenching rates.

Our research involves a third class of diagnostics techniques that can effectively investigate the unusual conditions expected in supercritical fluids. These diagnostics are based on stimulated Rayleigh, Brillouin, and Raman scattering measurements. We call this class *collective* diagnostics, because they involve collective material motions. These material motions are in turn fundamentally linked to useful and significant underlying physical parameters.

Near the critical point, the gaseous and liquid forms of a fluid become indistinguishable. Such a fluid has unusual properties, such as liquid-like densities and gas-like diffusivities and viscosities, with negligible surface tension, no heat of vaporization, infinite isothermal compress-

ibility, and enhanced chemical reactivity. The large compressibility and thermodynamic equivalence of the liquid and gaseous forms at the same pressure mean that a near-critical fluid is continually condensing and evaporating, which really mean aggregating and dissociating, because there is no actual separation of phases.

This brief description illustrates that near critical and supercritical fluids will experience a range of collective effects that may greatly influence the mechanisms of mixing and combustion. For example, the concept of a droplet is no longer well defined, yet the formation and breakup of droplets remain important to understanding both how a "liquid-like" fuel mixes with a "gas-like" oxidizer and how chemical reactions are modified. The spatial scale of these collective effects should be about 1-1000  $\mu\text{m}$ , much larger than molecules, and difficult to visualize and quantify with path-integrated measurements such as schlieren or interferometry. Thus there is a need for new diagnostic techniques, which is filled by stimulated scattering techniques.

### **Stimulated Scattering**

Rayleigh, Brillouin, and Raman scattering occur commonly as spontaneous scattering. These scattering processes arise from natural oscillation modes of materials and can be used to determine the physical parameters responsible for those oscillations. When these collective modes are excited with a powerful laser, the mode oscillations can be driven so hard that they grow exponentially. This phenomenon is called stimulated scattering. The dominant advantage of stimulated scattering is that the scattered signal can be made arbitrarily large; otherwise, these processes produce extremely weak signals. By using a probe to measure the induced amplification, we can obtain very good quantitative results. This technique is distinct from the stimulated scattering that builds up from noise, in which case quantification is very difficult.

The large signals from stimulated scattering are particularly helpful for investigating Rayleigh and Brillouin scattering, where the weak signals available from spontaneous scattering are difficult to discriminate from background excitation light. Other advantages of stimulated scattering include excellent temporal resolution, and improved spectral resolution and signal-to-noise ratio. Furthermore, the use of two laser beams allows spatial registration and point measurement of local conditions.

With a single detection system, all three processes—Rayleigh, Brillouin, and Raman—can be measured. These processes together provide measurements of a wide range of material properties. Rayleigh scattering provides information on thermal properties, compositional fluctuations, and density; Brillouin scattering on compressional or elastic properties and density; and Raman scattering on chemical and compositional properties, density, and temperature. While

spontaneous Brillouin<sup>5</sup> and Raman<sup>4,6,7</sup> scattering have been applied to supercritical fluids, the use of stimulated scattering for supercritical fluids is new.

The basic arrangement for stimulated scattering measurements is shown in Figure 1. The pump laser sets up an electric polarization oscillating at the characteristic frequency of a scattering mode of the material.<sup>8</sup> For a strong input laser pulse, this polarization acts as a driving force, leading to amplification of both the material oscillation and a scattered optical wave. The optical amplification is detected as a gain or loss on the probe beam. Spatial resolution is determined by the overlap volume of the pump and probe beams.

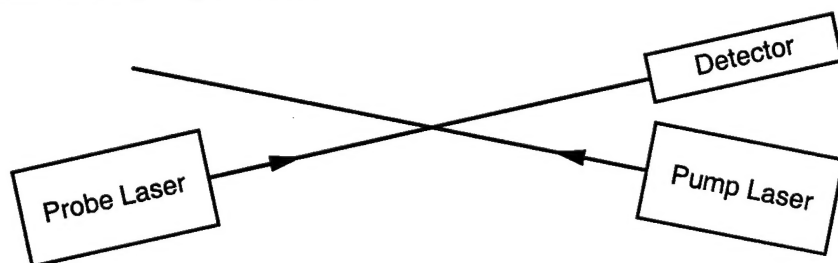


Figure 1. Basic experimental arrangement for stimulated scattering measurements.

When using spontaneous scattering, it can be quite difficult to discriminate the Rayleigh and Brillouin scattered signals against the background excitation light, even under ideal detection conditions. However, the large signals from stimulated scattering processes result in no problems in discriminating against background light. This can be seen in Figures 4, 5, 9, and 10 in the Accomplishments / New Findings section. Even though these measurements are performed within a few GHz (a fraction of  $1 \text{ cm}^{-1}$ ) of the wavelength of the pulsed excitation laser, there is no contribution of scattered background light to the measurement.

Other advantages of stimulated scattering over spontaneous scattering include exceptional temporal resolution, improved spectral resolution (limited by the laser linewidths rather than a spectrometer or interferometer), and very high signal-to-noise ratios. Furthermore, the use of two laser beams allows spatial registration and point measurement of local conditions.

Rayleigh scattering results from refractive index variations due to thermal waves or diffusive density fluctuations and compositional fluctuations. Brillouin scattering results from refractive index variations due to sound waves or traveling density or pressure fluctuations.

In a single-component fluid, the positions, strengths, line shapes, and linewidths in the combined Rayleigh and Brillouin scattering spectrum provide information about the temperature, density, isothermal compressibility  $\chi_T$ , the heat capacity ratio  $c_P/c_V$ , the thermal diffusivity  $D_T$ , the acoustic attenuation coefficient  $\Gamma$ , the adiabatic sound velocity  $c_S$ , and the longitudinal kinematic viscosity or effective mass diffusion coefficient  $D_V$ .<sup>9</sup> Values of these parameters obtained from

stimulated scattering in hexane are given in Table 1 of the Accomplishments / New Findings section. An additional oscillatory mode<sup>10,11</sup> provides information on the exchange of energy between the internal vibrational modes and translational modes. Near the critical point, several of these parameters approach exceptional values, e.g.,  $c_S \rightarrow 0$  and  $\chi_T \rightarrow \infty$ . Critical opalescence is an extreme case of scattering off density fluctuations. One of the first practical uses of spontaneous Brillouin scattering in gases was the investigation of the speed of sound near the critical point.<sup>5</sup>

In two-component fluids, additional information can be obtained from Rayleigh and Brillouin scattering measurements.<sup>12</sup> Even in a nominally well-mixed sample, fluctuations will exist in relative concentration or mole fraction. These fluctuations contribute to scattering that appears as part of the central Rayleigh line, with a linewidth depending on the binary diffusion coefficients  $D_{ij}$ . In addition, the differences in molecular weight between the two components means that there are actually three speeds of sound in a binary mixture: the hydrodynamic or adiabatic speed of sound of the mixture,  $c_S \sim [kT/(m_1\chi_1 + m_2\chi_2)]^{1/2}$ , and the speeds of sound of the individual components,  $\sim [kT/m_1]^{1/2}$  and  $\sim [kT/m_2]^{1/2}$ . Acoustic waves traveling at the component speeds are rapidly damped, but show up as well-defined features at characteristic frequencies in the Brillouin spectrum of the mixture. The linewidths of these features could be used to determine the binary viscosity coefficients,  $\eta_{ij}$ . In principle, such Brillouin scattering measurements in mixtures could be used to determine both the local chemical composition and the rate of chemical mixing.

Raman scattering from molecules is a well established technique in combustion diagnostics. Spontaneous Raman scattering is one of the few optical diagnostic techniques that has been used to date on supercritical fluids.<sup>4,6,7,13</sup> Stimulated Raman scattering can be performed with essentially the same apparatus as the stimulated Rayleigh and Brillouin measurements and provides stronger signals, higher spectral resolution, and better signal-to-noise ratios than spontaneous Raman scattering. Information provided by stimulated Raman scattering includes chemical composition, density, and temperature. Interpretation of stimulated Raman scattering measurements is simpler than for CARS, because the signal is directly proportional to the imaginary part of the third-order nonlinear susceptibility (or to the Raman scattering cross section) rather than to the squared magnitude of the sum of real and imaginary parts of the third-order susceptibility, as is the case for CARS.<sup>14</sup>

The stimulated scattering techniques are widely applicable. We have used stimulated Brillouin and Rayleigh scattering to perform measurements in glasses and crystals<sup>8,14,15</sup> without the requirement of detailed spectroscopic information on these materials. Our supercritical

experiments are aided by long term research at SRI on supercritical fluids, including studies of supercritical water oxidation<sup>16</sup> and supercritical fluid extraction.<sup>17</sup>

The laser requirements for our stimulated Rayleigh and Brillouin measurements are quite modest. The pump beam energy is only  $\sim 40 \mu\text{J}$ , and the probe beam is provided by a diode laser. Thus, stimulated scattering could be used even as an on board monitor of fuel state and properties.

Parameters currently of interest to the Air Force for supercritical fuels include compressibility, sonic velocity, density and phase, and chemical composition.<sup>18</sup> All these parameters can be provided directly by stimulated scattering measurements. Thus stimulated scattering will play a very important role in understanding fuel performance and in diagnosing fuel system performance, critical steps in assuring the performance of next generation aircraft. We are one of only a handful of groups that have performed stimulated Rayleigh and Brillouin experiments, and we are the only group applying these techniques to supercritical fluids.

## **ACCOMPLISHMENTS / NEW FINDINGS**

We applied stimulated Rayleigh and Brillouin scattering to property measurements in pure supercritical fluids. The physical properties that can be measured using this technique are the compressibility (and hence speed of sound and temperature), acoustic damping times or kinematic viscosities, thermal diffusivity, and density. We performed stimulated scattering measurements at both 532 nm and 1064 nm. The measurements at 1064 nm are the first pump-probe stimulated scattering measurements in the infrared to our knowledge. We made experimental modifications to reduce scattered light and improve the signal-to-noise ratios. First- and second-generation supercritical cells were designed, built, and tested. Measurements with high spectral resolution and signal-to-noise ratio were obtained in supercritical fluids. Our work complements well work on optical diagnostics of supercritical fuels being performed at Wright-Patterson using spontaneous Raman and fluorescence measurements.<sup>19</sup>

### **Stimulated Scattering Measurements**

The basic experimental arrangement for stimulated scattering is shown in Figure 1 above. As a pump laser for our stimulated scattering measurements, we use an injection-seeded Nd:YAG laser. This laser was previously modified to allow production of linewidths down to 20 MHz and below.<sup>20</sup> This narrow linewidth is possible through generation of long pulse lengths produced through lowered oscillator gain and pulse lengthening in the amplifier. Narrow linewidths for the pump laser are important for resolving Brillouin features, which can be as narrow as 13 MHz.<sup>8</sup>



The optical properties of jet fuels in the supercritical state are important for this work. In recent experiments, fuels taken to supercritical conditions are found to be black on returning to ambient conditions.<sup>18</sup> Little is known about the optical properties of the fuels while they are still at supercritical conditions. We measured the transmission of thermally stressed JP7 fuel obtained from Tim Edwards of AFRL, Wright-Patterson. The results are shown in Figure 2. Although the thermally stressed fuel is highly absorbing in the visible, it is transparent in the near infrared, where we performed our measurements.

Because stimulated scattering measurements are nonresonant, they can be performed at any wavelength for which the medium is transparent. Previous stimulated Brillouin measurements in solids were performed at 532 nm,<sup>8,15,21</sup> using the second harmonic of an injection-seeded Nd:YAG laser as a pump laser. The probe beam was produced with a cw dye laser pumped by an argon ion laser. Recent advances in diode laser technology allow use of a tunable diode laser as the probe laser. In this case, the fundamental of the Nd:YAG laser is used as the pump laser and measurements are performed at 1064 nm. We chose to use 1064 nm because of the lower absorption in thermally stressed fuel, the lower operating costs compared with the argon laser, and the reduced time required for keeping the ring dye laser in good operation. Operation at 532 nm has the advantage of higher gain coefficients and higher probe beam powers.

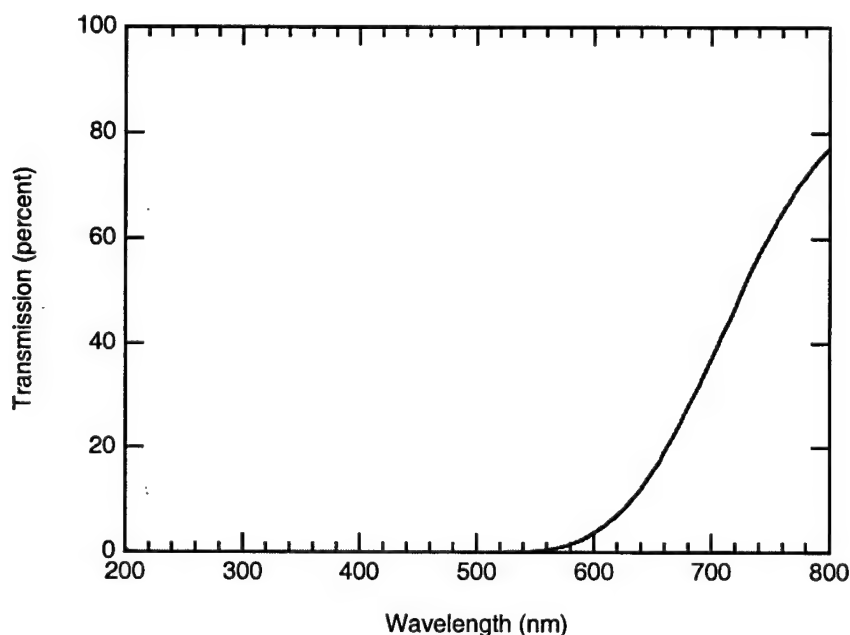


Figure 2. Transmission through 1 cm of JP7 fuel, thermally stressed to 1200° F.

We purchased a tunable diode laser from Environmental Optical Sensors Inc. (EOSI, since acquired by Newport Corporation), which had previously produced lasers at the required wavelength. However, EOSI had considerable difficulty producing a laser for us. The first two lasers EOSI sent ceased functioning prematurely, and considerable delays were encountered before receiving a third laser.

To maintain progress on our research program while waiting for the diode laser, we performed measurements at 532 nm, using the apparatus shown in Figure 3. We borrowed an argon ion laser and ring dye laser from another researcher in our laboratory. A wavemeter (New Focus) was used to monitor the probe laser wavelength. Both lasers were focused through the sample using effective focal lengths of about 2 m. To prevent saturation of the detector, the chopper wheel reduces the dye laser power except during a short period corresponding to the laser pulse. The spatial filter (lens and pinhole aperture) reduces the amount of scattered pump laser light incident on the detector.

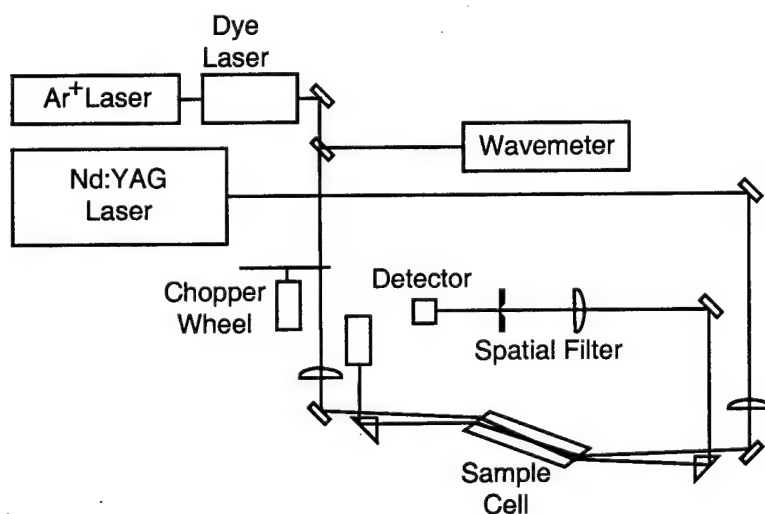


Figure 3. Apparatus for stimulated scattering at 532 nm.

With this laser and the second harmonic of the Nd:YAG laser, we obtained stimulated Brillouin spectra such as that shown for methanol in Figure 4. There are two peaks in the spectrum. The positive peak at the left is a gain peak, which occurs when energy is transferred from the pump laser to the probe (dye) laser. The negative peak at the right is a loss peak, which occurs when energy is transferred from the probe laser to the pump laser. Information that can be extracted from these peaks includes the overall density (from the peak height), the acoustic velocity or compressibility (from the peak separation), and the acoustic lifetime or kinematic viscosity (from the peak widths).



Several experimental improvements were required to obtain a stimulated Rayleigh scattering signal at 532 nm. The dye laser has large intensity fluctuations both near 1 MHz and near 80 MHz. These were reduced by using low- and high-pass filters that transmitted most of the frequency components in the pump pulse. Amplitude fluctuations associated with jitter of the pump pulse were reduced by triggering the boxcar used for data acquisition from the laser light rather than from the Q-switch trigger pulse. The data acquisition electronics were configured to perform single-shot measurements to allow subtraction of the scattered pump laser light on a shot-by-shot basis. Following the signal-to-noise improvements, we were able to observe stimulated Rayleigh scattering in methanol. This peak is shown in Figure 5 along with a fit to the appropriate theoretical lineshape (the imaginary part of a complex Lorentzian function).

From our measurements at 532 nm, we obtained enough information to begin design of a cell for supercritical experiments. To reduce the influence of scattered pump light, we used a cell that is long enough to prevent overlap of the pump and probe beams on the windows, and has tilted windows.

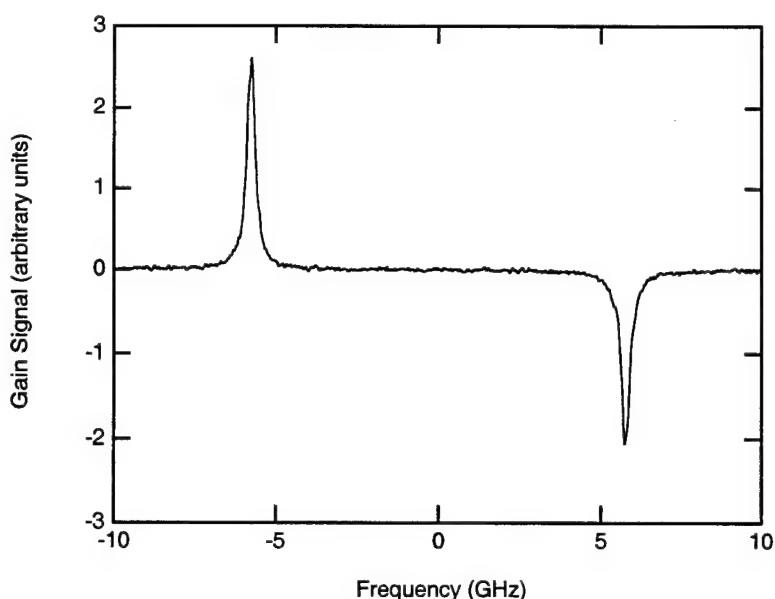


Figure 4. Stimulated Brillouin scattering spectrum for methanol.

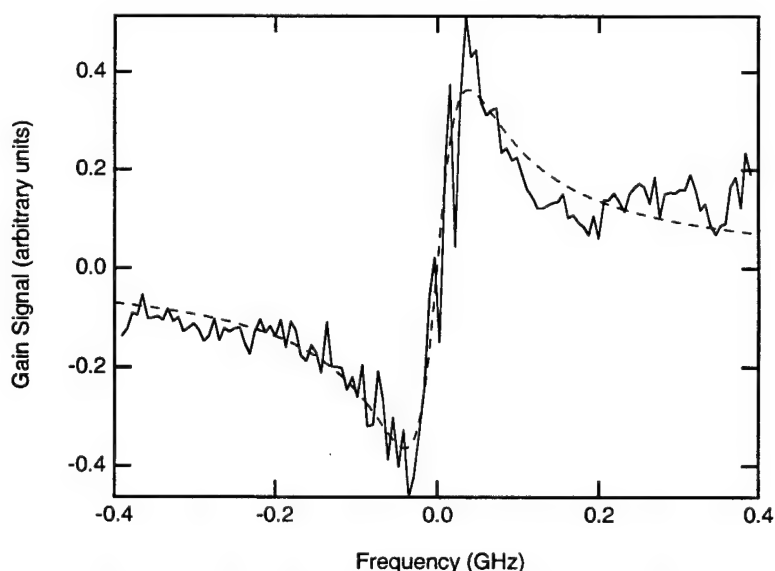


Figure 5. Stimulated Rayleigh spectrum for methanol.

## Supercritical Cell

We designed and built a cell for experiments at high pressure and temperature, up to 500 K and 2000 psi. The cell design and high pressure system are shown in Figures 6 and 7. In designing this cell, we drew on information gained from conversations with Tim Edwards and Chris Bunker of AFRL Wright-Patterson in their work on high pressure/high temperature systems. The cell volume was kept small to minimize the risk from the failure of the graphite foil used to seal the windows. At supercritical conditions, any hydrocarbons leaking from the cell causes a fire because the temperatures exceed the autoignition temperature. For our cell design, we used a heater that totally encloses the cell to maintain uniform conditions throughout the cell. The initial design used steel bolts and fused silica windows. However, the differential expansion of the bolts and the windows resulted in leaks through the graphite foil seals at high temperatures. We substituted titanium bolts and glass windows, which have very similar thermal expansion coefficients, and the cell was tested to 500 K and 2000 psi simultaneously without leaks.

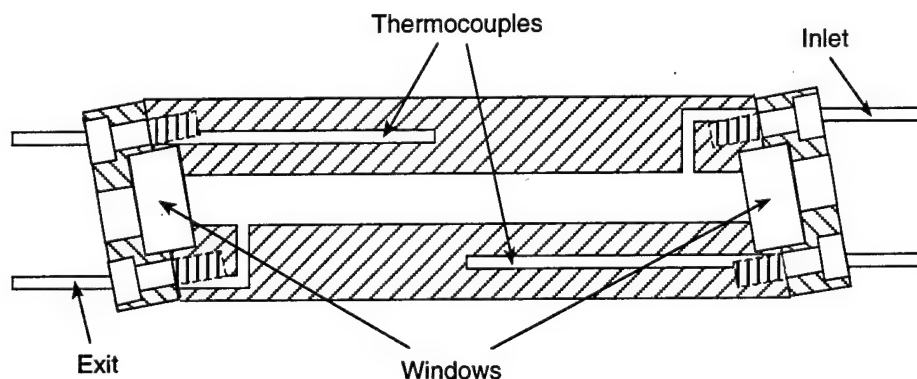


Figure 6. Design for high pressure/high temperature cell.

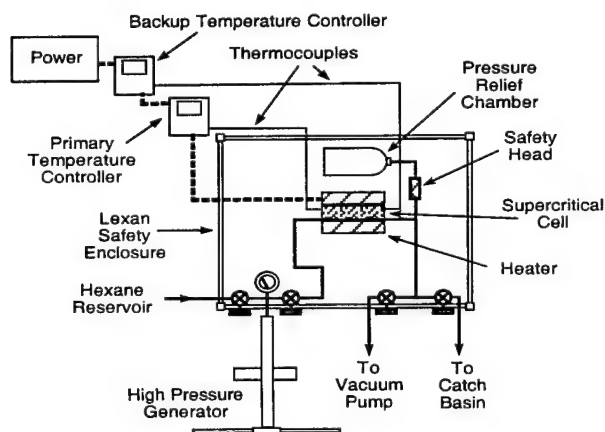


Figure 7. Overall high pressure system.

## Infrared Stimulated Scattering Measurements

During construction of the supercritical cell, we received a functioning tunable diode laser, which provides 8 mW at 1064 nm. We substituted this laser for the ring dye laser and reconfigured the experiment to operate at 1064 nm as shown in Figure 8. Although the experiments we had performed at 532 nm greatly aided our work at 1064 nm, several changes were required. The 8-mW power was less than the approximately 100 mW we had using the ring dye laser. In addition, the silicon detector we used to detect the probe signal had a poor sensitivity at 1064 nm.

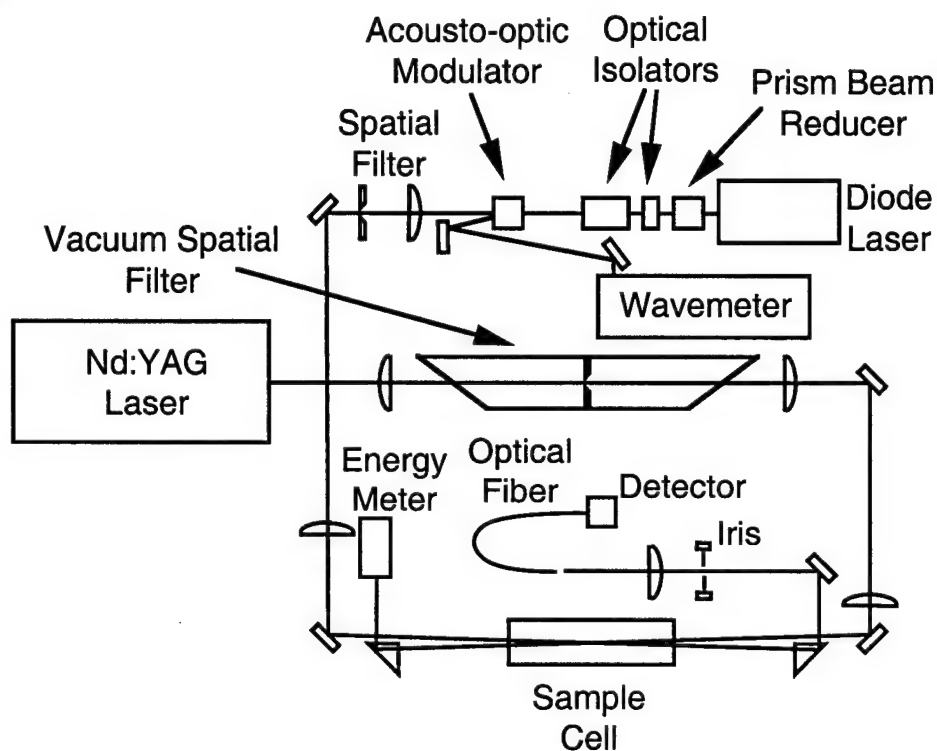


Figure 8. Apparatus for stimulated Rayleigh and Brillouin scattering at 1064 nm.

To obtain improved detection sensitivity for the 1064 nm diode laser, we substituted an InGaAs detector for the silicon detector used at 532 nm. InGaAs has a larger capacitance per unit area than silicon. To obtain comparable time response, we had to substitute a 0.1-mm-diameter InGaAs detector for the 2.54-mm-diameter silicon detector. The silicon detector had been large enough to detect all the probe beam light when placed directly behind the pinhole used to exclude scattered pump light, but the InGaAs detector was too small to collect all the probe light in this manner and too large to act as a spatial filter in place of the pinhole. To remedy this situation, we replaced the pinhole with an optical fiber, which could then be coupled directly to the InGaAs detector. This made alignment easier than it had been using the pinhole and silicon detector.

Because of the lower laser power, it was not necessary to use a chopper wheel for measurements at 1064 nm.

The diode laser was more sensitive to scattered pump light than the dye laser, and amplitude oscillations were produced even with an optical isolator placed in front of the diode laser. To reduce these effects, we added a second optical isolator, added a spatial filter to the probe beam, and added apertures to the probe and pump beams on either side of the fluid cell.

With these modifications, we obtained stimulated spectra using the tunable diode laser. An example of a stimulated Rayleigh-Brillouin spectrum in hexane is shown in Figure 9. This spectrum has three peaks—a double-peaked Rayleigh peak centered at the frequency of the incident laser beam and two Brillouin peaks shifted above and below the incident laser frequency by an amount proportional to the speed of sound. To our knowledge, these are the first stimulated scattering spectra taken without using a single-mode dye laser. The most significant improvement is that the diode laser has much less amplitude noise than the dye laser. Properties extracted from these measurements are summarized in Table 1.

A special feature of stimulated scattering measurements at 1064 nm is the large stimulated Rayleigh peak, which is due to the presence of stimulated thermal scattering. Electrostrictive and absorptive (thermal) effects are two primary mechanisms for the coupling between the electric field of light and the materials fluctuations responsible for the scattering—acoustic waves for Brillouin scattering and non-propagating entropy waves for Rayleigh scattering.<sup>22</sup> The electrostrictive effect (the force produced by the electric field through the linear polarizability) produces stimulated scattering in the absence of absorption. With absorption, thermal forces produce new forms of stimulated scattering.

Liquids containing hydrogen atoms typically display absorption due to overtone or combination bands of the OH or CH stretch vibrations at 1064 nm. This absorption causes significant changes in the stimulated Rayleigh and stimulated Brillouin spectra as compared with measurements performed in the visible spectral region (such as in Figure 4), where many liquids have no absorption. For pure electrostrictive scattering, stimulated Rayleigh scattering is typically on the order of 100 times smaller than stimulated Brillouin scattering, and extremely difficult to observe. However, with thermal effects, the stimulated Rayleigh scattering can become larger than the stimulated Brillouin scattering. This allows the stimulated Rayleigh peak to be easily observed at 1064 nm. We have also observed electrostrictive stimulated Rayleigh scattering at 1064 nm, and the transition from electrostrictive to thermal Rayleigh scattering, in which case the two types of scattering can entirely cancel.

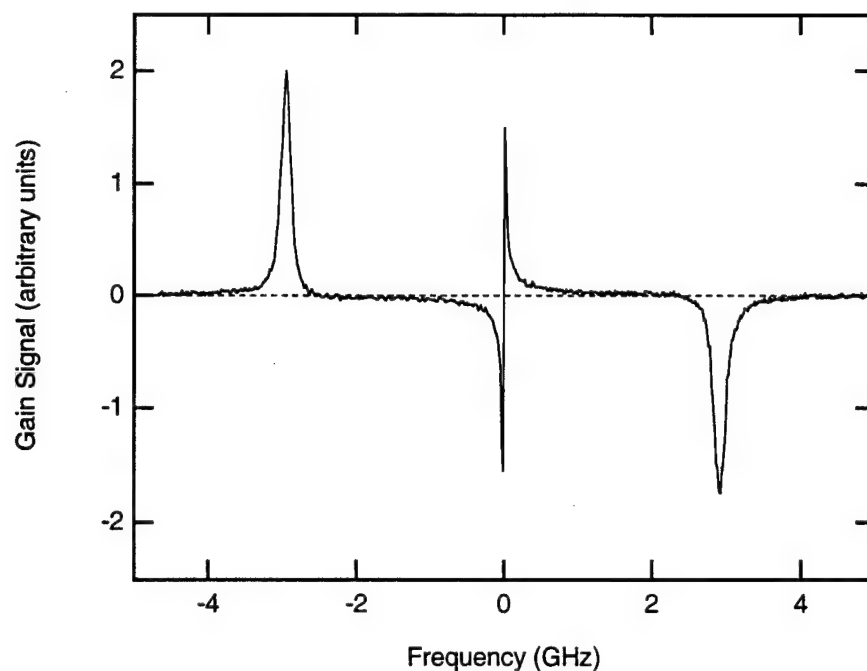


Figure 9. Stimulated Rayleigh and Brillouin spectrum for hexane.

Table 1. Properties measured in hexane using stimulated Rayleigh and Brillouin scattering.

Brillouin shift	2.91 GHz
Brillouin width	151 MHz
Rayleigh width	7.9 MHz
Acoustic damping time	1.06 ns
Acoustic velocity	1125 m/s
Acoustic attenuation coefficient	$8.4 \times 10^5 \text{ m}^{-1}$
Effective mass diffusion coefficient	$7.1 \times 10^{-6} \text{ m}^2/\text{s}$
Isentropic compressibility	$1.2 \times 10^{-9} \text{ m}^2/\text{N}$
Thermal diffusivity	$1.2 \times 10^{-7} \text{ m}^2/\text{s}$

We had been concerned that scattered pump light would be a significant problem for measurements with the diode laser. The diode laser had about 10 times less power than the dye laser, and the gain coefficient was over 4 times smaller at 1064 nm than at 532 nm. However, we found that the scattered light was almost insignificant for our measurements at 1064 nm, primarily

due to the steps we had taken to reduce scattered light for 532 nm, the improved spatial filtering provided by the fiber, the lower noise of the diode laser (which allowed measurement of smaller stimulated gains, or smaller pump energies), and the generally decreasing trend in the amount of scatter at longer wavelengths. This is very good news because we expected scattered pump light to be the primary obstacle to performing measurements in the infrared.

When operating the cell at high temperatures, we found that convection near the windows caused beam wander. This made measurements difficult, particularly in the region of the critical point. To avoid these effects, we produced a second-generation cell. Having found that scattered light was less of a problem at 1  $\mu\text{m}$ , we made a shorter cell with the windows normal to the cell rather than tilted as before. This cell had a total internal length of 2.5 cm. A small tilt of the entire cell was sufficient to reduce scattered light to required levels. The shorter cell could be more evenly heated than the long cell, reducing convection. To further reduce convection, aluminum spacers were placed between the ends of the cell and the end of the heater, and insulating end plates were placed on the ends of the oven.

Figure 10 shows an example of stimulated scattering performed at 200°C and 630 psi. Our measurements are the first stimulated Rayleigh and stimulated Brillouin spectra taken at supercritical conditions to our knowledge. Note that we are still able to obtain measurements at a high signal-to-noise ratio at these conditions. Also shown in Figure 10 are fits of theoretical lineshapes to the data and the electrostrictive and thermal portions of those fits. Note that the signal data show an asymmetry in the Brillouin (outer) peaks. This asymmetry is produced by the imaginary Lorentzian lineshape of the thermal stimulated Brillouin peak. Stimulated thermal Brillouin and Rayleigh scattering is caused by the moderate absorption of the Nd:YAG fundamental wavelength in organic liquids. Without the thermal effects, the stimulated Rayleigh peak would be extremely small and difficult to measure.

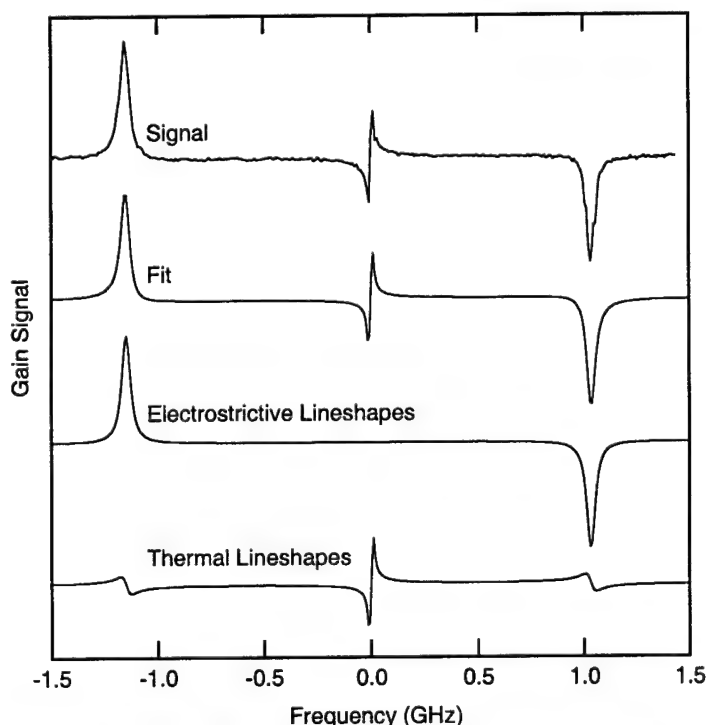


Figure 10. Stimulated Rayleigh and Brillouin spectrum for hexane at 200°C and 630 psi.

We have shown that stimulated Brillouin and Rayleigh scattering is a robust and precise technique for performing measurements in supercritical fluids. This work forms an excellent foundation for future studies of supercritical fluids.

## REFERENCES

1. J. A. Newman and T. A. Brzustowski, "Behavior of a liquid jet near the thermodynamic critical region," AIAA J. **9**, 1595-1602 (1971).
2. R. D. Woodward, D. G. Talley, T. J. Anderson, and M. Winter, "Shadowgraphy of transcritical cryogenic fluids," presented at 6th Annual Penn State PERC Symposium, NASA Lewis Research Center, Cleveland, OH, 1994.
3. W. Mayer and H. Tamura, "Flow visualization of supercritical propellant injection in a firing LOX/GH<sub>2</sub> rocket engine," presented at 31st AIAA/ASME/SAE/ASEE Joint Propulsion Conference & Exhibit, San Diego, CA, 1995.
4. R. D. Woodward and D. G. Talley, "AIAA 96-0468, Raman imaging of transcritical cryogenic propellants," presented at 34th Aerospace Sciences Meeting & Exhibit, Reno, NV, 1996.
5. R. W. Gammon, H. L. Swinney, and H. Z. Cummins, "Brillouin scattering in carbon dioxide in the critical region," Phys. Rev. Lett. **19**, 1467-1469 (1967).
6. M. S. Brown and R. R. Steeper, "CO<sub>2</sub>-based thermometry of supercritical water oxidation," Appl. Spectrosc. **45**, 1733-1738 (1991).
7. W. Kohl, H. A. Lindner, and E. U. Franck, "Raman spectra of water to 400°C and 3000 bar," Ber. Bunsenges. Phys. Chem. **95**, 1586-1593 (1991).
8. G. W. Faris, L. E. Jusinski, and A. P. Hickman, "High-resolution stimulated Brillouin gain spectroscopy in glasses and crystals," J. Opt. Soc. Am. B **10**, 587-599 (1993).
9. B. J. Berne and R. Pecora, *Dynamic Light Scattering* (John Wiley & Sons, New York, 1976).
10. R. D. Mountain, "Spectral distribution of scattered light in a simple fluid," Rev. Modern Phys. **38**, 205-214 (1966).
11. W. S. Gornall, G. I. A. Stegeman, B. P. Stoicheff, R. H. Stolen, and V. Volterra, "Identification of a new spectral component in Brillouin scattering of liquids," Phys. Rev. Lett. **17**, 297-299 (1966).
12. R. P. C. Schram, G. H. Wegdam, and A. Bot, "Rayleigh-Brillouin light-scattering study of both fast and slow sound in binary gas mixtures," Phys. Rev. A **44**, 8062-8071 (1991).
13. T. Edwards, "AIAA 93-0807, USAF supercritical hydrocarbon fuels interests," presented at 31st Aerospace Sciences Meeting & Exhibit, Reno, NV, 1993.
14. G. W. Faris, "Brillouin gain spectroscopy in glasses and crystals," in *Applied Laser Spectroscopy*, Wolfgang Demtröder and Massimo Inguscio, Eds. (Plenum Press, New York, 1990), pp. 307-312.
15. G. W. Faris, L. E. Jusinski, M. J. Dyer, W. K. Bischel, and A. P. Hickman, "High-resolution Brillouin gain spectroscopy in fused silica," Opt. Lett. **15**, 703-5 (1990).
16. D. S. Ross and I. Jayaweera, "Conversions of organic material in hydrothermal media," presented at American Chemical Society Meeting, 1994.
17. S. Ventura, G. Hum, and S. Narang, Supercritical CO<sub>2</sub> extraction of porous absorbants, GRI report , (1992).



18. T. Edwards, personal communication (1996).
19. C. E. Bunker, J. R. Gord, and K. D. Grinstead, Jr., "Spectroscopic investigations of high-temperature, high-pressure model aviation fuels," presented at Symposium on Structure of Jet Fuels V, The Division of Petroleum Chemistry, American Chemical Society, Boston, MA, 1998.
20. G. W. Faris, M. J. Dyer, and W. K. Bischel, "Laser linewidth narrowing induced by amplifier gain saturation," *Opt. Lett.* **19**, 1529-1531 (1994).
21. G. W. Faris, M. J. Dyer, and A. Peet Hickman, "Transient effects on stimulated Brillouin scattering," *Opt. Lett.* **17**, 1049-1051 (1992).
22. W. Kaiser and M. Maier, "Stimulated Rayleigh, Brillouin, and Raman spectroscopy," in *Laser Handbook*, F. T. Arecchi and E. O. Schulz-Dubois, Eds. (North-Holland, Amsterdam, 1972), Vol. 2, pp. 1077-1150.

## **PERSONNEL**

The following personnel participated in the research under support by this contract:

Gregory W. Faris, Research Physicist, principal investigator and lead experimentalist.

Martina Gerken, International Fellow, experimentalist.

Yihong Chen, Postdoctoral Fellow, experimentalist.

Christian Jirauschek, International Fellow, experimentalist.

These students performed research on this project under support from the Research Experiences for Undergraduates program of the National Science Foundation:

DaNel Hogan, Undergraduate Student, experimentalist.

Elizabeth M. Jeffrey, Undergraduate Student, experimentalist.

## PUBLICATIONS

The following publications acknowledge this contract:

- G. W. Faris, M. Gerken, C. Jirauschek, D. Hogan, and Y. Chen, "High spectral resolution stimulated Rayleigh / Brillouin scattering at 1- $\mu$ m," manuscript in preparation.
- C. Jirauschek, E. M. Jeffrey, and G. W. Faris, "Electrostrictive and Thermal Stimulated Rayleigh Spectroscopy in Liquids," manuscript in preparation.
- C. Jirauschek and G. W. Faris, "Stimulated Rayleigh and Brillouin scattering in supercritical fluids," manuscript in preparation.
- G. W. Faris, S. A. Meyer, M. J. Dyer, and M. J. Banks, "Two-Photon-Resonant Difference-Frequency Mixing with an ArF Excimer Laser: VUV Generation and Multi-photon Spectroscopy," submitted to J. Opt. Soc. Am. B (2000).

The following publications are from research supported by the previous contract and were published after the end of the contract:

- W. Juchmann, J. Luque, and J. B. Jeffries, "Atomic Hydrogen Concentration in a Diamond Depositing dc-Arcjet Determined by Calorimetry," J. Appl. Phys. **81**, 8052 (1997).
- S. A. Meyer and G. W. Faris, "High Power Lyman Alpha Source Generated with an ArF Excimer Laser," Opt. Lett. **23**, 204-206 (1998).
- W. Juchmann, J. Luque, J. Wolfrum, and J. B. Jeffries, "Absolute Concentration, Temperature, and Velocity Measurements in a Diamond Depositing dc-Arcjet Reactor," Diamond and Diamond Related Mat., **7**, 165 (1998).
- J. Luque, W. Juchmann, E. A. Brinkman, and J. B. Jeffries, "Excited State Density Distributions of H, C, C<sub>2</sub>, and CH by Spatially Resolved Optical Emission in a Diamond Depositing dc-Arcjet Reactor," J. Vacuum Sci. and Tech. A., **16** 397 (1998).

## INTERACTIONS / TRANSITIONS

### PRESENTATIONS

The following presentations were made on research supported by this contract or the previous contract:

- Scott A. Meyer and Gregory W. Faris, "Phase Matching Effects on VUV Generation near Lyman Alpha," Paper MGG2 presented at the Optical Society of America Annual Meeting, 13th Interdisciplinary Laser Science Conference, Long Beach, California, 12-17 October 1997.
- G. W. Faris, "Experimental Studies on Supercritical Fluids," presented at the ARO/AFOSR Contractor's Meeting in Chemical Propulsion, Long Beach, California, 29 June - 1 July 1998.
- D. Hogan and G. W. Faris, "Stimulated Brillouin and Rayleigh Scattering in Liquids," Paper ThBBB7 presented at the Optical Society of America Annual Meeting, 14th Interdisciplinary Laser Science Conference, Baltimore, Maryland 4-9 October 1998.
- Gregory W. Faris, Martina Gerken, and DaNel Hogan, "Development of Stimulated Scattering as a Diagnostic for Supercritical Fluids," Paper CTuH4 presented at Conference of Lasers and Electro-Optics / Quantum Electronics and Laser Science Conference (CLEO/QELS), Baltimore, Maryland, 23-28 May 1999.
- Gregory W. Faris, Martina Gerken, DaNel Hogan, Elizabeth Jeffrey, and Yihong Chen, "Stimulated Scattering as a Diagnostic for Supercritical Fluids," Paper TuXX49 presented at the Optical Society of America Annual Meeting, 15th Interdisciplinary Laser Science Conference, Santa Clara, California, 26-30 September 1999.

### INTERACTIONS

The following interactions occurred at the AFOSR/ARO contractors meeting in Chemical Propulsion, Bar Harbor, Maine, 13-16 June 1999:

Tim Edwards, supercritical fuels, diagnostic requirements, and supercritical cells.

Mel Roquemore, miscellaneous research on combustion and fuels.

Tom Jackson, high pressure and hypersonic diagnostics.

Irv Glassman, supercritical fluids

Med Colket, combustion chemistry

Marshal Long, laser diagnostics, laser sources

Werner Dahm, vortices

Paul Dimotakis, turbulence, presentation techniques

Hal Calcote, combustion

Mitch Smooke, combustion diagnostics

Stephen Pope, combustion

Ed Law, combustion chemistry

Gerry Faeth, combustion

Norman Kurnit, Los Alamos, stimulated Brillouin scattering, May 1999

Mark Skeldon, U. Rochester, stimulated Rayleigh scattering, May 1999

The following interactions occurred at the AFOSR/ARO contractors meeting in Chemical Propulsion, Long Beach, California, 29 June - 1 July 1998.

Tim Edwards, supercritical fuels, diagnostic requirements, and supercritical cells.

Mel Roquemore, miscellaneous research on combustion and fuels.

Tom Jackson, high pressure and hypersonic diagnostics.

Irv Glassman, supercritical flow cells, carbon structures

Yaw Yeboah, supercritical cells and diagnostics

Pablo Debenedetti, supercritical mixtures

Doug Talley, supercritical diagnostics

Jerry Seitzman, laser diagnostics,

Michael Winter, diagnostics and sensors

Med Colket, combustion chemistry

Peter DeBarber, diagnostics

Bob Santoro, absorption spectra of organics

Ron Hanson, diagnostics

Marshal Long, tomography

Ian Kennedy, diagnostics,

Nina Bergan French (Sky Plus) and Steve Priebe (INEL), laser diagnostics, environmental monitoring various dates 1998.

The following interactions occurred during a visit to Wright-Patterson AFB on June 20, 1997:

Tim Edwards, discussions on supercritical fuels and diagnostic requirements.

Mel Roquemoire, miscellaneous research on combustion and fuels.

Jim Bort, time-resolved diagnostics, experiments on supercritical fluids.

The following interactions occurred at the AFOSR contractors meeting, Ohio Aerospace Institute, Cleveland, Ohio, June 17-19, 1997:

Pablo Debenedetti, Princeton University, supercritical fluids.

Robert Dibble, UC Berkeley, optical tomography.

Galen King, Purdue University, time-resolved diagnostics.

Larry Rahn, Sandia National Laboratories, combustion research.

Robert Lucht, combustion research.

Tim Edwards, Wright Laboratories, supercritical research.

Jim McDaniels, University of Virginia, hypersonic research.

Hal Calcote, Aerochem, soot, combustion.

Robert Santoro, Penn State, soot, combustion research.

Frederick Gouldin, Cornell University, optical tomography.

Med Colket, combustion research.

Paul Dimotakis, turbulent combustion.

Irvin Glassman, Princeton University, combustion research.

Ian Kennedy, UC Davis, nanoparticles.

Ingrid Wysong, Phillips Laboratory, telephone conversations on measurements in supercritical fluids and plasma propulsion (1997).

## TRANSITIONS

Performer: Dr. G. W. Faris, SRI International, 650 859 4131

Customer: Dr. Surendra Sharma, NASA Ames Research Center, 650 604 3432

Result: VUV generation using Raman-shifted ArF laser

Application: Measurement of oxygen concentrations for electric arc shock tube experiments for high speed aerodynamics research and development.

Customer: Tim Edwards, AFRL Wright Patterson

Result: Spectroscopy of thermally treated jet fuel

Application: Understanding of degradation of jet fuel at high temperatures

Customer: Richard Miles, Princeton University

Result: Design of liquid nitrogen-cooled Raman cells

Application: Laser-based imaging of fluid flows

## **DISCOVERIES**

An infrared stimulated scattering system and supercritical cell were developed under this contract.

## **HONORS / AWARDS**

Gregory Faris

ARCS Fellow, 1985-1986

Topical editor, *Applied Optics*

## **APPENDIX A**

**HIGH SPECTRAL RESOLUTION STIMULATED RAYLEIGH / BRILLOUIN  
SCATTERING AT 1- $\mu$ M, MANUSCRIPT IN PREPARATION.**



## **HIGH SPECTRAL RESOLUTION STIMULATED RAYLEIGH / BRILLOUIN SCATTERING AT 1- $\mu$ M**

Gregory W. Faris, Martina Gerken, Christian Jirauschek, DaNel Hogan, and Yihong Chen

Molecular Physics Laboratory

SRI International

333 Ravenswood Avenue, Menlo Park, CA 94025-3493

gregory.faris@sri.com

### **ABSTRACT**

We have demonstrated stimulated Rayleigh / Brillouin scattering at a wavelength of 1  $\mu$ m using an injection seeded Nd:YAG laser as a pump laser and a tunable diode laser as a probe laser. Spectra with good signal-to-noise ratio are obtained in spite of the low probe beam power and small gain coefficient in the infrared. Stimulated Rayleigh scattering is readily observable in most liquids due to absorption by the OH and CH overtone bands. The absorption also causes an asymmetry in the stimulated Brillouin peak. A Rayleigh linewidth of 8 MHz is measured with this approach.

**OCIS codes:** (290.5900) Scattering, stimulated Brillouin; (300.6320) Spectroscopy, high-resolution; (190.1900) Diagnostic applications of nonlinear optics; (999.999) Scattering, stimulated Rayleigh; (300.6340) Spectroscopy, infrared

MP 00-29  
March 9, 2000

Stimulated scattering may be used to perform noninvasive *in situ* measurements of material physical properties. Stimulated Rayleigh and stimulated Brillouin scattering provide information on the thermal and elastic properties, respectively, of the material under study. Linewidths for stimulated Rayleigh and stimulated Brillouin scattering are typically on the order of 10 and 100 of MHz, respectively. Thus, narrowband lasers are required for Rayleigh and Brillouin scattering measurements.

These measurements are non-resonant, and may be performed at any wavelength for which the medium under study is transparent or nearly transparent. Previous experiments on stimulated Rayleigh and Brillouin scattering have used a ring dye laser as either a pump or probe laser.<sup>1-3</sup> As an alternative to ring dye lasers, we have used an external cavity laser diode operating at 1064 nm. Although this laser provides over an order of magnitude less power than a ring dye laser and the gain coefficient is more than 4 times smaller at 1064 nm than at 532 nm, we find very good results with the laser diode. In addition, the absorption present in most liquids at 1064 nm makes stimulated Rayleigh scattering readily observable.

Liquids containing hydrogen atoms typically display absorption due to overtone or combination bands of the OH or CH stretch vibrations at our measurement wavelength of 1064 nm. This absorption causes significant changes in the stimulated Rayleigh and stimulated Brillouin spectra as compared with measurements performed in the visible spectral region, where many liquids have little or no absorption.

Brillouin and Rayleigh scattering involve scattering of light from density fluctuations caused by acoustic waves and non-propagating entropy waves, respectively. For stimulated Rayleigh and Brillouin scattering, there are two primary mechanisms for coupling the electric field of the light and the material fluctuations—electrostriction and absorption.<sup>4</sup> The electrostrictive effect (the force produced by the electric field through the linear polarizability) produces stimulated scattering in the absence of absorption. With absorption, thermal forces also can cause material fluctuations. For pure electrostrictive scattering, stimulated Rayleigh scattering is typically on the order of 100 times smaller than stimulated Brillouin scattering, and extremely difficult to observe. However, with thermal effects, the stimulated Rayleigh scattering can become larger than the stimulated Brillouin scattering, and is easily observed.

Our experimental apparatus for stimulated scattering at 1  $\mu\text{m}$  is shown in Fig. 1. The pump laser is an injection-seeded Nd:YAG laser. This laser is an attractive pump laser for stimulated scattering measurements as it can provide high peak powers to enhance the nonlinear response and near-Fourier transform limited linewidths to provide high spectral resolution. By reducing the oscillator pump energy, Fourier transform-limited spectral linewidths as narrow as

20 MHz have been obtained with this laser.<sup>5</sup> The probe laser is a diode laser, tuned through feedback from an external grating (EOSI model 2010). This laser has not been actively stabilized, so we rely on passive stability for our measurements. The elongated beam profile of the diode laser is reduced and circularized using an anamorphic prism pair (Melles Griot 06 GPA 003) producing a beam of roughly 1 mm in diameter. An acousto-optic modulator directs the probe beam to a Fizeau wavelength meter (New Focus model 7711), except for a 15 ms window centered at the time of pump pulse, when the modulator is turned off and the probe beam passes to the sample. Both the pump and probe beams are spatially filtered to remove higher order transverse mode structure. The pump and probe beams are overlapped in a cell containing the liquid in a counterpropagating geometry with a crossing angle of approximately 25 mrad. The gain signal is detected with a InGaAs photodiode (Fermionics FD100FC) and an transimpedance amplifier.

The Nd:YAG laser has approximately  $10^7$  times more power than the diode laser during a typical measurement. To prevent scattered Nd:YAG light from influencing the diode laser, two optical isolators are used on the diode laser beam. To prevent scattered pump laser light from overwhelming the gain signal, the detected light is spatially filtered using an iris, a lens and a 62.5  $\mu\text{m}$  core optical fiber coupled to the InGaAs detector.

The wavelength meter is calibrated between 400 and 1000 nm only. For these measurements we require accurate relative wavelength changes, not absolute wavelength values. we tested the accuracy of the relative wavelength readings by comparing the wavelength readings with the heterodyne frequency obtained by beating the diode laser and seed laser beams. The two measurements agreed to within 1.5%.

A stimulated Rayleigh/Brillouin spectrum for hexane obtained with this system is shown as the top curve in Fig. 2. The abscissa is the difference in frequency between the pump and probe lasers. The outer two peaks are Brillouin peaks; the central pair of peaks is due to stimulated Rayleigh scattering. The positive-going Brillouin peak to the left is a gain peak, corresponding to transfer of power from the Nd:YAG laser to the probe laser. The negative-going peak to the right is a loss peak, wherein power is transferred from the probe laser to the pump laser.

We performed fits to the measured lineshapes to determine linewidths, lineshifts, and peak heights. The electrostrictive Brillouin lineshape is described by the real part of the complex Lorentzian profile; the thermal Brillouin and Rayleigh lineshapes are described by the imaginary parts of a complex Lorentzian profile.<sup>4</sup> The measured lineshapes are described by the convolution of the Gaussian spectral lineshape of the Nd:YAG pump laser with these Lorentzian

profiles. These convolved lineshape may be expressed as the real and imaginary parts of the complex error function for the Gaussian for the Brillouin and Rayleigh peaks, respectively (the former is a Voigt profile). Fits were performed using the algorithm of Humlicek,<sup>6,7</sup> and the Igor graphics program (Wavemetrics). We use the Fourier-transform limited linewidth calculated from pulsewidth as the spectral linewidth.

The full fit to the Rayleigh/Brillouin spectrum is shown as the curve labeled "fit" in Fig. 2. Very good agreement is found between the measured and fit lineshapes (see also Figs. 3 and 4). The electrostrictive and thermal contributions to the overall fit are shown separately at the bottom of Fig. 2. Note that the imaginary Lorentzian shape of the thermal Brillouin scattering creates an asymmetry for the Brillouin peaks. This is seen more clearly in Fig. 3, which shows the Brillouin gain peak from Fig. 2. The spectroscopic and thermodynamic properties for n-hexane determined from numerous such fits are given in Table 1.

A scan over the stimulated Rayleigh peak is shown in Fig. 4. As the wavemeter does not provide sufficient spectral resolution over such a short frequency range, the frequency values for this measurement were determined from the heterodyne signal obtained by combining a portion the seed and probe lasers on a photodiode. This peak is quite narrow. The average linewidth determined from multiple fits such as shown in Fig. 4 gives value of  $7.9 \pm 3.2$  MHz, which is in good agreement with the value expected from the thermal diffusivity for n-hexane. These measurements were performed with a pulsewidth for the Nd:YAG laser of approximately 30 ns, which corresponds to a full width half maximum spectral linewidth of about 15 MHz. Thus the laser linewidth is about twice the measured linewidth of the Rayleigh peak. The good agreement with the expected linewidth confirms that the Nd:YAG laser has a transform-limited linewidth of 15 MHz.

For comparison, a stimulated scattering spectrum of methanol taken at 532 nm is shown in Fig. 5. This spectrum was acquired using the second harmonic of the same Nd:YAG laser and a cw ring dye laser (Coherent CR-699) as a probe laser. The spectra taken at 1064 (Fig. 2) and 532 nm (Fig. 5) are of similar quality, except that the infrared measurement has the strong stimulated thermal Rayleigh peak.

The ability to perform stimulated scattering in the infrared opens new measurement possibilities for materials that are only transparent in the infrared, allowing measurements within the bulk material rather than only on the surface. Measurement of spontaneous Brillouin or Rayleigh scattering in the infrared are greatly hampered by smaller scattering cross sections and poorer detector performance. However, with stimulated scattering the signal powers can be nearly as large as the laser power, overcoming these limitations. This allows bulk measurement

in materials that are not transparent in the visible such as most semiconductors and liquids containing multi-ring aromatic compounds.

This work was supported by the Air Force Office of Scientific Research under contract F-49620-97-C-0002.

## REFERENCES

1. S. Y. Tang, C. Y. She, and S. A. Lee, "Continuous-wave Rayleigh-Brillouin-gain spectroscopy in SF<sub>6</sub>," *Opt. Lett.* **12**, 870-872 (1987).
2. G. W. Faris, L. E. Jusinski, M. J. Dyer, W. K. Bischel, and A. P. Hickman, "High-resolution Brillouin gain spectroscopy in fused silica," *Opt. Lett.* **15**, 703-5 (1990).
3. K. Ratanaphruks, W. T. Grubbs, and R. A. MacPhail, "CW stimulated Brillouin gain spectroscopy of liquids," *Chem. Phys. Lett.* **182**, 371-378 (1991).
4. W. Kaiser and M. Maier, "Stimulated Rayleigh, Brillouin, and Raman spectroscopy," in *Laser Handbook*, F. T. Arecchi and E. O. Schulz-Dubois, Eds. (North-Holland, Amsterdam, 1972), Vol. 2, pp. 1077-1150.
5. G. W. Faris, M. J. Dyer, and W. K. Bischel, "Laser linewidth narrowing induced by amplifier gain saturation," *Opt. Lett.* **19**, 1529-1531 (1994).
6. J. Humlicek, "Optimized computation of the Voigt and complex probability functions," *J. Quant. Spectrosc. Radiat. Transfer* **27**, 437-444 (1982).
7. F. Schreier, "The Voigt and complex error function: A comparison of computational methods," *J. Quant. Spectrosc. Radiat. Transfer* **48**, 743-762 (1992).

Table 1.  
Properties measured in hexane using stimulated Rayleigh /Brillouin scattering.

Brillouin shift	$2.91 \pm 0.06$ GHz
Brillouin width	$151 \pm 8$ MHz
Rayleigh width	$7.9 \pm 3.2$ MHz
Acoustic damping time	1.06 ns
Acoustic velocity	1125 m/s
Acoustic attenuation coefficient	$8.4 \times 10^5$ m <sup>-1</sup>
Effective mass diffusion coefficient	$7.1 \times 10^{-6}$ m <sup>2</sup> /s
Isentropic compressibility	$1.2 \times 10^{-9}$ m <sup>2</sup> /N
Thermal diffusivity	$1.2 \times 10^{-7}$ m <sup>2</sup> /s

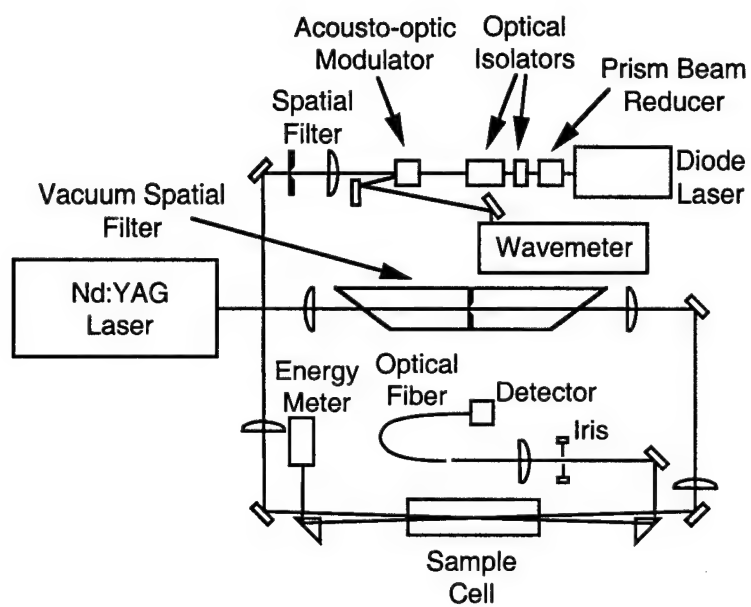


Fig. 1. Experimental apparatus for stimulated Brillouin and stimulated Rayleigh scattering.



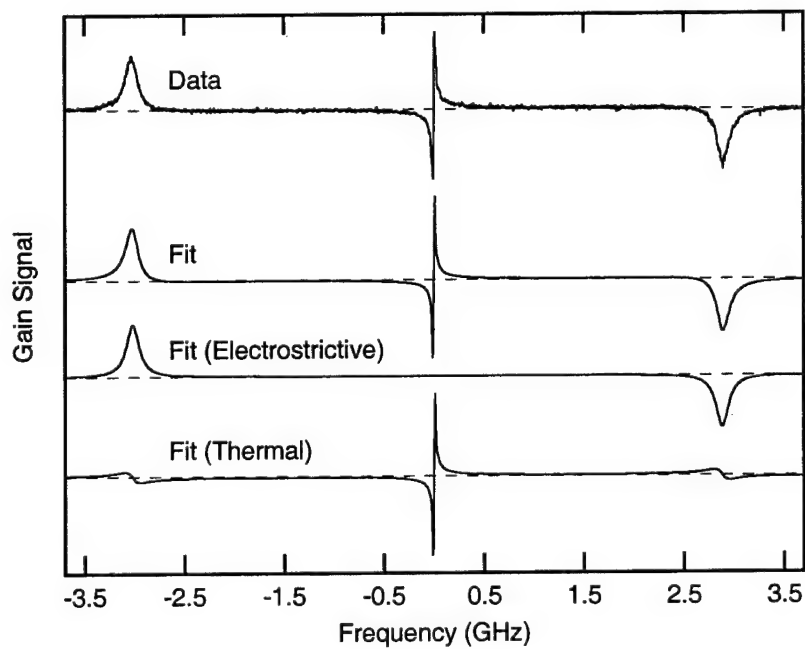


Fig. 2. Stimulated Rayleigh/Brillouin spectrum for n-hexane (top), fit to the data (middle) and electrostrictive and thermal components to the fit (bottom). The dashed lines indicate zero gain level for each curve.

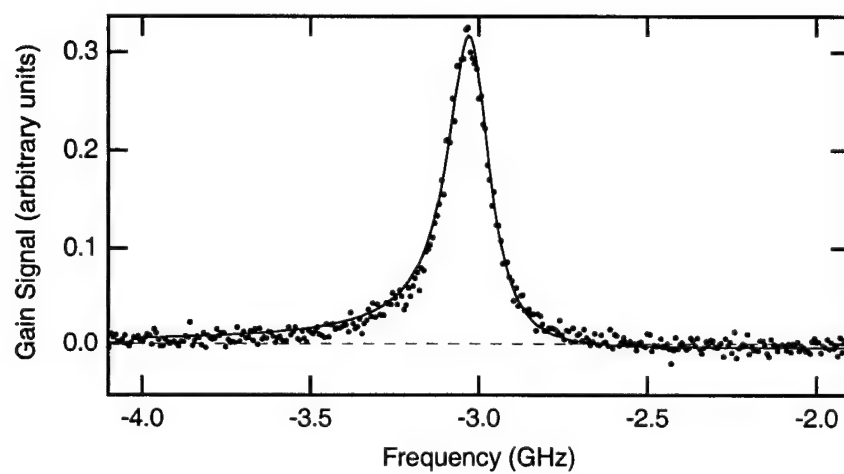


Fig. 3. Data (points) and fit (solid line) for stimulated Brillouin gain peak for n-hexane. Stimulated thermal Brillouin scattering gives an asymmetry to the peak.

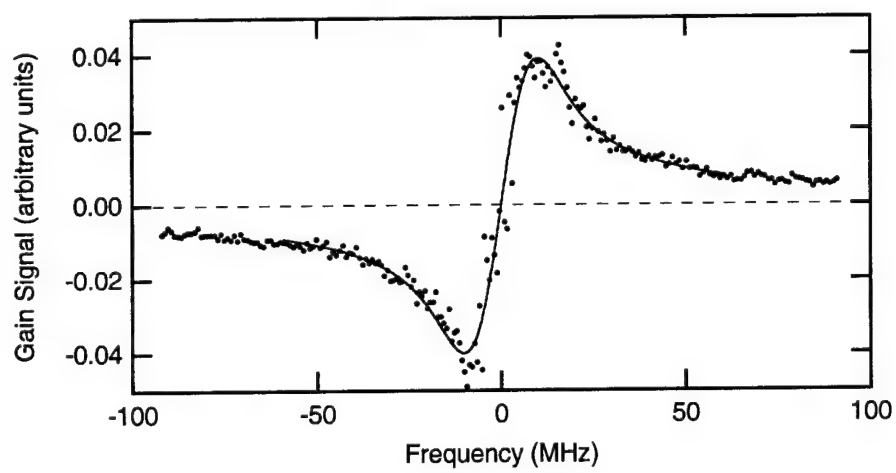


Fig. 4. Data (points) and fit (solid line) for stimulated thermal Rayleigh scattering in n-hexane.

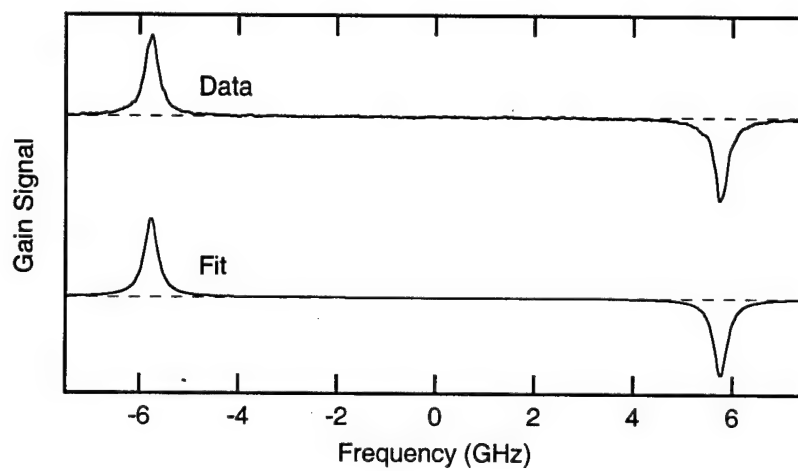


Fig. 5. Stimulated Brillouin spectrum for methanol measured at 532 nm.

## **APPENDIX B**

**ELECTROSTRICTIVE AND THERMAL STIMULATED RAYLEIGH  
SPECTROSCOPY IN LIQUIDS, MANUSCRIPT IN PREPARATION.**

Rayleigh scattering involves the scattering of light by non-propagating isobaric entropy fluctuations. Density variations associated with these fluctuations cause a modulation of the refractive index, and the spatial variations of the refractive index result in a scattering of light. When the incident light is sufficiently intense, stimulated Rayleigh scattering occurs. In this case, coupling of the incident (pump) light and the fluctuations can produce amplification of the scattered light, and coupling between the incident and scattered light fields can amplify the fluctuations.

In this Letter we describe the use of tunable Rayleigh gain spectroscopy in electrostrictive and predominantly absorptive liquids. This is the first observation of the transition from electrostrictive to thermal stimulated Rayleigh scattering to our knowledge. This transition is produced through varying the medium absorption. In agreement with theory,<sup>1</sup> for a certain amount of absorption the electrostrictive and the absorptive part of the gain factor cancel (see Eq. 1).

Two different mechanisms can produce the coupling between light and medium for simulated Rayleigh scattering—electrostriction and light absorption. In any medium, the electric field of the electromagnetic light wave can create a dipole moment through the medium polarizability. When the electric field is not uniform, as is always the case for an electromagnetic wave, the energy associated with the induced dipole moment and the electric field will vary spatially. The atoms or molecules in the field will experience a force associated with reaching the lowest energy state. This force is called electrostriction. In absorptive media, temperature changes due to the absorption of light result in additional density fluctuations, which give rise to stimulated thermal Rayleigh scattering.

Electrostrictive and thermal effects tend to produce opposite influences on density. Electrostrictive effects generally cause the density to increase in the regions with higher electric field. Thermal effects cause a lower density in the region of the higher electric field as the heated medium expands. The electrostrictive effect is relatively weak, and it is quite difficult to observe pure electrostrictive stimulated Rayleigh scattering. Stimulated thermal Rayleigh scattering is more readily observed because the absorptive gain factors are large compared to the electrostrictive ones.

The amplification or gain for the scattered light produced by a strong pump light beam can be monitored using a second probe light beam. The spectral variation in gain for the probe beam is given by the imaginary part of a complex Lorentzian function:<sup>1</sup>

$$g_{RL} = [g_{RL}^e(\max) - g_{RL}^a(\max)] \frac{4\omega/\Gamma_{RL}}{1 + (2\omega/\Gamma_{RL})^2} . \quad (1)$$

where  $\Gamma_{RL}$  is the spontaneous Rayleigh linewidth,  $g_{RL}^e(\max)$  and  $g_{RL}^a(\max)$  are the maximum values for the electrostrictive and the absorptive gain factors, respectively, and  $\omega = \omega_p - \omega_s$  is the difference between the frequencies  $\omega_p$  of the pump beam and  $\omega_s$  of the probe (or Stokes) beam.

We use a pump and probe experiment to measure stimulated Rayleigh scattering. The pump and probe beams are crossed in the sample cell containing the liquid. The cw probe beam is used to measure the gain produced by the intense pulsed pump light. The maximum gain signal is obtained for counterpropagating pumping.

The experimental apparatus used to measure the frequency dependence of the gain factor is illustrated in Fig. 1. Ray trajectories are represented by dashed lines. We use the light from an injection-seeded, home-built, single-mode Nd:YAG laser<sup>2</sup> at 1064 nm to provide the pump radiation. For our experiment, it is operated with a pulse duration of about 29 ns (FWHM) and a repetition rate of 10 Hz. The spectral bandwidth of the laser is Fourier transform limited, providing a linewidth of about 15 MHz for a 29 ns pulse. The probe light is provided by a tunable single-mode diode laser with a linewidth smaller than 300 kHz in 50 ms. An acousto-optic modulator directs the probe beam to a wavemeter in the intervals between the pump pulses for determination of diode laser wavelength.

The spatial filters serve to suppress higher order transverse spatial modes. Furthermore, the spatial filter in the probe trajectory, together with the two optical isolators, prevents pump light from reaching the resonator of the tunable laser, which would otherwise cause frequency and amplitude fluctuations on the probe beam. Inside the cell, the counterpropagating (180° crossing angle) pump and probe beams are overlapped at their focal points to obtain a large gain signal. Detection is performed using an InGaAs photodiode with a transimpedance amplifier. The output signal is split with a bias tee into a high frequency part, which is the gain signal for the ~29 ns pulse, and a low frequency part, which monitors the probe beam power. The energy of the Nd:YAG beam is measured with a pyroelectric energy detector connected to an energy meter. The measured gain signals are divided by the probe and pump beam powers to compensate for fluctuations in the laser powers. A fast silicon detector is used to measure the pulse duration of the pump beam.

For Rayleigh gain spectroscopy in liquids, the resolution of the wavemeter is only slightly smaller than the scanning interval of about 100 MHz. To allow high-resolution measurements of stimulated Rayleigh scattering, we directly measure the frequency difference  $\omega$  between the pump and the signal beams. Glass plates are employed to separate a few percent of the beams from the diode laser and seed laser used to injection seed the pump laser. These beams are combined on a beamsplitter and focused on a detector. The detector measures the frequency difference between the two lasers; the sum frequency is far beyond the detection bandwidth. This heterodyne or beat signal provides a direct measure of the frequency difference between the lasers, including a well defined zero point of the frequency shift. Moreover, frequency fluctuations of the seed laser are now taken into account.

We use freon 113 (1,1,2-trichlorotrifluoroethane, anhydrous) to observe stimulated electrostrictive Rayleigh scattering. Most liquids containing hydrogen atoms cannot be used because they have absorption at 1064 nm due to overtone and combination vibrational absorption from O-H and C-H bonds.

The pure electrostrictive stimulated Rayleigh peak is small. We used pump beam energies of about 5 mJ in a 30 ns pulse to observe the electrostrictive signal in freon 113. This corresponds to a power of about  $10^7$  times larger than the  $\sim 1$  mW of probe beam power available at the sample cell. The gain signals were approximately 1% of the probe beam power. Thus even a small fraction of scattered pump light can completely overwhelm the electrostrictive gain signal. This effect is exacerbated by the fact that the pump and probe beam have nearly identical frequencies in the region of the Rayleigh peak. Thus, a heterodyne signal between the probe beam and scattered pump light is also present at the detector used to measure the gain signal. This heterodyne process provides an effective amplification of the scattered pump light as the detected heterodyne signal is proportional to the square root of the product of the pump and probe powers. Thus the 1% gain signal is only as big as the heterodyne signal from a scattered pump light power of  $10^{-4}$  of the probe beam power, or  $10^{-11}$  of the pump beam power.

The influence of scattered pump light was reduced by using very clean windows and freon, by tilting the sample cell to direct reflections from the windows away from the detector, blocking all stray reflections and other scattered light with black screens, making the pump and probe beams of approximately the same diameter, spatially filtering the pump and probe beams to remove higher order transverse spatial modes, and spatially filtering the probe beam before the detector using an iris, lens, and multimode fiber. However, we could not reduce the scattered light below the level from the spontaneous Rayleigh scattering of the freon in the volume determined by the overlap between the pump and probe beams. This spontaneous Rayleigh scattering is the dominant noise source for our measurements. We reduce the influence of the heterodyne signal from spontaneous Rayleigh scattering by averaging the measured gain over many laser shots (typically 60 shots for the stimulated Rayleigh measurements).

We determined the height of the Rayleigh peak by fitting an appropriate lineshape to the measured gain signal. The spectral dependence of the gain signal is described by the convolution of the stimulated Rayleigh lineshape {imaginary part of the complex Lorentzian, Eq. (1)} and the Gaussian spectral profile of the pulse laser. This convolution may be expressed in terms of the imaginary part of the complex error function. We used the approximation of Humlicek<sup>3,4</sup> for the complex error function to perform the fitting. The linewidth of the Fourier-transform limited Nd:YAG pulse was determined by measuring the temporal duration of the pulse. The contribution of the probe laser linewidth is negligible.



The solid curve at the top of Fig. 2 shows the measured electrostrictive Rayleigh gain signal in freon 113. The width of the Rayleigh peak is broadened considerably by the spectral linewidth of the pulse laser. The dashed curve shows the result of the curve fitting. Freon 113 does not absorb at the Nd:YAG wavelength of 1064 nm and shows a relatively high electrostrictive gain. To produce some absorption in the freon, we use ethanol, which mixes with freon and has moderate absorption at 1064 nm. After adding 0.10% (volume percentage) of ethanol, the electrostrictive and the absorptive gain have the same value and cancel each other out (see Eq. 1). The measured curve is shown in the middle of Fig. 2. The Rayleigh gain signal (solid curve) shows no Rayleigh peak, and the curve fitting (dashed curve) produces a flat line. The small variations in the measured gain signal are due to the heterodyne signal from scattered pump light. After doubling the amount of ethanol in freon 113, we get a gain signal that has about the same height as in pure freon, but is inverted. The measured gain signal for 0.19% of ethanol is shown at the bottom of Fig. 2 (solid curve), the dashed curve is the fitted profile.

We have measured the absorption coefficient for different volume percentages of ethanol in freon (see Fig. 3). The absorption coefficient displays a linear dependence on the percentage of ethanol. This measurement shows that a very small absorption coefficient ( $0.00012 \text{ cm}^{-1}$ ) is sufficient to cause the cancellation of the electrostrictive Rayleigh scattering at 0.1% ethanol.

For small amounts of ethanol in freon the physical properties (apart from the absorption) are changed only little. Theory<sup>1</sup> predicts a linear growth of the maximum absorptive gain factor  $g_{\text{RL}}^{\text{a}}(\text{max})$  with the absorption coefficient, whereas the maximum electrostrictive gain factor  $g_{\text{RL}}^{\text{e}}(\text{max})$  does not depend on the absorption. Measurements of the gain signal were performed for various amounts of ethanol in freon, and the height of the Rayleigh peak was determined. The results are shown in Fig. 4 for small percentages of ethanol. We display peak height rather than peak area as the area of the Rayleigh peak is infinite {Eq. (1) behaves as  $1/\omega$  for large  $\omega$ }. As expected, the height displays a linear dependence on the absorption coefficient {or  $g_{\text{RL}}^{\text{e}}(\text{max}) - g_{\text{RL}}^{\text{a}}(\text{max})$ }. The height has a negative value for  $g_{\text{RL}}^{\text{a}}(\text{max})=0$  in pure freon, becomes zero for  $g_{\text{RL}}^{\text{a}}(\text{max})=g_{\text{RL}}^{\text{e}}(\text{max})$ , corresponding to 0.1% of ethanol, and has positive values for  $g_{\text{RL}}^{\text{a}}(\text{max})>g_{\text{RL}}^{\text{e}}(\text{max})$ .

When the probe laser is scanned over a larger frequency range, stimulated Brillouin scattering is observed. The shapes of the stimulated electrostrictive and thermal Brillouin scattering peaks are described by the real and imaginary parts of the complex Lorentzian profile, respectively.<sup>1</sup> Only stimulated electrostrictive Brillouin scattering is observed in pure freon 113 (Fig. 5). Gain and loss peaks are observed at the left and right of Fig. 5, respectively. The gain and loss peaks corresponds to transfer of energy from the pump laser to the probe laser and vice

versa. The stimulated electrostrictive Rayleigh scattering, which is typically about 100 times smaller than the stimulated electrostrictive Brillouin scattering, is too small to be seen in Fig. 5.

The modest absorption coefficient of ethanol at 1064 nm ( $0.12 \text{ cm}^{-1}$ ) is sufficient to cause very large stimulated thermal Rayleigh scattering in ethanol (Fig. 6). The stimulated thermal Rayleigh peak is much larger than the stimulated electrostrictive Brillouin scattering in ethanol. Stimulated thermal Brillouin scattering causes asymmetry of the Brillouin peaks in this case.

We have reported an experimental investigation of stimulated Rayleigh scattering in liquids by tunable Rayleigh gain spectroscopy. We have observed the electrostrictive Rayleigh peak in freon 113, which is the first observation of stimulated electrostrictive Rayleigh scattering in a liquid to our knowledge. By adding small amounts of ethanol, we have increased the absorption coefficient to the point where electrostrictive and absorptive gain cancel out. For a further increase of the absorption, the peak inverts from its original form. In agreement with theory, a linear relationship between the height of the peak and the absorption coefficient has been observed.

This work was supported by the Air Force Office of Scientific Research under contract F-49620-97-C-0002.

## REFERENCES

1. W. Kaiser and M. Maier, "Stimulated Rayleigh, Brillouin, and Raman spectroscopy," in *Laser Handbook*, edited by F. T. Arecchi and E. O. Schulz-Dubois (North-Holland, Amsterdam, 1972), Vol. 2, pp. 1077-1150.
2. M. J. Dyer, W. K. Bischel, and D. G. Scerbak, "High-power 80-ns transform-limited Nd:YAG laser," *Proc. SPIE* **912**, 32-36 (1988).
3. J. Humlicek, "Optimized computation of the Voigt and complex probability functions," *J. Quant. Spectrosc. Radiat. Transfer* **27** (4), 437-444 (1982).
4. F. Schreier, "The Voigt and complex error function: A comparison of computational methods," *J. Quant. Spectrosc. Radiat. Transfer* **48** (5-6), 743-762 (1992).

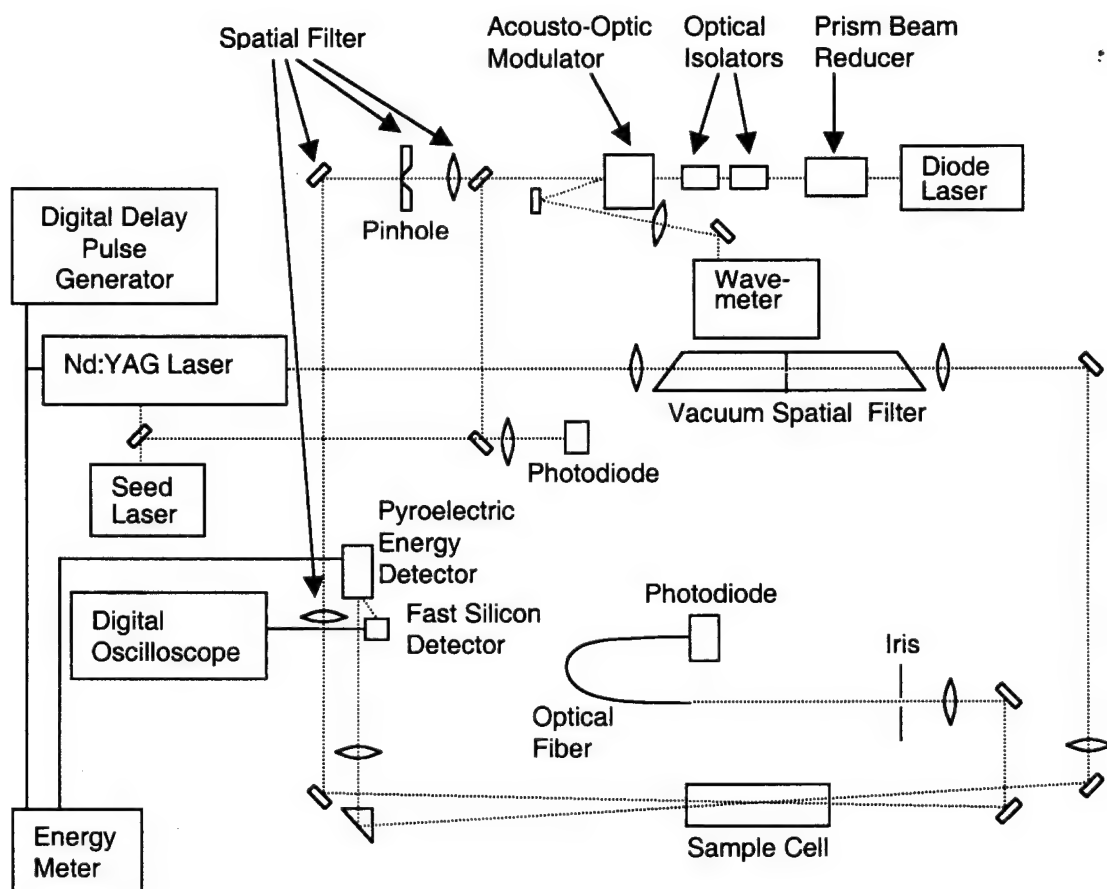


Fig. 1. Experimental apparatus for stimulated Rayleigh gain spectroscopy in liquids.

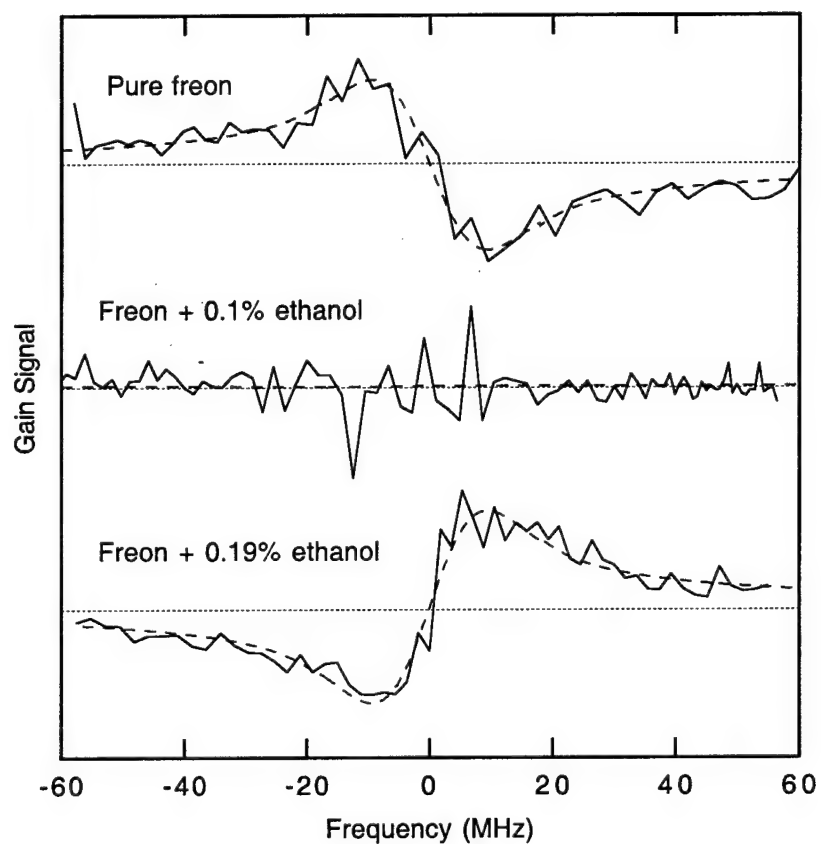


Fig. 2. Measured stimulated Rayleigh gain signal (solid curve) and fitted profile (dashed curve) in pure freon 113 (top), and freon with 0.1% ethanol (middle) and 0.19% ethanol (bottom) as a function of the frequency difference between the pump and probe lasers.

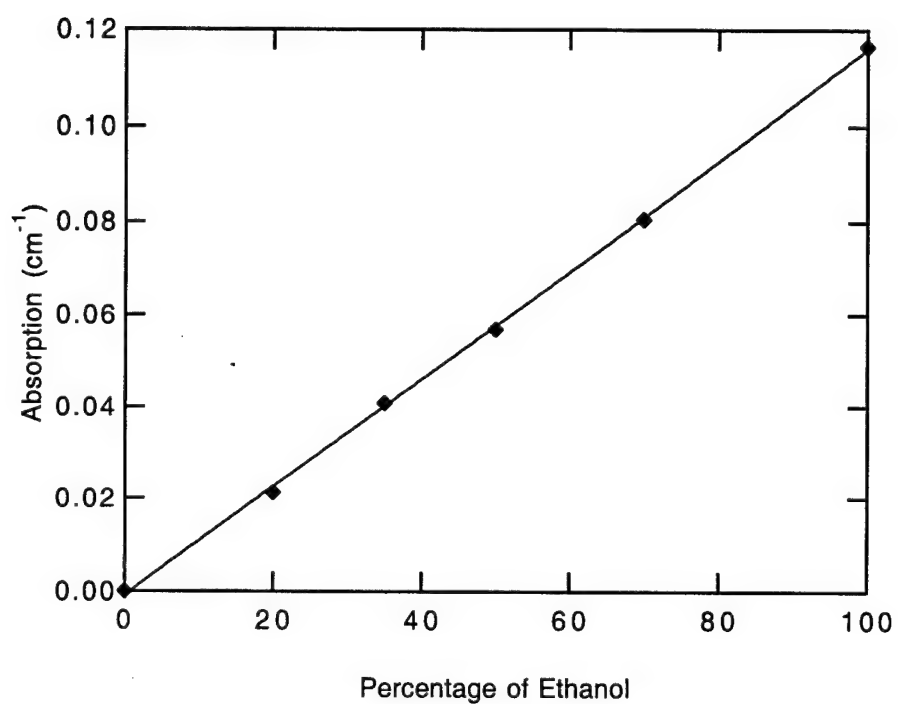


Fig. 3. Absorption coefficient in a mixture of freon 113 and ethanol at a wavelength of 1064 nm.

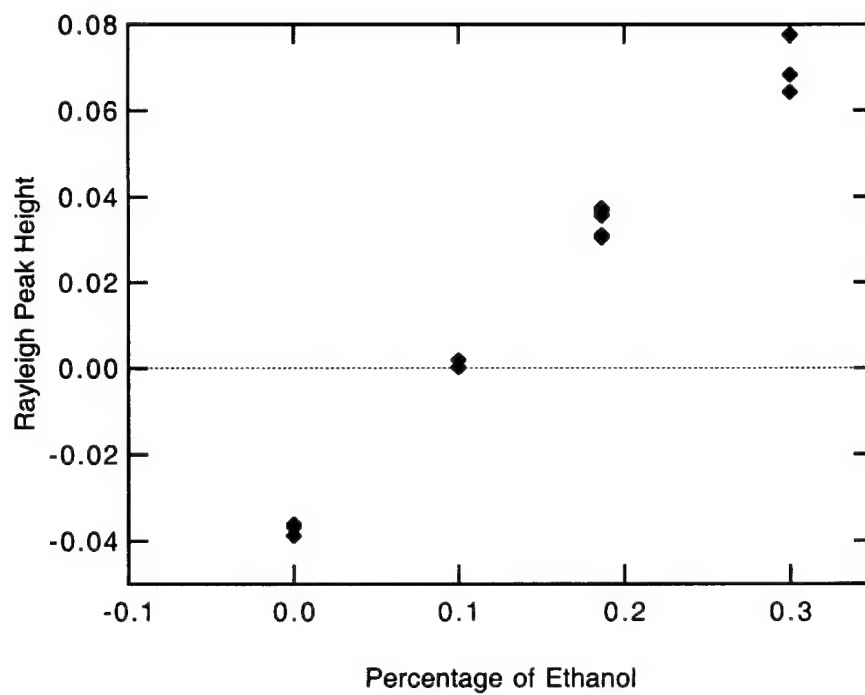


Fig. 4. Measured heights of the Rayleigh peak in a mixture of freon 113 and ethanol.

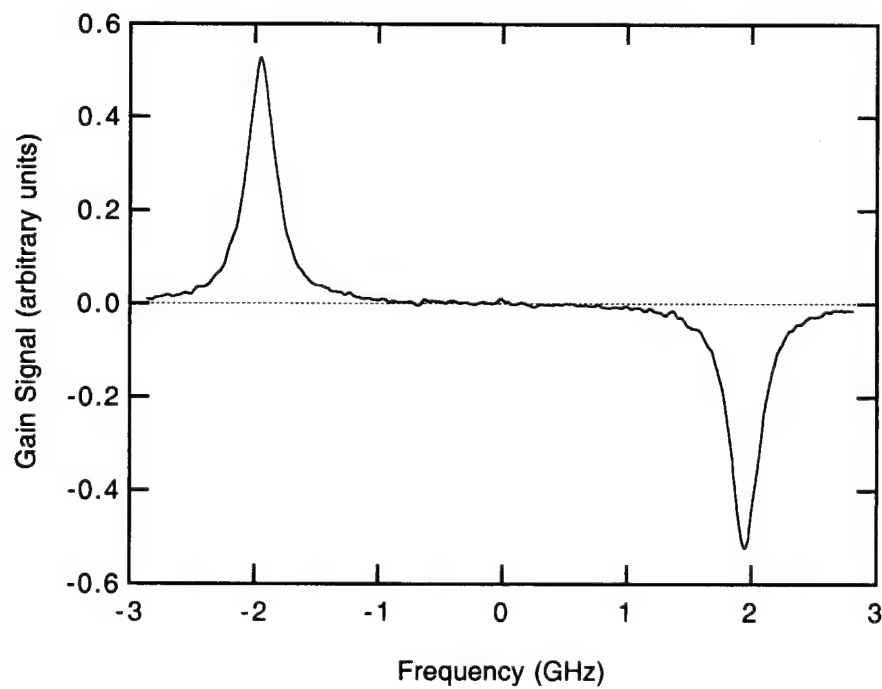


Fig. 5. Measured stimulated Brillouin gain signal in pure freon 113 as a function of the frequency difference between the pump and probe lasers. The stimulated Rayleigh gain signal of Fig. 2 is too small to be seen in this figure.



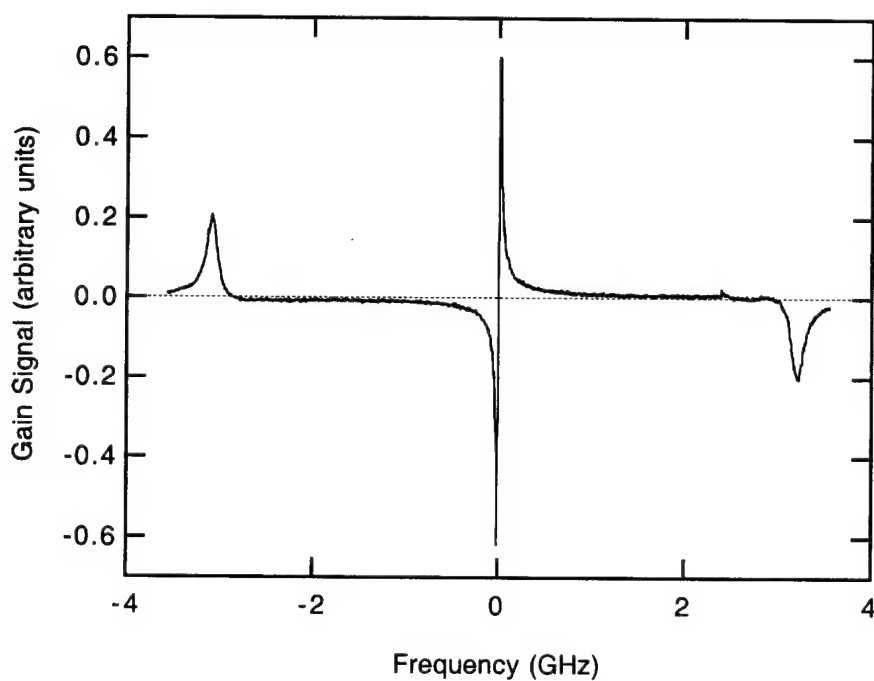


Fig. 6. Measured stimulated Brillouin gain signal in ethanol as a function of the frequency difference between the pump and probe lasers. Absorption produces a large stimulated thermal Rayleigh peak and stimulated thermal Brillouin scattering, which causes asymmetry of the stimulated Brillouin peaks.

## **APPENDIX C**

**TWO-PHOTON-RESONANT DIFFERENCE-FREQUENCY MIXING WITH AN  
ARF EXCIMER LASER: VUV GENERATION AND MULTI-PHOTON  
SPECTROSCOPY, SUBMITTED TO J. OPT. SOC. AM. B (2000).**

# **TWO-PHOTON-RESONANT DIFFERENCE-FREQUENCY MIXING WITH AN ARF EXCIMER LASER: VUV GENERATION AND MULTI-PHOTON SPECTROSCOPY**

Gregory W. Faris, Scott A. Meyer, Mark J. Dyer, and Michael J. Banks

Molecular Physics Laboratory

SRI International

Menlo Park, CA 94025

## **ABSTRACT**

Two-photon-resonant difference frequency generation using an ArF excimer laser provides widely tunable VUV radiation at high pulse energies. Two-photon resonances in H<sub>2</sub>, Kr, and HD are within the tuning range of the ArF laser. With this technique, we have directly measured over 65  $\mu$ J at 133 nm. H<sub>2</sub> has a significantly smaller phase mismatch than Kr, leading to more efficient VUV generation, particularly at shorter VUV wavelengths. However, mixing in H<sub>2</sub> also produces additional VUV lines from two-photon excited amplified spontaneous emission (ASE). We have observed new ASE lines produced in this manner. H<sub>2</sub> is ineffective at generation of Lyman- $\alpha$  radiation due to the production of H atoms. With a phase matched mixture of Kr and Ar, we have directly measured 7  $\mu$ J at Lyman- $\alpha$ . A physical basis for the asymmetric tuning profile in this gas mixture is presented. With light from this VUV source, we have performed 1+1 REMPI in Xe at 147 nm and two-photon-excited fluorescence in neon at 133 nm.

OCIS codes: (190.4380) Nonlinear optics, four-wave mixing; (300.6410) Spectroscopy, multiphoton; (140.7240) UV, XUV, and X-ray lasers; (190.1900) Diagnostic applications of nonlinear optics

MP 00-006  
January 28, 2000

## 1. INTRODUCTION

High power VUV radiation is required for a variety of applications such as multiphoton spectroscopy and diagnostics,<sup>1-4</sup> plasma diagnostics,<sup>5-11</sup> and photochemistry.<sup>12-15</sup> Approaches to production of high power VUV radiation include resonantly-enhanced four-wave mixing in gases and metal vapors,<sup>16-20</sup> high order Raman shifting,<sup>2,3,8,11,21-23</sup> nonlinear mixing in crystals (down to  $\sim 170$  nm),<sup>24,25</sup> and direct laser sources.<sup>26,27</sup> Of the broadly tunable sources, Raman shifting offers simplicity through the use of a single laser source, but pronounced amplitude variations are produced for the large number of anti-Stokes shifts required to reach deep into the VUV. The resonantly-enhanced mixing schemes can provide high powers deep into the VUV, but typically require two lasers. Two-photon resonant sum- and difference-frequency mixing may be performed using resonances in Kr,<sup>28,29</sup> Hg,<sup>1,30</sup> Xe<sup>31,32</sup> and other gases<sup>33-35</sup> using frequency-doubled dye lasers to provide the two-photon-resonant photons.

Although the ArF excimer laser has a relatively narrow tuning range of approximately 1 nm, there are by coincidence a number of two-photon resonances available in Kr, H<sub>2</sub>, and HD within this range.<sup>3,36</sup> The ArF laser provides a number of advantages for two-photon resonant difference-frequency mixing. The generated VUV power nominally scales as the square of the power for the two-photon resonant wavelength, for which the ArF can provide very high energies (up to 100 mJ). The short wavelength of the two-photon-resonance allows tuning to short VUV wavelengths (the nominal tuning range is 110 to 180 nm) and reduces the phase mismatch.

The application of ArF radiation to tunable VUV generation through two-photon-resonant difference frequency mixing was proposed as early as 1984 by Hilbig et al. (in Kr),<sup>37</sup> reported in 1991 by Strauss and Funk<sup>38</sup> and Faris and Dyer,<sup>39</sup> and extended to femtosecond VUV generation in 1996 by Kittelmann et al.<sup>40</sup> The ArF excimer laser has also been used for VUV and XUV generation through third harmonic generation,<sup>41</sup> sum frequency mixing,<sup>42,43</sup> two-photon pumped

amplified spontaneous emission,<sup>44</sup> Raman shifting,<sup>3,21,45,46</sup> and other nonlinear processes.<sup>47-49</sup> All these processes, with the exception of the Raman shifting, use two-photon resonances to provide enhancement.

This paper describes the use of an ArF laser for two-photon-resonant difference frequency mixing. Mixing is performed in Kr using the  $4p^5 6p[3/2,2] \leftarrow 4p^6 \ ^1S$  two-photon resonance at  $103363.4 \text{ cm}^{-1}$  and in  $H_2$  using the  $E,F \ ^1\Sigma_g^+ (v'=6, J'=1) \leftarrow X \ ^1\Sigma_g^+ (v''=0, J''=1)$  two-photon resonance at  $103487.1 \text{ cm}^{-1}$ . Factors affecting conversion efficiency and tuning range are discussed in Section 2. Experimental results for VUV generation are described in Section 3. Application of this VUV radiation to multi-photon spectroscopy is presented in Section 4.

## 2. VUV CONVERSION EFFICIENCY

For the four-wave sum and difference-frequency mixing processes described by  $\omega_4 = 2\omega_1 \pm \omega_2$ , the generated power  $P_4$  scales according to

$$P_4 \propto N^2 [\chi^{(3)}]^2 [P_1]^2 P_2 F \quad (1)$$

where  $N$  is the number density of atoms or molecules,  $\chi^{(3)}$  is the third order nonlinear susceptibility for this mixing process,  $P_1$  and  $P_2$  are the incident powers, and  $F$  is a phasematching integral. For mixing using collinear Gaussian beams with a common focus at  $z=0$ ,  $F$  is given by<sup>50-52</sup>

$$F(b_1, \bar{b}, \Delta k, z_a, z_b) = 4 \bar{b} \int_0^\infty \rho \left| \int_{-2z_a/b_1}^{2z_b/b_1} \frac{1}{a(u)} \exp\left[-\frac{\rho^2}{f(u)}\right] \exp\left[-i \frac{b_1 \Delta k u}{2}\right] du \right|^2 d\rho \quad (2)$$

where  $-z_a$  and  $z_b$  are the positions of the entrance and exit windows of the mixing cell and  $\bar{b}=b_1/b_2$  is the ratio of the input confocal parameters. The phase mismatch between the  $k$  vectors for the driving waves ( $k_1$  and  $k_2$ ) and the generated wave ( $k_4$ ) is  $\Delta k = k_4 - k'$  where  $k'=2k_1 \pm k_2$ . The

upper (lower) sign refers to sum (difference) frequency mixing here and in Eqs. (3) and (5) below. The dimensionless integration variables are given by  $u = 2z/b_1$  and  $\rho = \sqrt{k'/b_1} r$ , where  $z$  and  $r$  are the coordinates parallel and perpendicular to the laser propagation direction, respectively. When absorption and nonlinear refractive index effects<sup>28</sup> are negligible and  $\Delta k \ll k_4$ , the factors  $f(u)$  and  $a(u)$  are given by<sup>51-53</sup>

$$f(u) = \left[ \frac{(1+iu)(1 \pm i\bar{b}u)}{g(u)} - i \left( u - \frac{2z_b}{b_1} \right) \right] \quad (3)$$

$$a(u) = f(u) g(u) (1+iu) \quad (4)$$

where

$$g(u) = \frac{2k_1(1 \pm i\bar{b}u) + \bar{b}k_2(1+iu)}{k'} = \frac{(2k_1 + \bar{b}k_2)}{k'} \pm i\bar{b}u \quad (5)$$

The integral  $F$  accounts for the interaction between the driving polarization produced by the pump beams and the generated wave, integrated over the cell length. The factors  $a(u)$  and  $f(u)$  account for the effects of focusing on the frequency conversion, and the phase mismatch  $\Delta k$  accounts for dispersion.

## A. TUNING PROFILES

Simple expressions for  $F$  may be obtained for two special cases, (I) sum frequency generation for  $\bar{b} = 1$  and (II) difference frequency generation for  $k_2 \rightarrow 0$ . In both cases, Eq.(3) simplifies to  $f(u) = 1 + i2z_b/b_1$ . In addition, the generated beam is Gaussian with confocal parameter  $b_1$ .<sup>50</sup> Because  $f$  is independent of  $u$ , the integrals over  $u$  and  $r$  can be performed separately. In the tight focusing limit  $b_1, b_2 \ll z_a, z_b$ , the phasematching integral simplifies to:

(I) Sum frequency generation,  $\bar{b} = 1$  ( $b_1 = b_2 = b$ )

$$F = \begin{cases} \pi^2 (b\Delta k)^2 \exp(b\Delta k) & \text{for } \Delta k \leq 0 \\ 0 & \text{for } \Delta k \geq 0 \end{cases} \quad (6)$$

(II) Difference frequency generation,  $k_2 \rightarrow 0$

$$F = \begin{cases} \bar{b} \left( \frac{2\pi}{1+\bar{b}} \right)^2 \exp(b_1 \Delta k) & \text{for } \Delta k \leq 0 \\ \bar{b} \left( \frac{2\pi}{1+\bar{b}} \right)^2 \exp\left( - \frac{b_1 \Delta k}{\bar{b}} \right) & \text{for } \Delta k \geq 0 \end{cases} \quad (7)$$

Eq. (7) indicates that for difference frequency generation,  $F \sim \exp(b_1 \Delta k)$  for  $\Delta k < 0$  and  $F \sim \exp(-b_2 \Delta k)$  for  $\Delta k > 0$ . For  $\bar{b}=1$ , Eq. (7) simplifies further to  $F = \pi^2 \exp(-b|\Delta k|)$ .

The source of the asymmetry in Eq. (7) for  $\bar{b} \neq 1$  can be understood by examining the phase and amplitude variations in the phasematching integral. These phase and amplitude variations can be visualized with the vectorial approach used by Ward and New,<sup>54</sup> which they refer to as vibration curves. The contribution of each differential length increment,  $du$ , for the integrand over  $u$  in Eq. (2) is plotted as an infinitesimal vector in the complex plane. By plotting each vector head to tail, the magnitude of the integral over  $u$  is given by the distance from the tail of the first vector to the head of the last vector. For the limiting cases of Eqs. (6) and (7),  $F$  is proportional to the square of this distance because the integrals over  $u$  and  $\rho$  are separable.

A good orientation to the vibration curve is provided by the example of third harmonic generation as shown in Fig. 1(a). Three curves are plotted for values  $b\Delta k = 0$  and  $\pm 2$ . To provide a measure of physical distance, open circles are plotted at intervals of  $\Delta u = 1$  ( $\Delta z = b/2$ ) throughout Fig. 1. Each set of three curves in Fig. 1 crosses at the point  $u=0$  ( $z=0$ ). For  $b\Delta k = 0$  the vibration curve is a circle, starting at the bottom, and returning to the same point; third harmonic generation is zero for  $b\Delta k = 0$ . The source of the phase variation producing this circle is the Guoy effect,<sup>55</sup> which is an additional phase shift of  $\pi$  that occurs when an optical beam passes through a focus. For third harmonic generation, the driving polarization has a phase shift of  $3\pi$  ( $\pi$  for each input beam), while the generated radiation has a shift of only  $\pi$ . The difference in phase between the driving polarization and the generated radiation produces a net phase shift of  $2\pi$ , equal to the angle around the circle. In effect, destructive interference between the driving polarization and the radiation generated at different positions in the cell cancel the generated beam energy. When there is phase mismatch, dispersion provides an additional phase change. For  $\Delta k < 0$ , the phase

variation due to dispersion can counteract the phase variation due to the Guoy effect, leading to non-zero third harmonic generation. For  $\Delta k > 0$ , phase changes from dispersion and the Guoy effect have the same sign, leading to a tighter circle (spiral), and again no generated radiation. This produces the well-known result that third harmonic generation only occurs for  $\Delta k < 0$  (see inset graph of  $F$  versus  $b_1 \Delta k$  in Fig. 1(a), and Eq (6)).

The case of difference frequency generation ( $\omega_4 = 2\omega_1 - \omega_2$ ) and equal confocal parameters ( $\bar{b}=1$ ) is shown in Fig. 1(b). For clarity, we present the special case  $k_2 \rightarrow 0$ . For difference-frequency generation, the Guoy phase shifts for  $\omega_2$  and  $\omega_1$  have opposite signs. Thus the driving polarization and the generated wave both have a phase shift of  $\pi$ , and the vibration curve is a straight line for  $\Delta k \rightarrow 0$  (for  $k_2 \neq 0$ , there will be small curvature to this line). Positive or negative values for  $\Delta k$  produce equal integrated magnitudes, so the tuning profile is symmetric (see also inset graph in Fig. 2(b)).

When the confocal parameters are not equal ( $\bar{b} \neq 1$ ), the Guoy effect for the driving waves occurs over different distances. In this case, the vibration curve for  $b\Delta k = 0$  has significant curvature as shown in Fig. 1(c), again plotted for  $k_2 \rightarrow 0$ . Now positive and negative values of  $\Delta k$  do not produce equal integrated values. A strong asymmetry is produced in the tuning profile, as is seen in the inset graph. For positive  $\Delta k$ , the phase mismatch has the same sign as the Guoy effect for the  $\omega_2$  beam, and  $b_2$  governs the phasematching tuning width. For negative  $\Delta k$ , the phase mismatch and the Guoy effect for  $\omega_1$  have the same sign, and  $b_1$  governs the tuning width. The symmetry between  $b_1$  and  $b_2$  for  $\Delta k < 0$  and  $\Delta k > 0$  in Eq. (7) occurs because the Guoy effects of one of the  $\omega_1$  waves and the generated wave cancel for  $k_2 \rightarrow 0$  (they both have confocal parameters  $b_1$ ). When  $k_2 \neq 0$ , there is an additional asymmetry that depends on the ratio  $k_2/k'$  in Eq. (5). However, for reasonable values of  $k_2/k'$  and  $\bar{b}$ , the net asymmetry is dominated by the size of  $\bar{b}$  rather than  $k_2/k'$ .

In general, difference frequency generation using equal confocal parameters is preferable. When the confocal parameters are not equal, the peak difference frequency conversion efficiency is



reduced by a factor of approximately  $(1+\bar{b})(1 + 1/\bar{b})/4$ , which is always greater than one.

However, it may be desirable to have an asymmetric tuning profile in certain cases, for example to enhance or reduce difference frequency mixing in the region where sum frequency mixing occurs near  $b\Delta k=-2$ .

## B. PHASE MISMATCH

We have calculated the phase mismatch for Kr, Ar, and H<sub>2</sub> using published index of refraction data. We include Ar because we have used a mixture of Kr and Ar to phase match VUV generation in the region of Lyman- $\alpha$ . For Ar we use the Sellmeier expression given by Leonard<sup>56</sup> which is based on measurements performed down to 110 nm by Chashchina et al.<sup>57</sup> This expression gives much better agreement with other refractive index measurements in the range of 110-120 nm<sup>58-60</sup> than the Sellmeier expression for Ar of Bideau-Mehu et al.,<sup>61</sup> which is based on measurements down to 140 nm. For H<sub>2</sub>, we use the Sellmeier expression given by Chashchina and Shreider,<sup>62</sup> based on measurements down to 115 nm. This expression agrees with the more recent measurements between 110 and 115 nm of Gordon et al.<sup>60</sup> to within experimental error. For Kr we use the analytic expression of Bulanin and Kislyakov,<sup>63</sup> which is based on measured oscillator strengths for Kr with adjustment of the oscillator strengths of the first two resonance transitions to optimally match measured refractive index and static polarizability data. They state the expression should be valid up to the second resonance transition. Their refractive index expression agrees with the earlier calculations of Mahon et al.<sup>64</sup> for  $(n-1)$  to within 2-3% near Lyman- $\alpha$ , which lies between the first and second resonance transitions. Experimental measurements of the refractive index for Kr near Lyman- $\alpha$  have a very large spread<sup>58,65,66</sup> and don't provide a good test of the accuracy of these two calculations in this region.

In Fig. 2, we plot the phase mismatch per atom or molecule  $C=\Delta k/N$  for two-photon-resonant four-wave mixing with the ArF excimer laser in Kr, Ar, and H<sub>2</sub>, where  $N$  is the number density of each gas. Note that the phase mismatch for H<sub>2</sub> is typically much less than the phase

mismatch for Kr. The phase mismatch for Kr becomes negative at 123.58 nm, and increases quite rapidly until the next resonance at 116.49 nm, passing through zero near 120 nm.

### C. SATURATION EFFECTS

The description of conversion efficiency given above does not account for absorption of the VUV wave or saturation effects<sup>28,44,47,49,67-70</sup> that limit the conversion at high powers. Factors contributing to saturation include the Kerr effect, and for resonantly-enhanced processes, power broadening, Stark shifts, two-photon absorption, multiphoton ionization, stimulated hyper-Raman scattering, amplified spontaneous emission, parametric four-wave mixing, self-defocusing, and related nonlinear effects. These processes lead to changes in refractive index, population redistributions, and depletion of the pump waves that vary both along and transverse to the pump beams. Thus, deviations from the simple descriptions for conversion efficiency are to be expected.

## 3. VUV GENERATION

Our experimental arrangement for VUV generation is shown in Fig. 3. The ArF excimer laser (Lambda Physik EMG-150 MSC) has separate oscillator and amplifier discharge chambers. To improve the beam quality for nonlinear frequency conversion, the laser has been modified to include a spatial filter before the amplifier and to triple pass the amplifier.<sup>3</sup> The laser beam divergence is about 5 times over the diffraction limit. Energies of up to 100 mJ are obtained, although more typical operational energies are about 20 mJ. The second laser is a Nd:YAG-pumped dye laser (Quanta-Ray DCR II and PDL). To produce longer VUV wavelengths, the second harmonic of the dye laser is used. A control circuit (Lambda Physik model EMG 97) is used to minimize drift of the excimer laser pulse timing. The beam path of the ArF laser is purged with argon to minimize the effects of oxygen Schumann-Runge absorption.<sup>3</sup> The ArF and dye beams are combined using a high-power 45° ArF dielectric mirror and focused with a single 50-cm or 100-cm lens into the mixing cell. A telescope is used to adjust the dye laser spot size and

compensate for the chromatic aberration of the focusing lens. A half waveplate is used to produce horizontal polarization for the dye laser to match the horizontal polarization of the ArF laser. When the dye laser output is frequency doubled, the waveplate is not used since the frequency doubling process provides a horizontally polarized output beam.

To monitor whether the ArF wavelength is resonant with the desired two-photon transition, ions produced through 2+1 resonantly-enhanced multi-photon ionization (REMPI) are monitored using an electrode biased at +1.5 to +3 V relative to the cell. The electrode is placed before the laser focus to avoid spectral resolution loss due to power broadening at the focus.

At the output of the mixing cell, a single off-center MgF<sub>2</sub> lens is used to either refocus or collimate the VUV beam, to dispersively separate the VUV and pump beams, and as a window to the cell. This single-optic arrangement minimizes the amount of absorption loss for the VUV beam. This lens is mounted on a vacuum x-y-z adjustment stage to allow adjustment of the VUV beam position.

To prevent a potentially rapid decrease in the VUV transmission caused by trace amounts of oil, liquid nitrogen and an acetone/dry ice bath are used to isolate the VUV beamline and mixing cell, respectively, from the vacuum pumps. Acetone/dry ice is used on the mixing cell to avoid a significant boiloff of liquid nitrogen when the gas in the cell is replaced. High purity (99.997 or better) Kr, H<sub>2</sub> and Ar were used in the mixing cell.

During previously reported work,<sup>4</sup> we found decay of the MgF<sub>2</sub> optics transmission after relatively short VUV irradiation (approximately 15 min). We built a VUV generation cell with no exit window cell to study this effect. This cell consisted of a 30-cm long, 4-mm inside diameter pyrex tube, sealed with a window at the entrance and open at the exit. The cell was filled at the window end using a pulsed valve. 2+1 REMPI (resonantly enhanced multiphoton ionization) in H<sub>2</sub> was used to monitor the cell pressure. This cell functioned well for VUV generation, and was used to study the transmission of optics inserted into the generated VUV beam using a vacuum feedthrough fitting. When we tested recently purchased VUV grade MgF<sub>2</sub> optics with the

windowless cell, we did not find any rapid transmission decay. Nor have we found rapid optics decay problems using newer VUV-grade optics in our more recent VUV generation experiments. This may be indicative of improvements in the quality of VUV grade optical material since the previous studies.

We have, however, observed a decay of the response for the pyroelectric energy probes used to measure absolute VUV energies.<sup>71</sup> On exposure to high power Lyman- $\alpha$  radiation, the probe sensitivity drops for the VUV as well as for the pump beams. The sensitivity drops over 2 to 3 minutes during VUV exposure, and recovers when the VUV is removed, for example when a delay is introduced between the timing of the two pump laser pulses. Detection of the VUV with a second detector (observation of scattered VUV light with a Lyman- $\alpha$  bandpass filter and a KBr photomultiplier tube) confirmed that the drop in pyroelectric probe response was not due to loss of VUV power. The drop in response was observed for both a Laser Precision model RjP735 probe in vacuum and for a Molectron J3-09 probe operated under an Ar purge. The sensitivity of the Laser Precision probe recovered over periods of tens of minutes to hours, while the Molectron probe recovered in less than ten minutes. Under certain circumstances, the pulsed electrical output from the Molectron probe inverted from positive to negative. For the Laser Precision probe, the recovery time increased with successive irradiation episodes, and the signal did not recover by illuminating a different portion of the detector.

The nature of this sensitivity loss for these pyroelectric probes is not completely understood. Pyroelectric energy meters have been used for measurements of high power VUV at wavelengths of 130 nm and above.<sup>4,30</sup> These reports do not mention decay in the response of the energy meters, indicating that the sensitivity decline of pyroelectric energy meters may not occur at 130 nm and above. Other VUV energy or power detectors exist such as Schottky photodiodes used for synchrotron radiation<sup>72</sup> and ionization cells.<sup>73</sup> However, these detectors may saturate for the kW power levels described here.

We have used both Kr and H<sub>2</sub> for VUV generation, but we have not attempted mixing in HD. For mixing in Kr, two-photon resonances in the 4p<sup>5</sup> 6p[5/2,2], 4p<sup>5</sup> 6p[3/2,2], and 4p<sup>5</sup> 6p[1/2,0] states may be accessed. However, the 4p<sup>5</sup> 6p[5/2,2] and 4p<sup>5</sup> 6p[1/2,0] lie in the wings of the ArF tuning range where the output power is reduced; therefore we have used only the 4p<sup>5</sup> 6p[3/2,2] transition for mixing in Kr. Seven two-photon resonances for H<sub>2</sub> lie within the tuning range of the ArF laser corresponding to Q-branch transitions to v=6 and 7 in the E-F state.<sup>3</sup> We use the Q(1) (6,0) transition most commonly for VUV generation because of the large Boltzmann fraction in J=1, and because the Q(1) (7,0) line lies in the wing of the tuning curve. (Note that the vibrational level v=6 in the E,F state is sometimes labeled v<sub>E</sub> = 2, which corresponds to the vibrational number of the inner (E) well of the double minimum E,F state.)

Both the Kr 6p[3/2,2] and H<sub>2</sub> Q(1) (6,0) transitions overlap with Schumann-Runge bands in oxygen, and the ArF path must be purged with argon. The absorption is particularly strong for the Kr 6p[3/2,2], which requires a more aggressive Ar purge than when tuning to the H<sub>2</sub> Q(1) (6,0) transition.

The selection of Kr or H<sub>2</sub> as the nonlinear mixing medium depends on the application. As discussed below, the nonlinear susceptibilities for the Kr 6p[3/2,2] and H<sub>2</sub> Q(1) (6,0) transitions are similar in magnitude near Lyman-α. When mixing in H<sub>2</sub>, VUV amplified spontaneous emission (ASE) is generated, as is discussed in Section 3A. In the region where the ASE is the strongest, approximately 135-160 nm, mixing in Kr is generally preferred to avoid the additional VUV from ASE. Near 135 nm and below, the phase mismatch for Kr becomes quite large due to the resonance lines at 123.58 and 116.49 nm (see Fig. 2). In this region mixing in H<sub>2</sub> provides higher powers than for Kr. Using a pyroelectric energy meter, we have directly measured 65 μJ at 133 nm when mixing in H<sub>2</sub>. Mixing in H<sub>2</sub> does not work well in the region of Lyman-α, as discussed in Section 3B. In the regions below the Kr resonances, the phase mismatch is negative in Kr, which allows the possibility of phase matching by adding a gas with positive phase mismatch as described in Section 3B.

## A. ASE

When the ArF is tuned to two-photon resonances in the E,F state for  $\text{H}_2$ <sup>44,74</sup> or HD,<sup>75</sup> sufficient population may be transferred from the ground state to cause ASE in the VUV. This ASE can occur due to population transfer from the E,F state to the B state through near infrared ASE followed by ASE from the B to X state (Lyman band emission). Although ASE from the C state to the X state (Werner bands) also can occur through electron collisional transfer from the E,F state to the C state,<sup>44</sup> we have only observed Lyman band emission. The Lyman band ASE occurs predominantly at wavelengths from about 135 nm to 160 nm. This ASE may be a nuisance when performing difference frequency generation. Although the optimum pressure for generation of ASE tends to be higher than the optimum pressure for difference frequency generation,<sup>4</sup> it is not possible to perform difference frequency generation in  $\text{H}_2$  without significant ASE generation. However, the VUV ASE can also serve a beneficial role for checking VUV system performance. The VUV ASE may be used to test the transmission of optics and mixing gases in the VUV independently from difference frequency mixing, which requires careful temporal and spatial overlaps of ArF and dye beams. The ASE may also be used as a source of discrete VUV lines.

A spectrum of ASE lines taken with a VUV spectrometer (SPEX model 1500SP) is shown in Fig. 4. This measurement was taken with a 100 cm lens and a  $\text{H}_2$  pressure of approximately 200 mbar when the excimer laser was tuned to the E,F ( $v'=6, J'=1$ ) level. Also shown are expected line positions for selected B  $\rightarrow$  X (Lyman band) transitions from Dabrowski.<sup>76</sup> The spectrum in Fig. 4 has not been corrected for the spectral response of the spectrometer and photomultiplier tube. Although the E,F  $\rightarrow$  B ASE can populate either  $J=2$  or  $J=0$  in the B state, we have only observed VUV ASE from  $J=2$  in the form of P(3) and R(1) emission; P(1) lines are not observed. B  $\rightarrow$  X transitions from  $v'=0$  to  $v''=4-8$  and  $v'=1$  to  $v''=5-9$  are observed. For each pair of lines, the P(3) emission is stronger than the R(1) emission. Only the P(3) line is observed for the (1,5) and (1,9) bands. A peak near 162.8 nm appears to be the (2,10) P(3) line. At this spectral resolution, it is not possible to resolve the (2,9) P(3), (2,8) P(3), and (2,8) R(1) lines from the (0,8) R(1), (0,7) P(3), and (0,7) R(1) lines, respectively. The unassigned line at 153.8

nm is due to a stray reflection of the ArF laser in the spectrometer; we have not identified the line near 161.4 nm.

In addition to the lines shown in Fig. 4, we have also observed ASE emission on the (1,2) Lyman band as shown in Fig. 5. ASE on this band has not been reported previously, to our knowledge. The general pattern of observed Lyman band ASE, such as reduced intensity between the (1,6) and (1,2) lines and the limited range for emission from  $v'=2$  agrees with the variation in the Franck-Condon factors (overlap of the vibrational wavefunctions in the B and X states) for these bands given by Spindler.<sup>77</sup>

## B. LYMAN- $\alpha$ GENERATION

Lyman- $\alpha$ , corresponding to the shortest wavelength connecting the ground state of H atoms at 121.567 nm is an important wavelength for spectroscopy, photochemistry, and plasma diagnostics. Nonlinear production of Lyman- $\alpha$  has been pursued by a number of groups using frequency tripling;<sup>5,6,10,14,64,65,78-87</sup> Raman shifting;<sup>9,22</sup> electromagnetically induced transparency;<sup>88</sup> and resonantly-enhanced four-wave mixing in Mg,<sup>89</sup> Hg,<sup>7,90,91</sup> and Kr;<sup>13,14,29,71</sup> We have investigated the performance of our VUV source at this wavelength.

VUV generation with H<sub>2</sub> produces about two orders of magnitude more energy than with Kr in the region of Lyman- $\alpha$ . The VUV energy generated near Lyman- $\alpha$  in 65 mbar of pure H<sub>2</sub> is shown as a function of VUV wavelength as the solid line in Fig. 6. A dramatic dip in VUV generations occurs at Lyman- $\alpha$  due to the production of H atoms. There is a strong asymmetry to this dip, with reduced efficiency in the long wavelength side. Others also have reported asymmetric dips near Lyman- $\alpha$  for VUV generation in H<sub>2</sub>.<sup>9,92,93</sup> The asymmetry is due to contributions of H atoms to the phase mismatch. The index of refraction of the H atoms varies rapidly near the strongly-allowed Lyman- $\alpha$  transition, which produces a profound effect on the phase matching. On the long wavelength side of Lyman- $\alpha$ , the phase-mismatch increases and conversion efficiency drops. On the short wavelength side, H atoms make a negative contribution

to  $\Delta k$  and improve the conversion efficiency through reduced phase mismatch. This interpretation is supported by measurements in negatively dispersive gases: when generating VUV in Kr with H<sub>2</sub> added, the asymmetry is reversed (see Fig. 7) because  $\Delta k$  for Kr is negative in this spectral region.

We have modeled the shape of the tuning profile in Fig. 6 by calculating values for the phase matching function,  $F$ , as a function of VUV wavelength. This calculation uses the phase mismatch per molecule for H<sub>2</sub> from Fig. 2, the measured H<sub>2</sub> pressure, and the confocal parameters determined for the fit in Fig. 9. The refractive index for H atoms is calculated from Equation (1) of Leonard<sup>56</sup> using calculated oscillator strengths,<sup>94</sup> and neglecting contributions from the continuum. This calculation is sufficiently accurate for our purpose. The H atom density is used as a fitting parameter. The resulting tuning profile for a H atom number density equal to 0.004 times the H<sub>2</sub> number density is shown as the dashed line in Fig. 6. The fit agrees qualitatively with the measurement except very near Lyman- $\alpha$ . Some disagreement between the measurement and fit is not surprising since the fit includes many approximations. For instance, the fit assumes a uniform H atom density over the full mixing length, while the H atoms are likely to drop significantly away from the focus.

There is additional reproducible structure in Fig. 6 that we believe is due to H<sub>2</sub> at 121.0, 121.2, 122.5, and 123 nm. We have not been able to conclusively assign these features. Possible sources of this structure are competition from  $2 + 1$  (2 ArF photons and one dye photon) absorption into H<sub>2</sub> Rydberg states or Werner band absorption by excited states produced by the VUV ASE described in Section 3A. Expected line positions from the literature for the Rydberg<sup>95</sup> and Werner<sup>76</sup> transitions are shown in Fig. 6.

We have tried unsuccessfully to avoid production of H atoms near Lyman- $\alpha$ . Reduction in H<sub>2</sub> pressure and ArF laser power and slight detunings of the ArF laser from resonance met with limited success, but none eliminated the drop in power at Lyman- $\alpha$ . Adjusting synchronization of the ArF and dye laser to encourage mixing before significant H atom production had no apparent effect. Although we could produce 5-15  $\mu\text{J}$  near Lyman- $\alpha$ , the maximum energy we were able to



produce at Lyman- $\alpha$  in  $H_2$  was 0.2  $\mu J$  (see Fig. 8). The zero level for the measurements in Fig. 8 was determined by changing the delay between the two lasers to prevent nonlinear mixing.

We have not identified the mechanism for generation of the H atoms. Emission at Balmer- $\alpha$  (656 nm) was observed in the focal region. The intensity of the Balmer- $\alpha$  radiation increases as roughly the third power of density before saturating and slowly decreasing above 13 mbar. Datkos et al.<sup>70</sup> have observed Lyman- $\alpha$  from ArF-irradiated  $H_2$ , which they attribute to electron attachment to high Rydberg states produced following absorption of three ArF photons.

Note that from Fig. 8 we observe VUV generation even directly at Lyman- $\alpha$ , while the H atoms concentrations estimated from Fig. 6 should absorb all Lyman- $\alpha$ . One possible explanation is that H atoms are predominantly produced at the laser focus while some Lyman- $\alpha$  is produced after the focal region. To summarize our results in pure  $H_2$ , we produce 5-15  $\mu J$  near Lyman- $\alpha$ , with a 1-2 order of magnitude dip on resonance where peak energies of about 0.2  $\mu J$  are produced.

The lower efficiency for Kr relative to  $H_2$  near Lyman- $\alpha$  is primarily due to the phase mismatch, not the nonlinear susceptibility  $\chi^{(3)}$ . At 121.46 nm,  $H_2$  has a maximum VUV power at a pressure of about 65 mbar, while Kr has a maximum at about 7 mbar in this region (both using a 50 cm lens). Thus without phase matching Kr has an experimentally measured optimum pressure that is about 10 times lower than for  $H_2$ . This is twice the calculated difference in phase mismatch between Kr and  $H_2$  given in Fig. 2 of  $C_{Kr} \sim -5 C_{H_2}$ . The discrepancy is primarily due to the phase mismatch from H atoms at the wavelength of 121.46 nm (see Fig. 6). Because the VUV power scales with the square of the gas density, phase mismatch alone should cause  $H_2$  to be a factor of about 100 times more efficient than Kr. Because we find that  $H_2$  produces about 100 time more energy than Kr, we expect the  $\chi^{(3)}$  for Kr and  $H_2$  should be roughly equivalent near Lyman- $\alpha$ .

We generated high energies at Lyman- $\alpha$  using a phase matched mixture of Kr and Ar. A mixture of Kr and  $H_2$  cannot be used because H atoms are generated even when the ArF laser is tuned to the Kr resonance (see Fig. 7). Kr and Ar were added gradually to the cell to enhance mixing, using typically four additions of each gas in alternation. A mixture ratio of 3.9:1 Ar/Kr

phase matches at Lyman- $\alpha$ , resulting in about two orders of magnitude increase in energy over pure Kr. By comparison, from the phase mismatch from Fig. 2, we expect a ratio of 4.7:1 Ar/Kr. The generated energy at a Kr partial pressure of 130 mbar is shown in Fig. 9 as a function of VUV wavelength. Seven  $\mu\text{J}$  are obtained at Lyman- $\alpha$ . Prospects for further increase in energies and implications for the tuning range are described elsewhere.<sup>71</sup>

There is a pronounced asymmetry in the tuning profile of Fig. 9. This asymmetry is too large to be produced by curvature in the dispersion of the Kr/Ar mixture. Such an asymmetry can be produced by unequal confocal parameters for the input beams as described in Section 2A. We fit a phase matched tuning curve to the data of Fig. 9 using Eqs. (2) to (5) and the phase mismatch data of Fig. 2. This fit is shown as the dashed line in Fig. 9. The fit uses values of  $b_1 = 0.6$  cm and  $\bar{b} = 4$ . We have also modeled the effects of an offset between the foci of the input beams<sup>51</sup> to study possible asymmetries. Although an offset reduces the frequency conversion efficiency, it produces no significant asymmetry.

#### 4. VUV MULTIPHOTON SPECTROSCOPY

We have applied VUV radiation generated with two-photon-resonant difference frequency mixing to two types of multiphoton excitation deep in the VUV; 1+1 REMPI (resonantly-enhanced multi-photon ionization) in Xe at 147 nm and two-photon excited fluorescence in Ne at 133 nm. For both of these experiments, separation of the VUV and pump beams was performed with a  $\text{MgF}_2$  Pellin Broca prism rather than the off-axis lens shown in Fig. 3.

##### A. 1+1 REMPI IN XENON

We used two photons at 147 nm to perform 1+1 REMPI through the  $5p^56s[3/2,1]$  state of xenon at  $68,045\text{ cm}^{-1}$ , as shown in the inset in Fig. 10. The 147-nm radiation was produced through mixing in Kr. Because VUV radiation can readily ionize many molecular species, background ion signals are a major consideration for VUV REMPI. With energies of only 3  $\mu\text{J}$ ,

we have obtained signal-to-noise ratios of over 50 for the ion signal, a good indication that this approach can give useful signals. A 1+1 REMPI spectrum and an absorption spectrum for Xe at a cell pressure of 0.065 mbar are shown in Fig. 10. The ion signal is collected with a single electrode biased at 25 V/cm. The strong resonance absorption in xenon leads to a dip in the REMPI signal at line center. At higher pressures, the ion signal drops to zero at line center. The power dependence of the ion signal from xenon at a pressure of 0.13 mbar is shown in Fig. 11. The signal follows the expected square dependence on the VUV power.

## **B. TWO-PHOTON-EXCITED FLUORESCENCE IN NEON**

We have also performed two-photon excited fluorescence from neon. Neon is the second most difficult element to excite from the ground state, after helium. Mixing in  $H_2$  was used to generate approximately 20  $\mu J$  at 133 nm. Two photons excite the  $2p^53p[3/2,2]$  state which lies 150,858.5  $cm^{-1}$  above the ground state. Fluorescence to the  $2p^53s[3/2,1]$  state at 610 nm is detected with a photomultiplier and a 700 nm short pass filter. The Ne pressure was approximately 130 mbar. Tuning the VUV demonstrates a linewidth at 133 nm of 1.8  $cm^{-1}$ . This linewidth is predominantly due to the linewidths of the ArF ( $\sim 1 cm^{-1}$ ) and frequency-doubled dye ( $\sim 1.5 cm^{-1}$ ) lasers. Additional details of these measurements are presented elsewhere.<sup>4</sup>

## **5. SUMMARY AND CONCLUSIONS**

We have shown that two-photon-resonant difference frequency mixing using an ArF laser is a practical method for production of high energies in the VUV. Mixing in Kr and  $H_2$  each have their relative advantages.  $H_2$  has a smaller phase mismatch, but the production of strong VUV ASE in the wavelength range of  $\sim 135$ -160 nm appears unavoidable in  $H_2$ . The negative phase mismatch in Kr below the first resonance at 123.58 nm allows phase matching using gas mixtures. We have not explored mixing in HD.

We have directly measured over 65  $\mu\text{J}$  at 133 nm when mixing in pure  $\text{H}_2$ , and 7  $\mu\text{J}$  at Lyman- $\alpha$  (121.567 nm) when mixing in a phase matched mixture of Kr and Ar. Mixing in  $\text{H}_2$  at Lyman- $\alpha$  is hampered by the production of H atoms, leading to poor VUV generation and an asymmetric tuning profile due to the phase mismatch of the H atoms. A physical basis is presented for the asymmetric tuning profile for the phase matched mixture of Kr and Ar. The utility of this source is demonstrated in two multiphoton VUV experiments: 1+1 REMPI in Xe at 147 nm and two-photon-excited fluorescence in neon at 133 nm.

### ACKNOWLEDGMENTS

This research was supported by the Air Force Office of Scientific Research under contracts F49620-90-C-0044, F49620-94-C-0027, and F49620-97-C0002. We acknowledge David L. Huestis of SRI International for numerous helpful discussions, Jean Lacoursière (now of TTI Medical) for providing his observations regarding the Molelectron energy meter, and Richard J. Exberger of NASA-Ames Research Center for the loan of the KBr photomultiplier tube. M. J. Banks was supported by the Research Experiences for Undergraduates Program of the National Science Foundation.

### REFERENCES

1. R. Hilbig and R. Wallenstein, "Resonant sum and difference frequency mixing in Hg," IEEE J. Quantum Electron. **19**, 1759-1770 (1983).
2. G. C. Herring, M. J. Dyer, L. E. Jusinski, and W. K. Bischel, "Two-photon-excited fluorescence spectroscopy of atomic fluorine at 170 nm," Opt. Lett. **13**, 360-362 (1988).

3. G. W. Faris and M. J. Dyer, "Raman-shifting ArF excimer laser radiation for vacuum-ultraviolet multiphoton spectroscopy," *J. Opt. Soc. Am. B* **10**, 2273-2286 (1993).
4. G. W. Faris and M. J. Dyer, "Two-photon excitation of neon at 133 nm," *Opt. Lett.* **18**, 382-384 (1993).
5. R. W. Dreyfus, P. Bogen, and H. Langer, "Atomic H and D concentrations and velocities measured with harmonically generated Lyman- $\alpha$  (1215Å) radiation," in *Laser Techniques for Extreme Ultraviolet Spectroscopy*, edited by T. J. McIlrath and R. R. Freeman (American Institute of Physics, New York, 1982), pp. 57-68.
6. K. G. H. Baldwin, J. P. Marangos, and D. D. Burgess, "Application of coherent VUV radiation to the measurement of Lyman- $\alpha$  absorption lineshapes in a dense Z-pinch plasma," *J. Phys. D* **17**, L169-L173 (1984).
7. G. C. Stutzin, A. T. Young, A. S. Schlachter, J. W. Stearns, K. N. Leung, W. B. Kunkel, G. T. Worth, and R. R. Stevens, "VUV laser absorption spectrometer system for measurement of H<sup>0</sup> density and temperature in a plasma," *Rev. Sci. Instrum.* **59**, 1363-1368 (1988).
8. H. F. Döbele, "Generation of coherent VUV radiation and its application to plasma diagnostics," *Plasma Sources Sci. Technol.* **4**, 224-233 (1995).
9. D. Wagner, B. Dikmen, and H. F. Döbele, "Vacuum ultraviolet absorption spectroscopy in the spectral interval of Lyman- $\alpha$  of atomic hydrogen and deuterium in an ion source plasma," *Rev. Sci. Instrum.* **67**, 1800-1806 (1996).
10. Ph. Mertens and M. Silz, "Radial profiles of atomic deuterium measured in the boundary of TEXTOR 94 with laser-induced fluorescence," *J. Nucl. Mater.* **241-243**, 842-847 (1997).

11. S. A. Meyer, D. Bershader, and S. P. Sharma, "Resonance broadening measurements of atomic oxygen at 130 nm," *Journal of Quantitative Spectroscopy and Radiative Transfer* **60**, 53-68 (1998).
12. A. V. Kanaev, V. Zafiropulos, M. Ait-Kaci, L. Museur, H. Nkwawo, and M. C. Castex, "Excimer formation mechanism in gaseous krypton and Kr/N<sub>2</sub> mixtures," *Z. Phys. D* **27**, 29-37 (1993).
13. R. A. Brownsword, M. Hillenkamp, T. Laurent, R. K. Vatsa, H.-R. Volpp, and J. Wolfrum, "Photodissociation dynamics of the chloromethanes at the Lyman- $\alpha$  wavelength (121.6 nm)," *J. Chem. Phys.* **106**, 1359-1366 (1997).
14. P. Löffler, E. Wrede, L. Schnieder, J. B. Halpern, W. M. Jackson, and K. H. Welge, "Dissociation dynamics of acetylene Rydberg states as a function of excited state lifetime," *J. Chem. Phys.* **109**, 5231-5246 (1998).
15. J. Lacoursière, S. A. Meyer, G. W. Faris, T. G. Slanger, B. R. Lewis, and S. T. Gibson, "The O(<sup>1</sup>D) Yield from O<sub>2</sub> photodissociation near H Lyman- $\alpha$  (121.6 nm)," *J. Chem. Phys.* **110**, 1949-1958 (1999).
16. R. T. Hodgson, P. P. Sorokin, and J. J. Wynne, "Tunable coherent vacuum-ultraviolet generation in atomic vapors," *Phys. Rev. Lett.* **32**, 343-346 (1974).
17. W. Jamroz and B. P. Stoicheff, "Generation of tunable coherent vacuum-ultraviolet radiation," in *Progress in Optics XX*, edited by E. Wolf (North-Holland, Amsterdam, 1983), pp. 325-381.
18. J. F. Reintjes, *Nonlinear Optical Parametric Processes in Liquids and Gases* (Academic Press, Inc., New York, 1984).

19. R. Hilbig, G. Hilber, A. Lago, B. Wolff, and R. Wallenstein, "Tunable coherent VUV radiation generated by nonlinear optical frequency conversion in gases," *Comments At. Mol. Phys.* **18**, 157-180 (1986).
20. C. R. Vidal, "Four-wave frequency mixing in gases," in *Tunable Lasers*, edited by L. F. Mollenauer and J. C. White (Springer-Verlag, Berlin, 1987), Vol. 59, pp. 57-113.
21. H. F. Döbele, M. Hörl, and M. Röwenkamp, "Tuning ranges of KrF and ArF excimer laser amplifiers and of associated vacuum ultraviolet anti-Stokes Raman lines," *Appl. Phys. B* **42**, 67-72 (1987).
22. P. Bogen, Ph. Mertens, E. Pasch, and H. F. Döbele, "Detection of atomic oxygen and hydrogen in the vacuum UV using a frequency-doubled, Raman-shifted dye laser," *J. Opt. Soc. Am. B* **9**, 2137-2141 (1992).
23. A. Goehlich, U. Czarnetzki, and H. F. Döbele, "Increased efficiency of vacuum ultraviolet generation by stimulated anti-Stokes Raman scattering with Stokes seeding," *Appl. Opt.* **37**, 8453-8459 (1998).
24. F. Seifert, J. Ringling, F. Noack, V. Petrov, and O. Kittelmann, "Generation of tunable femtosecond pulses to as low as 172.7 nm by sum-frequency mixing in lithium triborate," *Opt. Lett.* **19**, 1538-1540 (1994).
25. V. Petrov, F. Rotermund, F. Noack, R. Komatsu, T. Sugawara, and S. Uda, "Vacuum ultraviolet application of  $\text{Li}_2\text{B}_4\text{O}_7$  crystals: Generation of 100 fs pulses down to 170 nm," *J. Appl. Phys.* **84**, 5887-5892 (1998).
26. V. I. Gladushchak, S. A. Moshkalev, G. T. Razdobarin, and E. Ya. Shreider, "Coherent sources of vacuum ultraviolet radiation," *Sov. Phys. Tech. Phys.* **31**, 855-873 (1986).

27. S. M. Hooker and C. E. Webb, "Progress in vacuum-ultraviolet lasers," *Progress in Quantum Electronics* **18**, 227-274 (1994).
28. G. Hilber, A. Lago, and R. Wallenstein, "Broadly tunable vacuum-ultraviolet/extreme-ultraviolet radiation generated by resonant third-order frequency conversion in krypton," *J. Opt. Soc. Am. B* **4**, 1753-1764 (1987).
29. J. P. Marangos, N. Shen, H. Ma, M. H. R. Hutchinson, and J. P. Connerade, "Broadly tunable vacuum-ultraviolet radiation source employing resonant enhanced sum-difference frequency mixing in krypton," *J. Opt. Soc. Am. B* **7**, 1254-1259 (1990).
30. C. H. Muller, III, D. D. Lowenthal, M. A. DeFaccio, and A. V. Smith, "High-efficiency, energy-scalable, coherent 130-nm source by four-wave mixing in Hg vapor," *Opt. Lett.* **13**, 651-653 (1988).
31. Y.-M. Yiu, K. D. Bonin, and T. J. McIlrath, "Two-photon resonant upconversion in xenon," *Opt. Lett.* **7**, 268-270 (1982).
32. R. Hilbig and R. Wallenstein, "Tunable VUV radiation generated by two-photon resonant frequency mixing in xenon," *IEEE J. Quantum Electron.* **19**, 194-201 (1983).
33. K. Tsukiyama, M. Momose, M. Tsukakoshi, and T. Kasuya, "Generation of XUV radiation by four-wave mixing in CO," *Opt. Commun.* **79**, 88-92 (1990).
34. N. Melikechi, S. Gangopadhyay, and E. E. Eyler, "Generation of vacuum ultraviolet radiation for precision laser spectroscopy," *Appl. Opt.* **36**, 7776-7778 (1997).
35. G. Z. Zhang, D. W. Tokaryk, B. P. Stoicheff, and K. Hakuta, "Nonlinear generation of extreme-ultraviolet radiation in atomic hydrogen using electromagnetically induced transparency," *Phys. Rev. A* **56**, 813-819 (1997).



36. W. K. Bischel, J. Bokor, D. J. Kligler, and C. K. Rhodes, "Nonlinear optical processes in atoms and molecules using rare-gas halide lasers," *IEEE J. Quantum Electron.* **15**, 380-392 (1979).
37. R. Hilbig, G. Hilber, A. Timmerman, and R. Wallenstein, "Broadly tunable VUV radiation generated by frequency mixing in gases," in *Laser Techniques in the Extreme Ultraviolet*, edited by S. E. Harris and T. B. Lucatorto (American Institute of Physics, New York, 1984), pp. 1-9.
38. C. E. M. Strauss and D. J. Funk, "Broadly tunable difference-frequency generation of VUV using two-photon resonances in  $H_2$  and Kr," *Opt. Lett.* **16**, 1192-1194 (1991).
39. G. W. Faris and M. J. Dyer, "Multiphoton spectroscopy using tunable VUV radiation from a Raman-shifted excimer laser," in *Short-Wavelength Coherent Radiation: Generation and Applications*, edited by Phillip H. Bucksbaum and Natale M. Ceglio (Optical Society of America, Washington, DC, 1991), pp. 58-61.
40. O. Kittelmann, J. Ringling, G. Korn, A. Nazarkin, and I. V. Hertel, "Generation of broadly tunable femtosecond vacuum-ultraviolet pulses," *Opt. Lett.* **21**, 1159-1161 (1996).
41. Y. Hirakawa, T. Okada, M. Maeda, and K. Muraoka, "Coherent extreme-ultraviolet generation at 64 nm by efficient frequency tripling of an ArF laser," *J. Opt. Soc. Am. B* **14**, 1029-1034 (1997).
42. T. Srinivasan, H. Egger, H. Pummer, and C. K. Rhodes, "Generation of extreme ultraviolet radiation at 79 nm by sum frequency mixing," *IEEE J. Quantum Electron.* **19**, 1270-1276 (1983).
43. Y. Hirakawa, A. Nagai, K. Muraoka, T. Okada, and M. Maeda, "Generation of tunable coherent extreme-ultraviolet radiation at wavelengths as low as 66 nm by resonant four-wave mixing," *Opt. Lett.* **18**, 735-737 (1993).

44. H. Pummer, H. Egger, T. S. Luk, T. Srinivasan, and C. K. Rhodes, "Vacuum-ultraviolet stimulated emission from two-photon-excited molecular hydrogen," *Phys. Rev. A* **28**, 795-801 (1983).
45. T. R. Loree, R. C. Sze, D. L. Barker, and P. B. Scott, "New lines in the UV: SRS of excimer laser wavelengths," *IEEE J. Quantum Electron.* **15**, 337-342 (1979).
46. R. S. Hargrove and J. A. Paisner, "Tunable, efficient VUV generation using ArF-pumped, stimulated Raman scattering in  $H_2$ ," Paper ThA6, in *Digest of Topical Meeting on Excimer Lasers* (Optical Society of America, Washington, DC, 1979).
47. M. Shahidi, T. S. Luk, and C. K. Rhodes, "Generation of infrared and extreme-ultraviolet radiation in krypton with picosecond irradiation at 193 nm," *J. Opt. Soc. Am. B* **5**, 2386-2394 (1988).
48. U. Czarnetzki, U. Wojak, and H. F. Döbele, "Observation of stimulated hyper-Raman scattering in  $H_2$ ," *Phys. Rev. A* **40**, 6120-6123 (1989).
49. U. Czarnetzki and H. F. Döbele, "Generation of vacuum-ultraviolet radiation in  $H_2$  by nonlinear optical processes near the EF- and B-state resonances," *Phys. Rev. A* **44**, 7530-7546 (1991).
50. G. C. Bjorklund, "Effects of focusing on third-order nonlinear processes in isotropic media," *IEEE J. Quantum Electron.* **11**, 287-296 (1975).
51. G. Hilber, D. J. Brink, A. Lago, and R. Wallenstein, "Optical-frequency conversion in gases using Gaussian laser beams with different confocal parameters," *Phys. Rev. A* **38**, 6231-6239 (1988).
52. A. Lago, G. Hilber, and R. Wallenstein, "Optical-frequency conversion in gaseous media," *Phys. Rev. A* **36**, 3827-3836 (1987).

53. To achieve agreement with references 50 and 52, and the figures of reference 51, we use only positive  $k$  values in equation 3 of reference 51. We do use a negative sign for the parametrized distance,  $\epsilon$ , for the difference (dye) wavelength.
54. J. F. Ward and G. H. C. New, "Optical third harmonic generation in gases by a focused laser beam," *Phys. Rev.* **185**, 57-72 (1969).
55. A. E. Siegman, *Lasers* (University Science Books, Mill Valley, California, 1986), pp. 682-685.
56. P. J. Leonard, "Refractive indices, Verdet constants, and polarizabilities of the inert gases," *Atomic Data and Nuclear Data Tables* **14**, 21-37 (1974).
57. G. I. Chashchina, V. I. Gladushchak, and E. Ya. Shreider, "Determination of the refractive index of argon and the oscillator strength of its resonance lines," *Opt. Spectrosc.* **24**, 542-543 (1968).
58. P. D. Chopra and D. W. O. Heddle, "Polarization free measurements of Rayleigh scattering of Lyman  $\alpha$ ," *J. Phys. B* **7**, 2421-2428 (1974).
59. W. R. Ferrell, M. G. Payne, and W. R. Garrett, "Determination of optical constants of noble gases through multiphoton ionization measurements," *Phys. Rev. A* **35**, 5020-5031 (1987).
60. R. J. Gordon, S.-P. Lu, S. M. Park, K. Trentelman, Y. Xie, L. Zhu, A. Kumar, and W. J. Meath, "The use of coherent phase control of multiphoton ionization to measure the refractive indices of  $H_2$  and Ar between 1100 and 1150 Å," *J. Chem. Phys.* **98**, 9481-9486 (1993).
61. A. Bideau-Mehu, Y. Guern, R. Abjean, and A. Johannin-Gilles, "Measurement of refractive indices of neon, argon, krypton and xenon in the 253.7-140.4 nm wavelength range. Dispersion relations and estimated oscillator strengths of the resonance lines," *J. Quant. Spectrosc. Radiat. Transfer* **25**, 395-402 (1981).

62. G. I. Chashchina and E. Ya. Shreider, "Determination of hydrogen refraction in the vacuum spectral range," *Opt. Spectrosc.* **66**, 274-275 (1989).
63. M. O. Bulanin and I. M. Kislyakov, "Dynamic polarizabilities of rare-gas atoms. krypton and xenon," *Opt. Spectrosc.* **85**, 819-825 (1998).
64. R. Mahon, T. J. McIlrath, V. P. Myerscough, and D. W. Koopman, "Third-harmonic generation in argon, krypton, and xenon: Bandwidth limitations in the vicinity of Lyman- $\alpha$ ," *IEEE J. Quantum Electron.* **15**, 444-451 (1979).
65. R. Mahon, T. J. McIlrath, and D. W. Koopman, "Nonlinear generation of Lyman-alpha radiation," *Appl. Phys. Lett.* **33**, 305-307 (1978).
66. V. P. Gladushchak, S. A. Moshkalev, G. I. Chashchina, and E. Ya. Shreider, "Use of third-harmonic generation for determining the refractive indices of gases in the vacuum ultraviolet spectral region," *Opt. Spectrosc.* **51**, 608-609 (1981).
67. H. Puell, H. Scheingraber, and C. R. Vidal, "Saturation of resonant third-harmonic generation in phase-matched systems," *Phys. Rev. A* **22**, 1165-1178 (1980).
68. H. Scheingraber and C. R. Vidal, "Saturation of resonant third-harmonic generation due to self-defocusing and a redistribution of the population densities," *IEEE J. Quantum Electron.* **19**, 1747-1758 (1983).
69. J. C. Miller, "Two-photon resonant multiphoton ionization and stimulated emission in krypton and xenon," *Phys. Rev. A* **40**, 6969-6976 (1989).
70. P. G. Datskos, L. A. Pinnaduwege, and J. F. Kielkopf, "Photophysical and electron attachment properties of ArF-excimer-laser irradiated H<sub>2</sub>," *Phys. Rev. A* **55**, 4131-4142 (1997).

71. S. A. Meyer and G. W. Faris, "High-power Lyman- $\alpha$  source generated with an ArF excimer laser," *Opt. Lett.* **23**, 204-206 (1998).
72. M. Krumrey, E. Tegeler, J. Barth, M. Krisch, F. Schäfers, and R. Wolf, "Schottky type photodiodes as detectors in the VUV and soft x-ray range," *Appl. Opt.* **27**, 4336-4341 (1988).
73. J. A. R. Samson, *Techniques of Vacuum Ultraviolet Spectroscopy* (Pied Publications, Lincoln, Nebraska, 1967), pp. 263-295.
74. U. Czarnetzki, H. F. Döbele, and B. Rückle, "Stimulated IR- and vacuum-UV emission following two-photon-excitation of molecular hydrogen using an ArF laser," *Appl. Phys. B* **48**, 37-40 (1989).
75. T. S. Luk, H. Egger, W. Müller, H. Pummer, and C. K. Rhodes, "The observation of stimulated emission in the 119 to 149 nm range from HD excited by picosecond 193 nm radiation," *H. Chem. Phys.* **82**, 4479-4482 (1985).
76. I. Dabrowski, "The Lyman and Werner bands of H<sub>2</sub>," *Can. J. Phys.* **62**, 1639-1664 (1984).
77. R. J. Spindler, Jr., "Franck-Condon factors for band systems of molecular hydrogen—I," *J. Quant. Spectrosc. Radiat. Transfer* **9**, 597-626 (1969).
78. S. A. Batishche, V. S. Burakov, V. G. Voronin, V. I. Gladushchak, V. A. Mostovnikov, P. A. Naumenkov, G. T. Razdobarin, A. N. Rubinov, V. V. Semenov, N. V. Tarasenko, and E. Ya. Shreider, "Laser action near the L $\alpha$  line in hydrogen and deuterium," *Sov. Tech. Phys. Lett.* **3**, 473 (1977).
79. D. Cotter, "Tunable, narrow-band coherent VUV source for the Lyman-alpha region," *Opt. Commun.* **31**, 397-400 (1979).

80. R. Wallenstein, "Generation of narrowband tunable VUV Radiation at the Lyman- $\alpha$  Wavelength," *Opt. Commun.* **33**, 119-122 (1980).
81. H. Langer, H. Puell, and H. Röhr, "Lyman alpha (1216 Å) generation in krypton," *Opt. Commun.* **34**, 137-142 (1980).
82. R. Mahon and Y. M. Yiu, "Generation of Lyman- $\alpha$  radiation in phase-matched rare-gas mixtures," *Opt. Lett.* **5**, 279-281 (1980).
83. H. Zacharias, H. Rottke, J. Danon, and K. H. Welge, "Resonant two photon ionization of H and D atoms," *Opt. Commun.* **37**, 15-19 (1981).
84. R. Hilbig and R. Wallenstein, "Enhanced production of tunable vuv radiation by phase-matched frequency tripling in krypton and xenon," *IEEE J. Quantum Electron.* **17**, 1566-1573 (1981).
85. S. Himeno, E. Noda, Q. Q. Lü, S. Kogoshi, Y. Iida, M. Katsurai, and T. Sekiguchi, "Generation of coherent Lyman-alpha radiation with an alexandrite laser for diagnostics of neutral hydrogen density," *Journal of Nuclear Materials* **128-129**, 974-976 (1984).
86. L. Cabaret, C. Delsart, and C. Blondel, "High resolution spectroscopy of the hydrogen Lyman- $\alpha$  line Stark structure using a VUV single mode pulsed laser system," *Opt. Commun.* **61**, 116-119 (1987).
87. Ph. Mertens and P. Bogen, "Densities and velocity distributions of atomic hydrogen and carbon, measured by laser-induced fluorescence with frequency-tripling into the vacuum UV," *Appl. Phys. A* **43**, 197-204 (1987).
88. K. Hakuta, L. Marmet, and B. P. Stoicheff, "Nonlinear optical generation with reduced absorption using electric-field coupling in atomic hydrogen," *Phys. Rev A* **45**, 5152-5159 (1992).

89. T. J. McKee, B. P. Stoicheff, and S. C. Wallace, "Tunable, coherent radiation in the Lyman- $\alpha$  region (1210-1290 Å) using magnesium vapor," *Opt. Lett.* **3**, 207-208 (1978).
90. R. S. Turley, R. A. McFarlane, J. Remillard, and D. G. Steel, "Production of intense, coherent, tunable, narrow-band Lyman-alpha radiation," *Proc. SPIE* **912**, 116-121 (1988).
91. K. Eikema, J. Walz, and T. Hansch, "Continuous wave coherent Lyman-alpha radiation," *Physical Review Letters* **83**, 3828-3831 (1999).
92. F. G. Celii, H. R. Thorsheim, J. E. Butler, L. S. Plano, and J. M. Pinneo, "Detection of ground-state atomic hydrogen in a dc plasma using third-harmonic generation," *J. Appl. Phys.* **68**, 3814-3817 (1990).
93. C. E. M. Strauss, personal communication, 1997.
94. W. L. Wiese and G. A. Martin, "Atomic transition probabilities," in *CRC Handbook of Chemistry and Physics*, 59th edition, edited by Robert C. Weast (CRC Press, West Palm Beach, Florida, 1978), pp. D112-D140.
95. G. Herzberg and C. Jungen, "Rydberg series and ionization potential of the H<sub>2</sub> molecule," *J. Mol. Spectrosc.* **41**, 425-486 (1972).
96. P. L. Smith, M. C. E. Huber, and W. H. Parkinson, "Refractivities of H<sub>2</sub>, He, O<sub>2</sub>, CO, and Kr for  $168 \leq \lambda \leq 288$  nm," *Phys. Rev. A* **13**, 1422-1434 (1976).

## FIGURE CAPTIONS

Figure 1. Vibration curves for three cases of four-wave mixing. (a) third harmonic generation, (b) difference frequency mixing for  $\bar{b}=1$ , and (c) difference frequency mixing for  $\bar{b}=4$ . Inset graphs show the phasematching integral  $F$  as a function of  $b_1\Delta k$ .

Figure 2. Phase mismatch per atom or molecule for Kr, Ar, and  $H_2$  for two-photon-resonant difference frequency mixing with an ArF excimer laser. Regions of negative phase mismatch for Kr are indicated with dashed lines.

Figure 3. Experimental arrangement for vuv generation. Wavelengths shown are for Lyman- $\alpha$  generation.

Figure 4. Vacuum ultraviolet amplified spontaneous emission generated on pumping the  $E,F\ ^1\Sigma_g^+$  ( $v'=6$ )  $\leftarrow X\ ^1\Sigma_g^+$  ( $v''=0$ ) Q(1) transition in  $H_2$ . The emission strengths have not been corrected for the spectral response of the spectrometer and photomultiplier tube. Lyman band line positions are shown at the top of the figure.

Figure 5. Vacuum ultraviolet amplified spontaneous emission on the (1,2) Lyman band.

Figure 6. VUV energy generated in pure  $H_2$  in the region of Lyman- $\alpha$  at a pressure of 65 mbar. The dashed line is a theoretical tuning profile using Eqs. (2)-(5). Possible line assignments for spectral features are shown at the top of the figure.

Figure 7. VUV generation near Lyman- $\alpha$  using pure Kr and a mixture of Kr and  $H_2$ .

Figure 8. Expanded view of Lyman- $\alpha$  generation in pure  $H_2$ . The upper curve has been multiplied by a factor of ten.



Figure 9. VUV generation in a phasematched mixture of Kr and Ar at Lyman- $\alpha$  (solid line) and fit tuning profile from Eqs. (2)-(5).

Figure 10. Transmission (a) and 1+1 REMPI (b) spectra for xenon with 147-nm radiation. Energy level diagram for 1+1 REMPI is shown as inset.

Figure 11. Power dependence of ion signal from 1+1 REMPI in xenon.

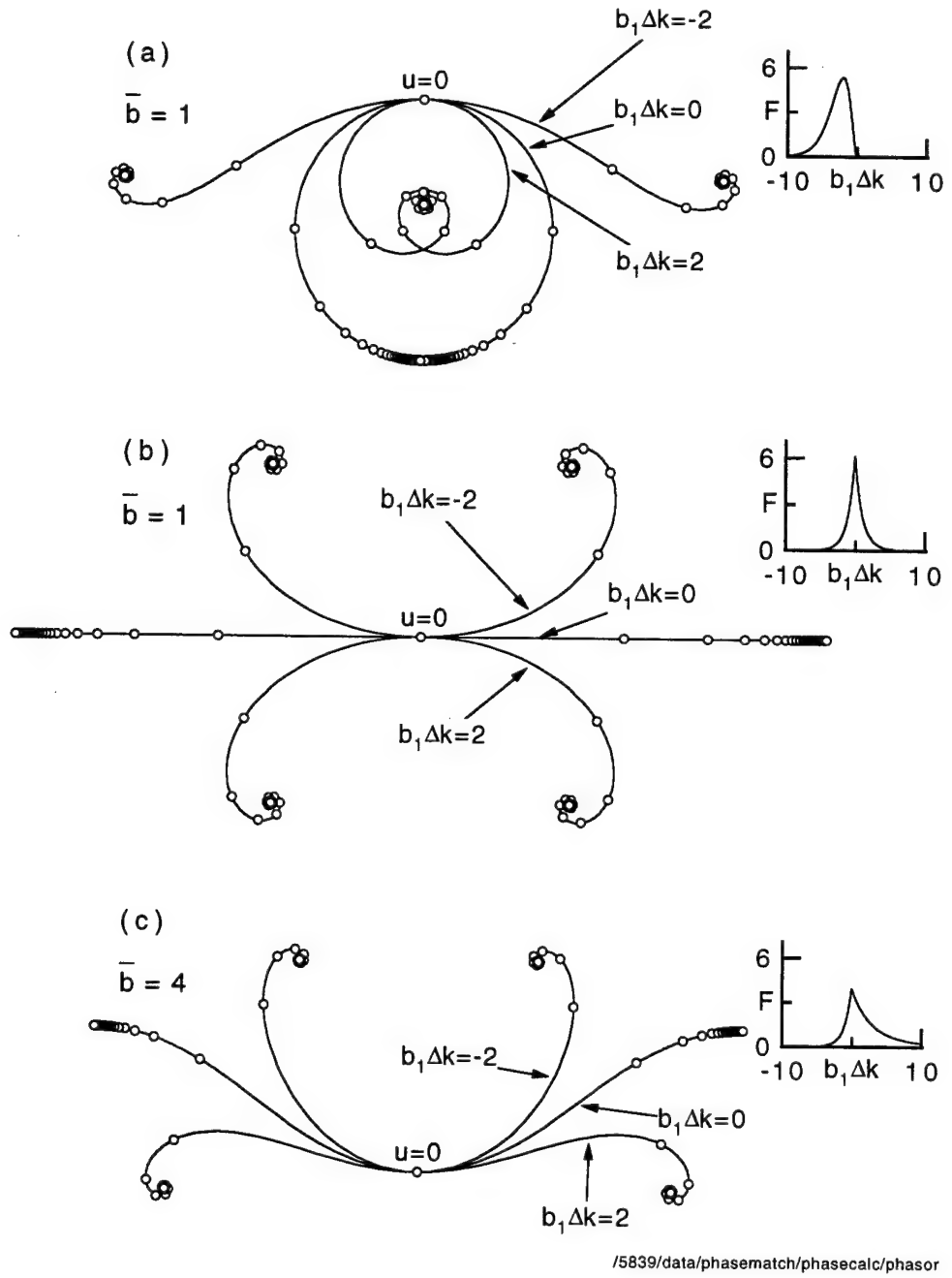


Figure 1. Vibration curves for three cases of four-wave mixing. (a) third harmonic generation, (b) difference frequency mixing for  $\bar{b}=1$ , and (c) difference frequency mixing for  $\bar{b}=4$ . Inset graphs show phasematching integral as a function of  $b_1 \Delta k$ .

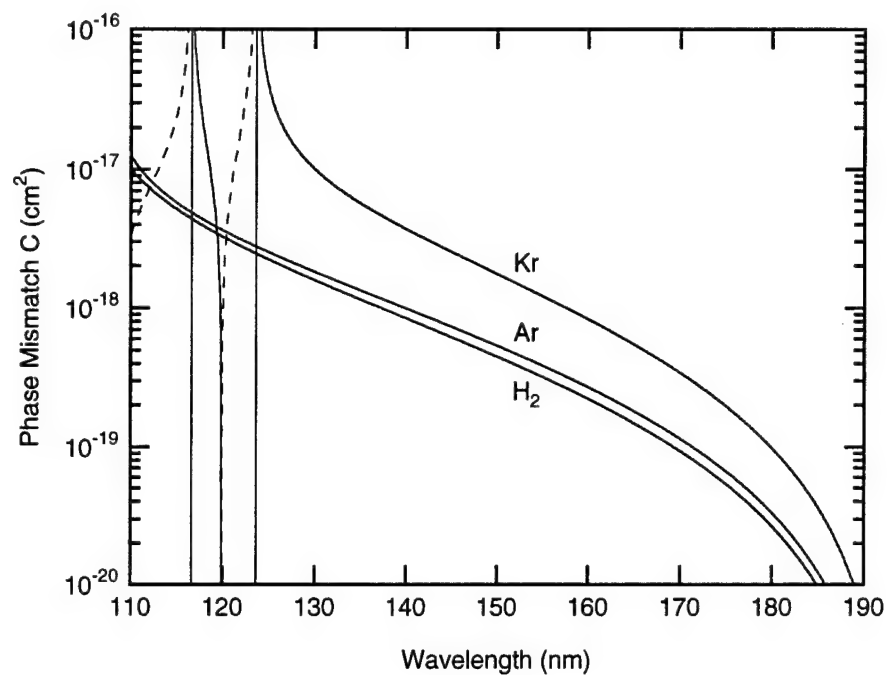


Figure 2. Phase mismatch per atom or molecule for Kr, Ar, and H<sub>2</sub> for two-photon-resonant difference frequency mixing using an ArF excimer laser. Regions of negative phase mismatch for Kr are marked with dashed lines.

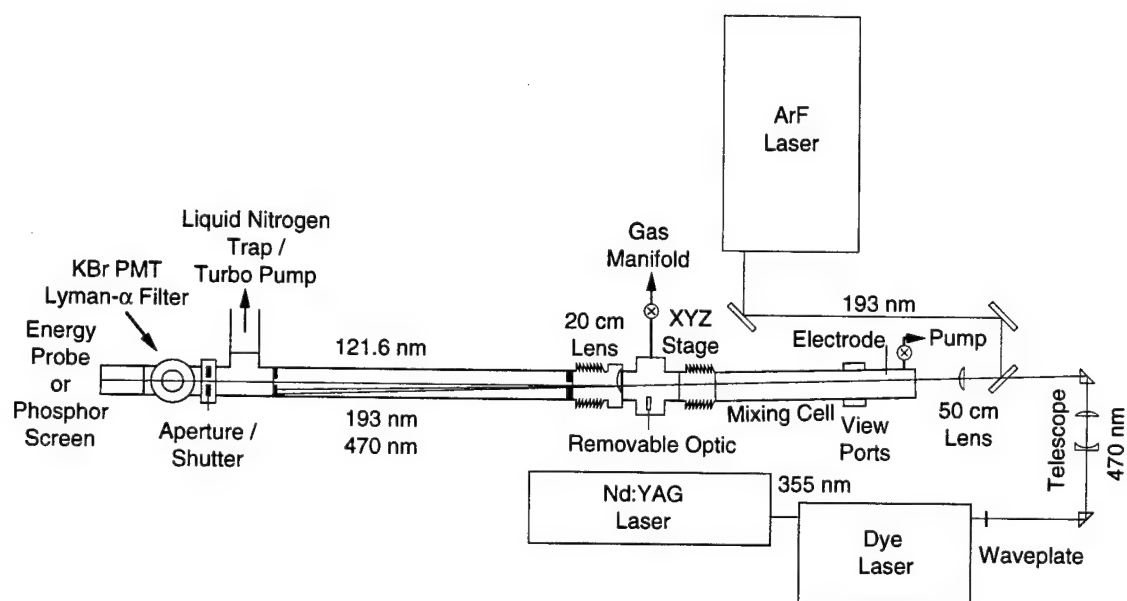


Figure 3. Experimental arrangement for vuv generation. Wavelengths shown are for Lyman- $\alpha$  generation.

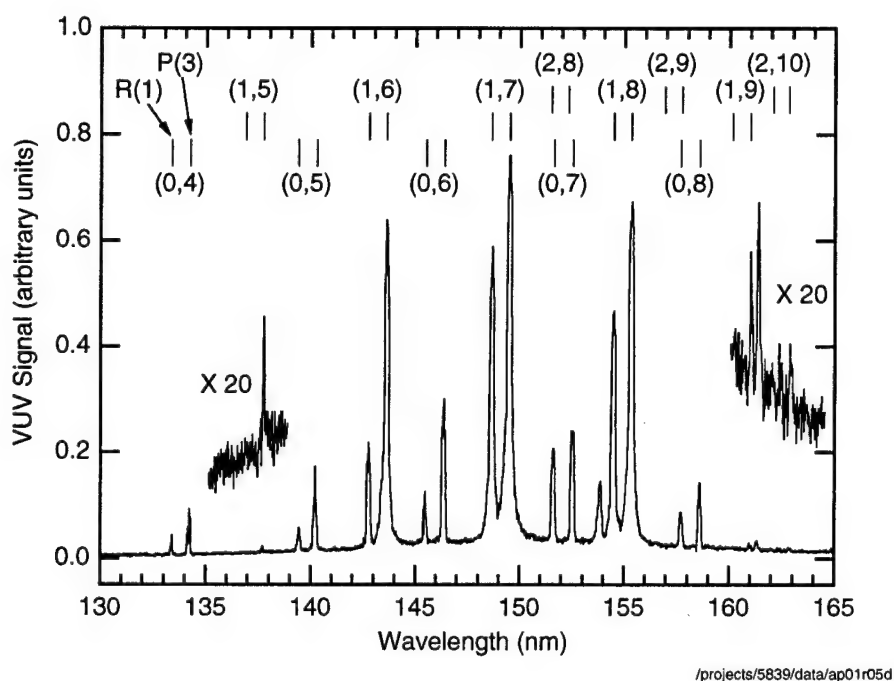


Figure 4. Vacuum ultraviolet amplified spontaneous emission generated on pumping the  $E,F\ ^1\Sigma_g^+$  ( $v'=6$ )  $\leftarrow X\ ^1\Sigma_g^+$  ( $v''=0$ ) Q(1) transition in  $H_2$ . The emission strengths have not been corrected for the spectral response of the spectrometer and photomultiplier tube. Lyman band line positions are shown at the top of the figure.

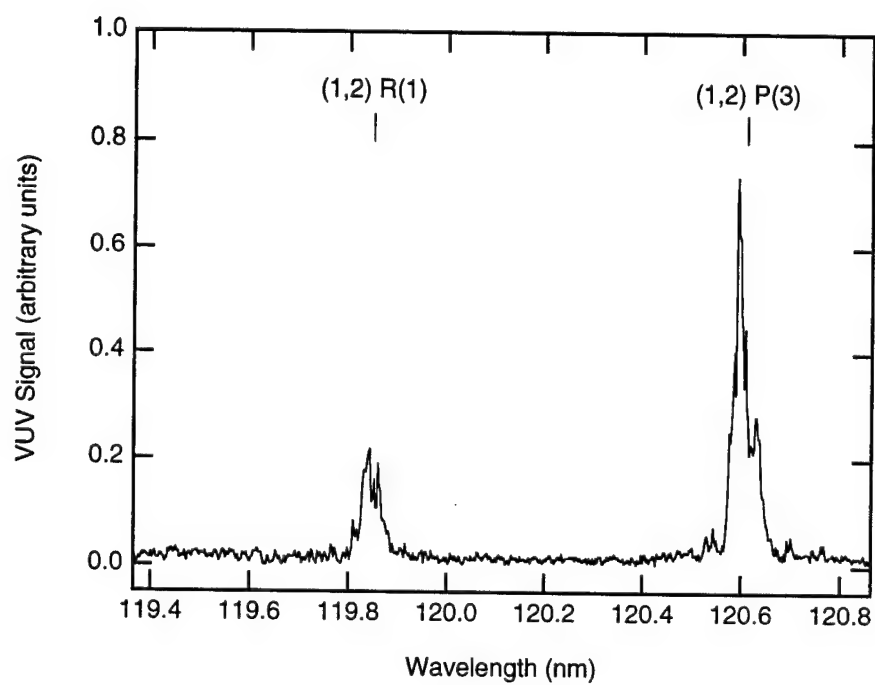


Figure 5. Vacuum ultraviolet amplified spontaneous emission on (1,2) Lyman band.

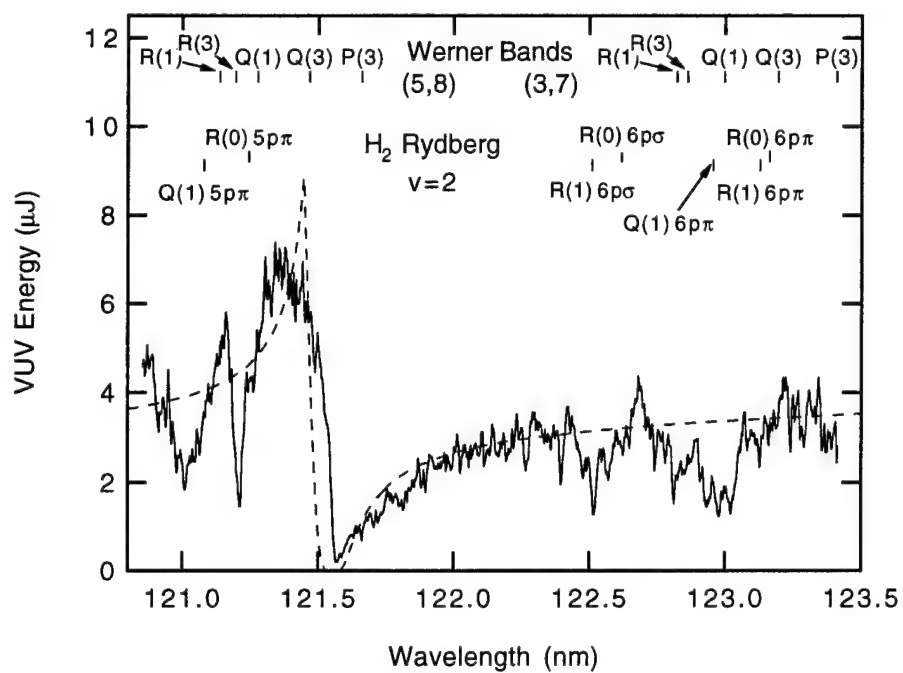


Figure 6. VUV energy generated in pure  $H_2$  in the region of Lyman- $\alpha$  at a pressure of 65 mbar. The dashed line is a theoretical tuning profile using Eqs. (2)-(5). Possible line assignments for spectral features are shown at the top of the figure.

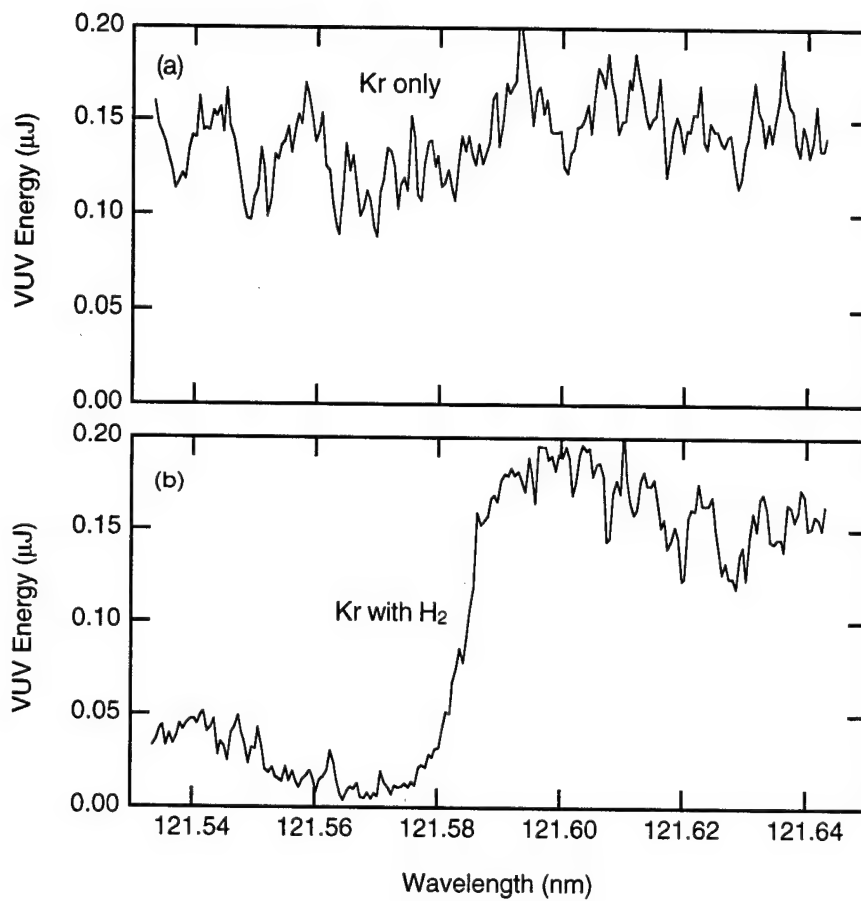


Figure 7. VUV generation near Lyman- $\alpha$  using pure Kr and Kr/H<sub>2</sub> mixture.



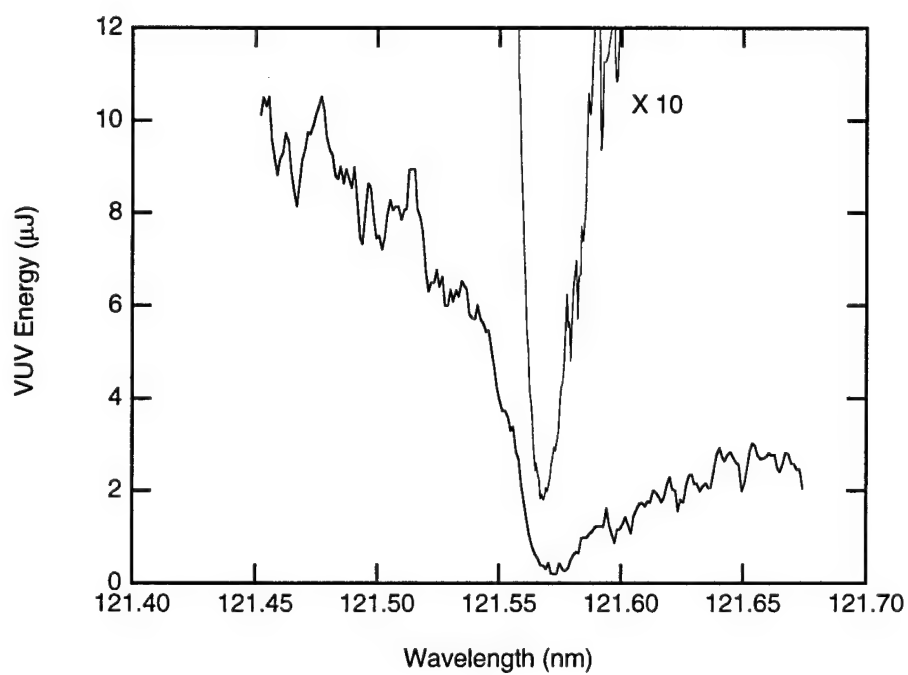


Figure 8. Expanded view of Lyman- $\alpha$  generation in pure H<sub>2</sub>. Upper curve has been multiplied by a factor of ten.

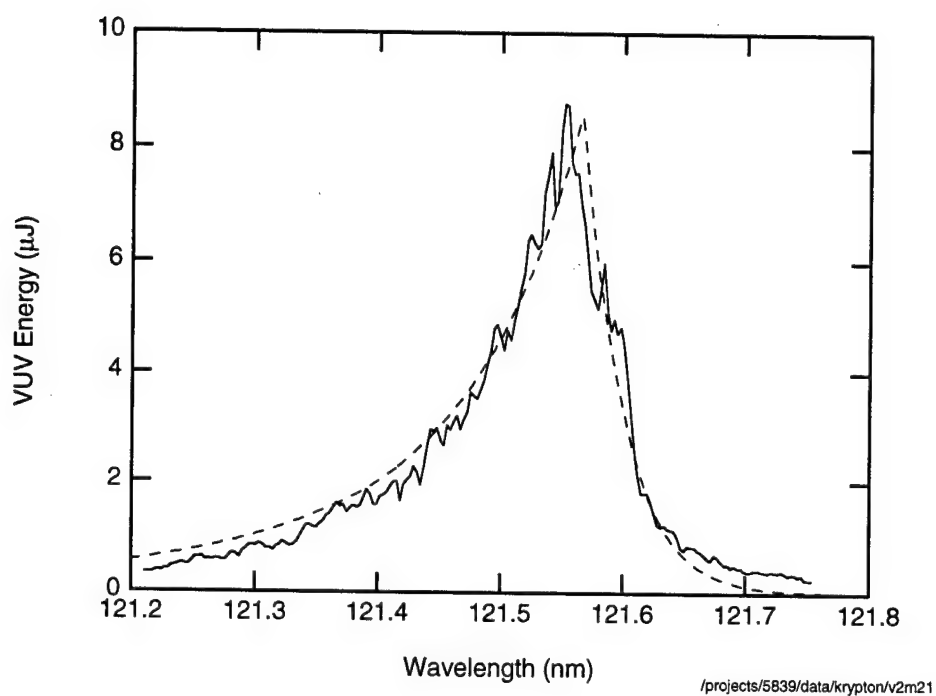


Figure 9. VUV generation in phasematched Kr/Ar mixture at Lyman- $\alpha$  (solid line) and fit tuning profile from Eqs. (2)-(5).

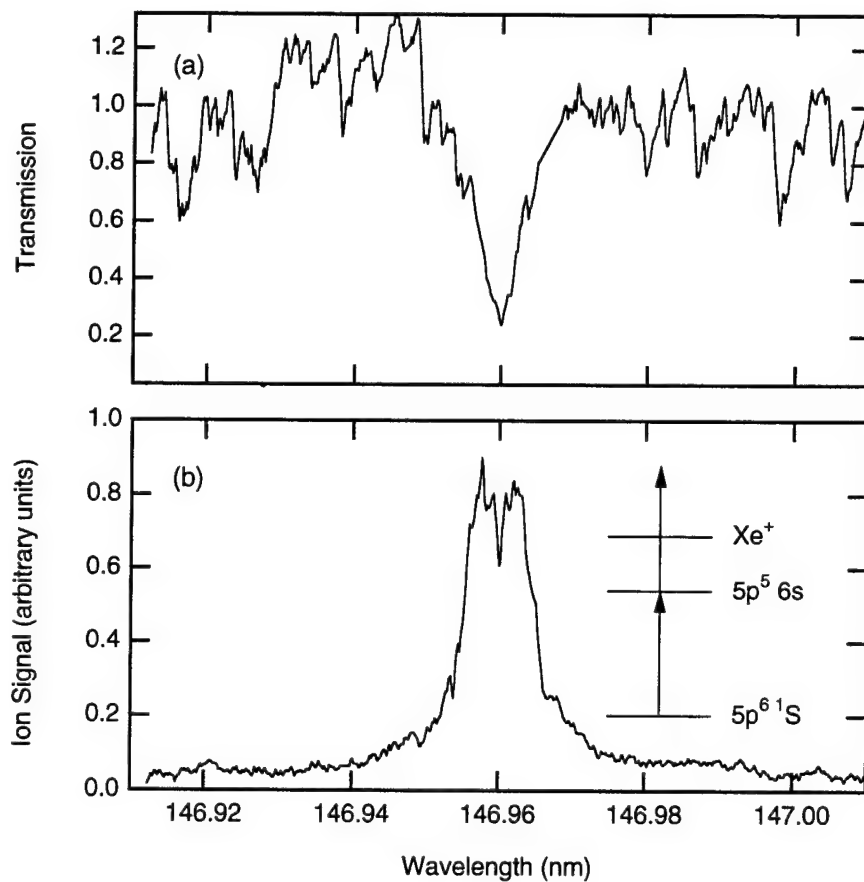


Figure 10. Transmission (a) and 1+1 REMPI (b) spectra for xenon with 147-nm radiation. Energy level diagram for 1+1 REMPI is shown as inset.

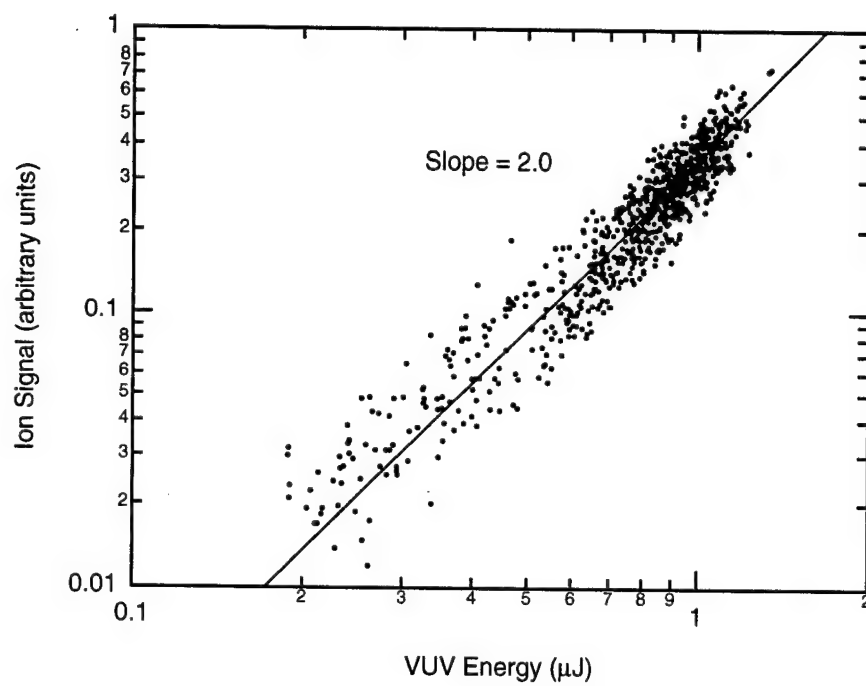


Figure 11. Power dependence of ion signal from 1+1 REMPI in xenon.

## **APPENDIX D**

**HIGH POWER LYMAN ALPHA SOURCE GENERATED WITH AN ARF  
EXCIMER LASER, OPT. LETT. 23, 204-206 (1998).**

# High-power Lyman- $\alpha$ source generated with an ArF excimer laser

Scott A. Meyer and Gregory W. Faris

Molecular Physics Laboratory, SRI International, Menlo Park, California 94025

Received October 2, 1997

We report high-power vacuum-ultraviolet (vuv) generation at the Lyman- $\alpha$  wavelength of 121.6 nm, using a simple experimental system. vuv radiation is produced through two-photon-resonant difference-frequency mixing with a tunable ArF excimer laser and a Nd:YAG-pumped dye laser. Using phase-matched mixtures of Kr and Ar at a total pressure of 650 mbar, we produced 7- $\mu$ J energies at Lyman- $\alpha$  in approximately 5 ns (1.3 kW), as measured directly with a pyroelectric energy probe. Measurements indicate that higher powers are possible with system optimization. A tuning range of 0.1 nm was achieved for a fixed gas mole fraction at a total pressure of 650 mbar. Qualitative agreement is found between measured tuning profiles and theoretical predictions. © 1998 Optical Society of America  
OCIS codes: 190.0190, 140.7240, 140.2180.

Development of coherent vacuum-ultraviolet (vuv) sources continues to provide new opportunities for vuv spectroscopy and photochemistry. Higher powers and broad tunability are extending techniques such as multiphoton detection, planar imaging, and photolysis deeper into the vuv. Hydrogen Lyman- $\alpha$  radiation (121.567 nm) is especially interesting because it permits single-photon detection of ground-state H atoms, which are important in arc-jet plumes, tokamaks, combustion, molecular dynamics, and astrophysics. Several researchers have generated Lyman- $\alpha$  with dye lasers and phase-matched mixtures of Kr with Xe or Ar by use of frequency tripling<sup>1-3</sup> or difference-frequency mixing.<sup>4</sup>

Alternatively, substantial vuv power can be generated with an ArF excimer laser and a dye laser by two-photon-resonant difference-frequency mixing,  $\nu_{\text{vuv}} = 2\nu_{\text{ArF}} - \nu_{\text{dye}}$ .<sup>5-7</sup> One can enhance this process by tuning the ArF laser to a two-photon resonance in H<sub>2</sub>, HD, or Kr, and tuning is provided by variation of the wavelength of the dye laser. By varying the dye-laser wavelength, one can produce vuv wavelengths of 110 to 180 nm. Because of the importance of the Lyman- $\alpha$  wavelength, our objective was to evaluate the energies available at Lyman- $\alpha$  with this technique. Kr has negative dispersion near Lyman- $\alpha$ , allowing phase matching by use of gas mixtures.

A schematic of the experimental arrangement is shown in Fig. 1. Because of the importance of beam quality for nonlinear frequency conversion, we modified the ArF laser (Lambda Physik EMG-150 MSC) to provide spatial filtering of the oscillator output beam and triple pass the amplifier.<sup>8</sup> This laser is tuned to two-photon resonances in the mixing gas. The third photon is provided by a Nd:YAG-pumped dye laser (Quanta-Ray DCR II and PDL) using Lambda Physik LC4700 dye. Output energies of the ArF laser and the dye laser are typically 20 and 10 mJ, respectively, and linewidths are of the order of 1 cm<sup>-1</sup>. The beams are combined on a high-power ArF dielectric mirror and focused with a 50-cm lens into the gas cell. We verify spatial overlap by temporarily directing portions of

the beams through a pinhole by use of a wedge. Temporal overlap is maintained by a drift-control circuit and verified by a fast photodiode. To minimize optics transmission losses, we use a single MgF<sub>2</sub> plano-convex lens (50-cm focal length at 250 nm) to provide an exit window for the mixing cell, collimate the vuv beam, and dispersively separate the vuv beam from the ArF and the dye beams. An aperture of 7-mm diameter spatially selects the vuv beam, which is detected by a Laser Precision RjP735 pyroelectric energy meter and a KBr photomultiplier tube. Two new vuv-grade MgF<sub>2</sub> lenses purchased from Optovac and Harshaw-Bicron were used for these measurements, and both initially yielded >70% transmission at Lyman- $\alpha$ . To date we have used only the Optovac lens and have not encountered the same degradation that was encountered in the research reported in Ref. 9, perhaps owing to improvements in MgF<sub>2</sub> growth techniques.

Although the pyroelectric energy probe allows relatively straightforward measurement of the vuv energies, it is not without complications. Irradiation of the probe with high-energy vuv radiation near Lyman- $\alpha$  causes the energy-probe output to decay within a period of minutes, becoming less sensitive to the ArF and the dye beams as well as to the vuv beam. The sensitivity recovers over periods of 10 min to several hours. The cause of this detector-sensitivity drop is

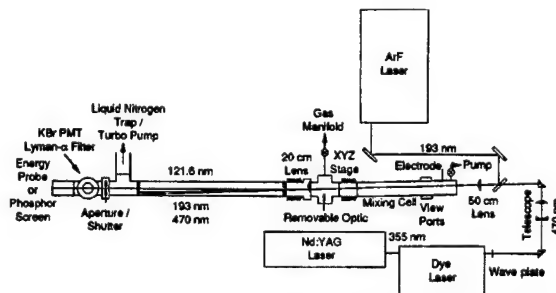


Fig. 1. Experimental apparatus for vuv generation. PMT, photomultiplier tube.

not currently understood. To provide a stable energy monitor, we also use a solar-blind KBr photomultiplier with a Lyman- $\alpha$  filter to measure vuv light scattered from the probe at right angles to the beam. This photomultiplier-filter combination is insensitive to ArF and dye light, and signal-to-background ratios of up to 100 are obtained. We estimate the accuracy of our energy measurements at 10% for direct probe readings and 30% with the photomultiplier and the filter.

Without phase matching, mixing in  $H_2$  produces 2 orders of magnitude more energy than mixing in Kr near Lyman- $\alpha$ . However,  $H_2$  does not produce vuv radiation well at Lyman- $\alpha$  because of production of H atoms, which absorb the vuv. In addition, resonant contributions to the refractive index from H atoms produce large variations in phase mismatch, causing large intensity fluctuations with varying vuv wavelength. Through manipulation of experimental parameters such as  $H_2$  pressure, laser powers, laser pulse synchronization, and ArF wavelength, we were not able to reduce H atom production sufficiently to allow good conversion at Lyman- $\alpha$ . For this reason we investigated the use of Kr.

One can enhance difference-frequency mixing in Kr by tuning the ArF laser to two-photon resonances with the  $6p[5/2, 2]$ ,  $6p[3/2, 2]$ , and  $6p[1/2, 0]$  states. Transitions to  $6p[5/2, 2]$  and  $6p[1/2, 0]$  lie in the wings of the ArF tuning curve, so we chose the  $6p[3/2, 2]$  transition. We purged the ArF beam path with argon to minimize losses owing to oxygen Schumann-Runge absorptions at this wavelength.<sup>8</sup> Generation of vuv radiation in pure Kr is poor because of the relatively large phase mismatch in Kr. The pressure dependence of the vuv intensity in pure Kr is shown in the lower part of Fig. 2. Peak energies of  $\sim 0.2 \mu J$  are produced at an optimum pressure of  $7 \pm 3$  mbar, roughly an order of magnitude lower than the optimum pressure in  $H_2$ . This is consistent with a calculated phase mismatch for Kr, which is five times larger than for  $H_2$  at Lyman- $\alpha$ . Phase mismatch can be eliminated by the addition of a positively dispersive gas such as Ar but not  $H_2$ , because H atoms are produced even when the ArF laser is tuned to the Kr resonance.

With phase-matched mixtures, higher partial pressures of Kr can be used. Figure 2 shows that a 3.9:1 Ar/Kr mixture with 260 mbar of Kr yields roughly 2 orders of magnitude of improvement over pure Kr. Phase-matched vuv generated at 130 mbar of Kr is shown in Fig. 3. We measured as much as  $7 \mu J$  of energy with 130 mbar of Kr. The excimer laser has a pulse length much longer than that of the dye laser, so we use the dye pulse length (5 ns FWHM) as an estimate of the vuv pulse length. At this pulse length we produced 1.3 kW of power at Lyman- $\alpha$ . As an indication of the brightness of our source, the Lyman- $\alpha$  radiation can be observed on a phosphor screen with the room lights on. The highest vuv power at Lyman- $\alpha$ , that was previously reported apparently corresponds to 250 W of power external to the mixing cell.<sup>4</sup> This previous power was measured indirectly through comparison of dye and vuv intensities measured by a spectrometer and a photomultiplier. This measurement approach is inaccurate owing to a variety

of systematic errors, such as comparing beam powers based on the fraction of the beams sampled by the spectrometer slit.

Our experiments indicate that significantly higher vuv powers are possible with further system optimization. Figure 2 shows that the vuv power is still increasing with pressure. Our cell was not designed for operation at overpressure, so higher total pressures were not explored. Further improvement is also possible by using larger focal-spot sizes (longer-focal-length lenses). We did not optimize the focal length of the focusing lens. Because the generated vuv depends on the path-integrated laser intensities, it varies with the incident laser powers, not with the peak intensities in the foci.<sup>10,11</sup> Thus larger focal-spot sizes can reduce saturation effects (which increase with the peak intensity) without sacrificing vuv power. Indications of saturation, which can occur as a result of dielectric breakdown, multiphoton ionization, ground-state depletion, intensity-dependent refractive-index changes, or other processes, are present in our measurements. Ideally, the vuv power scales with the square of the density, and our power rises more slowly (see Fig. 2). To gain full advantage of the longer conversion path lengths obtained with larger focal-spot sizes, one must

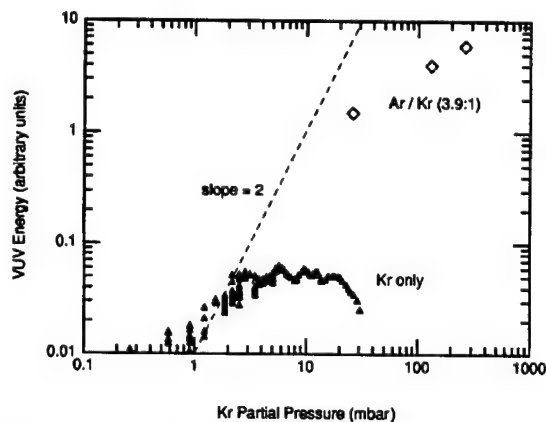


Fig. 2. Generated vuv as a function of Kr partial pressure. All measurements were performed at Lyman- $\alpha$ .

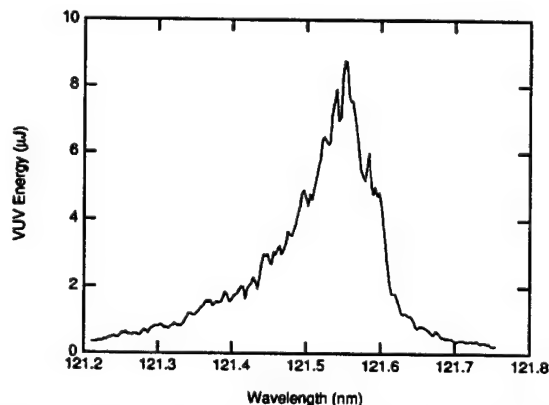


Fig. 3. Absolute vuv energy for a Kr partial pressure of 130 mbar.  $7 \mu J$  is generated at Lyman- $\alpha$ .

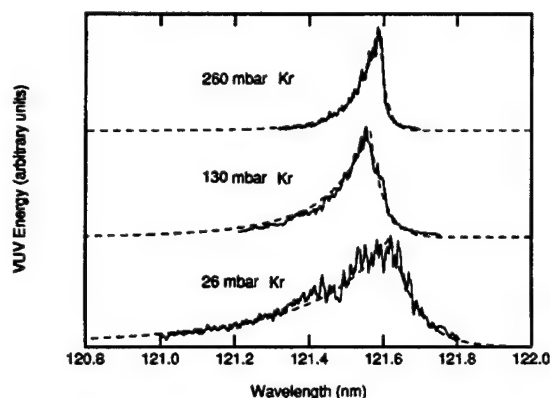


Fig. 4. Tuning range of vuv at different partial pressures of Kr. Solid curves, experimentally measured tuning profiles; dashed curves, fits using theoretical profiles.

ensure that the beam quality is quite good, which may require phase-conjugation amplification of the ArF laser.<sup>12</sup> Breakdown is often observed in the focal region at higher total pressures. Some reduction in breakdown or other saturation processes may be possible by use of a buffer gas with a higher refractive index than Ar, as the mixture used here is only 20% Kr. For operation at high pressures, absorption and (or) dispersion by rare-gas dimers may become important.<sup>1</sup> Because the tuning range at a fixed gas mixture is inversely proportional to the laser confocal parameters and the gas pressure, increased power may come at the cost of reduced tuning range. However, the tuning range may be increased by using a gas mixture that has a flatter dispersion than Ar/Kr.

The spectral tuning ranges for three Kr partial pressures are shown as solid curves in Fig. 4. As expected, the tuning range decreases (approximately) linearly with increasing pressure. These tuning profiles show a strong asymmetry, too strong to be caused by a curvature in the phase mismatch as a function of wavelength. Such asymmetry can be caused when ArF and the dye beams have dissimilar confocal parameters. This asymmetry is related to the additional phase change that occurs when the beams pass through the focus (Guoy effect). When the confocal parameters are not equal, a ripple is produced on the phase of the driving polarization that generates the vuv radiation. Depending on whether the phase of the driving polarization leads or lags the phase of the vuv wave (i.e., whether the phase mismatch is negative or positive), the phase ripple can be compensated for to a greater or lesser extent, leading to an asymmetry.

We fitted phase-matching curves to the profiles in Fig. 4 based on the expressions in Ref. 11.<sup>13</sup> These fits are shown as dashed curves in Fig. 4. The fitted confocal parameters for the ArF beam are 1.6 mm for 26 mbar of Kr and 6 mm for the two higher pressures. The fitted confocal parameters for the dye

laser are four times smaller than the ArF confocal parameter in each case. If we use the low-pressure confocal parameters to calculate focal-spot sizes, we find that the calculated and the measured spot sizes agree for the ArF beam, whereas the calculated spot size is roughly half the measured spot size for the dye laser. Our lasers do not have diffraction-limited Gaussian beams, so some disagreement in these values is not surprising. The fact that the fitted confocal parameters are not the same for all pressures may be related to refractive-index changes induced by the lasers or to other saturation effects. The dependence of the asymmetry on experimental confocal parameters means that the direction and the amount of asymmetry are experimentally dependent. The vuv beam profile also depends on the phase mismatch  $\Delta k$  and so will vary with wavelength.<sup>10</sup>

We have achieved directly measured energies of 7  $\mu$ J at Lyman- $\alpha$ , using two-photon-resonant difference-frequency mixing in phase-matched gas mixtures of Kr and Ar. Significant improvement in energy is expected with further system improvement, although this may come at the expense of a reduced tuning range for a fixed gas mixture.

The study was supported by the U.S. Air Force Office of Scientific Research under contract F49620-C-0027. We acknowledge helpful conversations with David L. Huestis of SRI International and the loan of the KBr photomultiplier tube by Richard J. Exberger of NASA-Ames Research Center.

## References

1. H. Langer, H. Puell, and H. Röhr, *Opt. Commun.* **34**, 137 (1980).
2. R. Mahon and Y. M. Yiu, *Opt. Lett.* **5**, 279 (1980).
3. R. Hilbig and R. Wallenstein, *IEEE J. Quantum Electron.* **17**, 1566 (1981).
4. J. P. Marangos, N. Shen, H. Ma, M. H. R. Hutchinson, and J. P. Connerade, *J. Opt. Soc. Am. B* **7**, 1254 (1990).
5. G. W. Faris and M. J. Dyer, in *Short-Wavelength Coherent Radiation: Generation and Applications*, P. H. Bucksbaum and N. M. Ceglio, eds. (Optical Society of America, Washington, D.C., 1991), pp. 56–61.
6. C. E. M. Strauss and D. J. Funk, *Opt. Lett.* **16**, 1192 (1991).
7. O. Kittelmann, J. Ringling, G. Korn, A. Nazarkin, and I. V. Hertel, *Opt. Lett.* **21**, 1159 (1996).
8. G. W. Faris and M. J. Dyer, *J. Opt. Soc. Am. B* **10**, 2273 (1993).
9. G. W. Faris and M. J. Dyer, *Opt. Lett.* **18**, 382 (1993).
10. G. C. Bjorklund, *IEEE J. Quantum Electron.* **QE-11**, 287 (1975).
11. G. Hilber, D. J. Brink, and R. Wallenstein, *Phys. Rev. A* **38**, 6231 (1988).
12. M. C. Gower, *Opt. Lett.* **8**, 70 (1983).
13. To achieve agreement with Ref. 13 and the figures of Ref. 11, we use only positive  $k$  values in Eq. (3) of Ref. 11. We do use a negative sign for the parameterized distance  $\epsilon$  for the difference (dye) wavelength.



## **APPENDIX E**

**ABSOLUTE CONCENTRATION, TEMPERATURE, AND VELOCITY  
MEASUREMENTS IN A DIAMOND DEPOSITING DC-ARCJET REACTOR,  
DIAMOND AND DIAMOND RELATED MAT., 7, 165 (1998).**

## Absolute concentration, temperature, and velocity measurements in a diamond depositing dc-arcjet reactor

Wolfgang Juchmann <sup>a</sup>, Jorge Luque <sup>b</sup>, Jürgen Wolfrum <sup>a</sup>, Jay B. Jeffries <sup>b,\*</sup>

<sup>a</sup> *Physikalisch Chemisches Institut, Universität Heidelberg, Heidelberg, Germany*

<sup>b</sup> *Molecular Physics Laboratory, SRI International, 333 Ravenswood Ave, Menlo Park, CA 94025, USA*

Received 23 June 1997; accepted 5 August 1997

### Abstract

Spatial distributions of the absolute concentration of H, CH, C<sub>2</sub>, and C<sub>3</sub> reactive intermediate species have been measured by laser-induced fluorescence (LIF) in the freestream plume of a dc-arcjet. Diamond film grows from this reactive mixture on a water-cooled molybdenum substrate in a 25 Torr reactor. The temperature of the gas jet is determined from LIF measurements of the rotational distribution of CH radicals in the plume. The directed velocity of the gas plume is derived from the Doppler shift of LIF. The fraction of the feedstock hydrogen dissociated is obtained from calorimetry. The atomic hydrogen concentration and gas temperature are used to constrain a model of the gas phase chemistry in the reactive plume. Concentration measurements of CH, C<sub>2</sub>, and C<sub>3</sub> provide a stringent test for the model of the diamond precursor chemistry. © 1998 Elsevier Science S.A.

**Keywords:** Plasma diagnostics; Chemical vapor deposition; Laser-induced fluorescence

### 1. Introduction

The chemistry precursor to diamond growth in conventional diamond reactors scales with the atomic hydrogen concentration [1–3]. The atomic hydrogen concentration in a dc-arcjet can approach [4] half of the hydrogen feedstock, which is consistent with the high quality diamond film and rapid growth rates observed in dc-arcjet reactors [5–8]. Chemical models [9–12] of the gas phase chemistry in the arcjet plume find the atomic hydrogen concentration important to predict the reactive gas flux to the growing diamond surface. Dandy and Coltrin [11] find the atomic hydrogen concentration so important to the predictions of their model, that they parameterize the results as a function of atomic hydrogen concentration. The atomic hydrogen concentration for the reactor condition studied here has been determined by a detailed power balance [4]. We use this measured atomic hydrogen concentration as an input parameter for the model of the precursor gas phase chemistry.

The reactive environment of the arcjet plume is investigated with laser-induced fluorescence (LIF) measure-

ments. The gas temperature is derived from the rotational temperature measured by LIF excitation scans [13,14]. This measured temperature constrains the model of the gas phase chemistry in the freestream of the arcjet plume. The directed velocity of the plume is determined from the Doppler shift of LIF between NO seeded into the plume flow and NO in a static cell [15]. The directed velocity establishes the reaction time of the reactive mixture of gases in the arcjet freestream. Both the gas temperature and the directed velocity are important terms in the calorimetry to determine the fraction of the feedstock hydrogen which is dissociated in the plume [4].

The dc-arcjet is an ideal reactor to test models of the chemical mechanism for the precursors for diamond growth; the rapid growth rate in such reactors suggests the important precursor species concentrations are large. In addition, the gas residence time in a dc-arcjet is well defined. Common diamond reactors such as hot filament and microwave discharge have rather small input feedstock flow with a long, diffusion controlled residence time. Small quantities of impurities or minor species in the feedstock can be important to the chemistry of systems with long residence times via complex and/or catalytic chemical reaction schemes.

The feedstock in the dc-arcjet reactor is activated in

\* Corresponding author. Fax: 001 650 859 6196;  
e-mail: jeffries@mplvax.sri.com

the discharge and expands through the nozzle into a reactive plume. The gas plume has a rapid directed velocity and the flight time to the boundary layer above the substrate is well defined. The transport through the thin boundary layer is diffusion controlled. In this paper, we will present a comparison of quantitative LIF measurements [16] of CH, C<sub>2</sub>, and C<sub>3</sub> concentrations in the freestream of the arcjet plume, with the predictions of reactive species mole fractions from a detailed chemical model constrained by measured gas temperature and atomic hydrogen concentration. This comparison indicates that the transport in the arcjet reactor is more complex than the simple picture presented above.

## 2. Experiment

The dc-arcjet reactor shown in Fig. 1 is the same used for previous work [4,13–16]. A 1.6 kW arc is struck in a 46:54 mixture of hydrogen and argon at a pressure of 6 atmospheres. The effluent from this arc expands through a converging/diverging nozzle into a reactor maintained at 25 Torr. Methane at 0.5% of the hydrogen flow is injected into the diverging section of the nozzle as shown in Fig. 1. For the velocity experiments 0.1% NO is added to the plume via the methane injector. Diamond thin film grows on a water-cooled molybdenum substrate inserted into the plume of the arcjet at a growth rate of approximately 1 mm/min. A probe laser beam shown in Fig. 1 is directed across the arcjet plume, the subsequent fluorescence is collected normal to the plume flow and the laser beam, and the optical probe volume of 1 mm<sup>3</sup> is determined by the intersection of the laser beam and the optical signal collection. The arcjet and substrate assembly can be moved with respect to optical probe volume during diamond deposition to

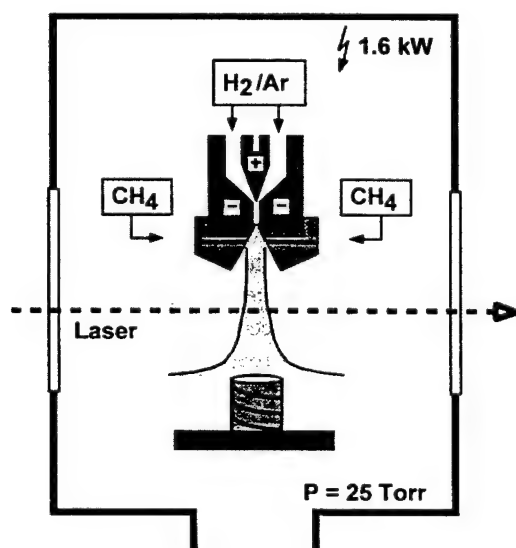


Fig. 1. Schematic of dc-arcjet in CVD reactor.

map spatial distributions along the centerline of the plume and radially across the cylindrically symmetric plume.

LIF signals from H, CH, C<sub>2</sub>, C<sub>3</sub>, and NO are excited with light from a variety of wavelength tunable laser sources, and the details of the excitation and optical collection for each of these species has been published in detail [14–17]. Atomic hydrogen is excited from the 1S ground state to the 3S and 3D excited states by two photons near 205 nm and the subsequent fluorescence to the 2P state near 656 nm is observed [17]. The 205 nm light is produced by frequency tripling a Nd:YAG pumped dye laser. CH radicals are excited in the 0–0 band of the B–X transition near 390 nm or the 0–0 band of the A–X transition near 437 nm with light from an excimer pumped dye laser, and the subsequent fluorescence is collected in the same band excited [14,16]. C<sub>2</sub> radicals are excited in the 2–0 band of the d–a Swan system and fluorescence collected in the 2–1 and 1–0 bands [16]. C<sub>3</sub> radicals are excited in the spectrally overlapped vibrational bands of the A–X transitions near 427 nm. The NO LIF is excited in the 0–0 band of the A–X transition near 226 nm with frequency doubled light from an excimer pumped dye laser [15].

## 3. Arcjet plume velocity

A trace of NO is seeded into the arcjet plume and LIF is excited by a laser beam directed into the plume flow through a small hole in the center of the substrate. The same laser beam also excites LIF from NO in a static cell. The directed velocity of the plume produces a Doppler shift in the NO excitation compared with that in the cell. The plume velocity determined from these Doppler shift measurements is shown in Fig. 2 as a function of radial distance about the centerline of the plume. The peak velocity of 2.6 km/s is supersonic at Mach 2.2 for the gas mixture of 0.26:0.27:0.47 of

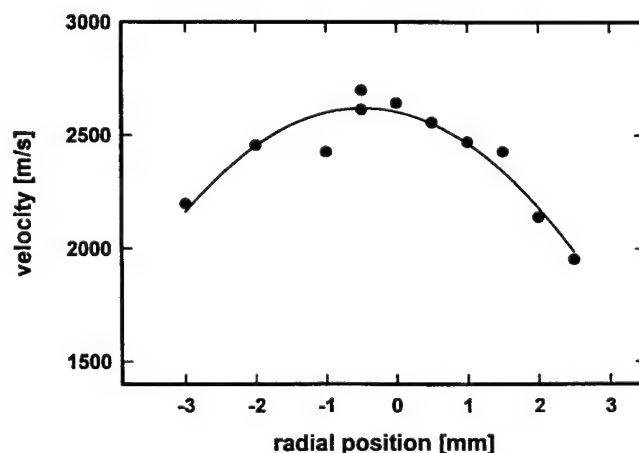


Fig. 2. Axial velocity vs radial position at the nozzle exit.

H:H<sub>2</sub>:Ar. This mixture results from the measured [4] 33% dissociation of the hydrogen feedstock with an initial mixture of 46:54 hydrogen and argon.

#### 4. Temperature

The gas temperature is determined from LIF measurements of the rotational distribution of CH [14,16]. Because the CH radicals chemically react rapidly with both H and H<sub>2</sub> in the arcjet plume, we tested the assumption that the CH rotational distribution is equilibrated with the gas temperature. We compared the CH measurements with an LIF measurement of the rotational distribution of NO seeded into the flow [16]. NO does not react with the major species in the arcjet plume (H, H<sub>2</sub>, and Ar), and thus, undergoes hundreds of collisions to insure the rotational distribution of NO is in thermal equilibrium with gas temperature in the freestream of the plume. We found agreement between the NO and CH data and conclude that the CH rotational distribution provides a good measure of the gas temperature [16].

Fig. 3 shows the gas temperature on the centerline of the arcjet plume between the nozzle exit at  $z=0$  and the substrate at  $z=38.2$  mm. The gas temperature is constant in the freestream and there is nearly a 1000 K temperature increase in the boundary layer above the substrate. This temperature rise is consistent with a shock heating from the impinging supersonic flow. In the shock, both temperature and pressure will rise abruptly.

#### 5. Concentration measurements

Quantitative concentration of H, CH, C<sub>2</sub>, and C<sub>3</sub> are determined in the reactive arcjet plume from LIF meas-

urements [14,16,17]. Quantitative LIF requires knowledge of the gas temperature, fluorescence quantum yield, spectroscopic data for the transition, and the detection efficiency for the optical collection. LIF results from optical excitation of a specific quantum state of an atom or molecule; therefore, gas temperature must be known to correct the signal for the Boltzmann fraction of the population in the specific state initially excited. The quantum yield is the probability that the excited state will radiate a signal photon, including all the non-radiative loss rates for the excited state. In the arcjet plume, LIF from H, CH, C<sub>2</sub>, and C<sub>3</sub> must compete with collisional quenching. For CH, C<sub>2</sub>, and C<sub>3</sub> the quantum yield is directly determined by comparison of the measured fluorescence decay time with the radiative lifetime [14,16]. From time-resolved LIF measurements, the quantum yield is obtained for different spatial positions in the plume. For atomic hydrogen, the quantum yield measured at very low reactor pressures compares well with collisional quenching rates determined from a model of the major species concentrations and literature values of the quenching rate constants. The model predictions are then extrapolated to higher reactor pressures, where direct measurements of the time-resolved fluorescence with nanosecond laser excitation are not possible [17].

Different strategies are used to determine the quantitative scale for each species [14,16,17]. For CH and C<sub>2</sub> there is a complete spectroscopic data base, a single quantum state can be excited within our laser and Doppler bandwidths, and the laser excitation and fluorescence rates are well known. The C<sub>3</sub> absorption spectrum is quasi-continuous at this temperature and spectral region. The probability for laser absorption is obtained from measurements of temperature-dependent optical absorption [18]. Two-photon absorption depends critically on the mode statistics of the laser; therefore, we chose to calibrate the quantum yield-corrected LIF measurements of relative concentration of atomic hydrogen with calorimetry [4,17]. The optical detection efficiency for CH, C<sub>2</sub>, and C<sub>3</sub> LIF is calibrated by Rayleigh scattering.

The variation of the absolute number density for H, CH, C<sub>2</sub>, and C<sub>3</sub> measured along the centerline in the freestream of the arcjet plume is presented in Fig. 4. Atomic hydrogen, CH, and C<sub>2</sub> radicals peak near the nozzle and decline in the freestream by approximately 30%. C<sub>3</sub> radical concentrations increase by approximately a factor of four between the nozzle and the boundary layer.

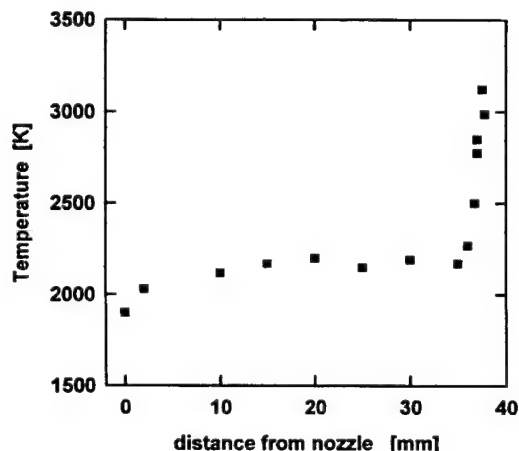


Fig. 3. Temperature along the centerline of the dc-arcjet measured by excitation LIF of CH B-X (0,0) rotational transitions.

#### 6. Chemical reaction model

The gas phase chemistry in the freestream is modeled as a one-dimensional (1D) flow with axial diffusion

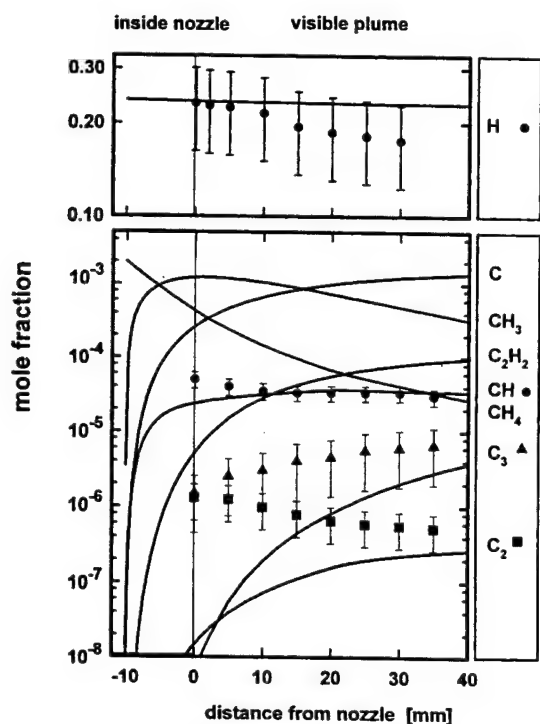


Fig. 4. Comparison between concentrations of gas-phase species in the arcjet determined by a 1D model (lines) and calibrated LIF (symbols).

using the Sandia premix and Chemkin codes [19]. We have constructed our own chemical mechanism (E.A. Brinkman and G.P. Smith, pers. comm.) consisting of C1 and C2 chemistry from the GRI-Mech [20] mechanism for methane combustion and estimates of the C3–C6 chemistry. The model calculation is constrained by the measured temperature, gas flow, gas velocity, and initial atomic hydrogen concentration. The solid lines in Fig. 4 are predictions of species concentrations in the freestream as a function of distance from the nozzle without a substrate present. The methane is injected inside the diverging nozzle at the position  $z = -8$  mm. LIF measurements are possible only after the plume exits the nozzle.

The deviation between calculated and measured atomic hydrogen is a direct measure of the radial diffusion, which is not included in this model. The measured CH radical concentration is in remarkable agreement with the model prediction. Near the nozzle, we find  $C_2$  and  $C_3$  present in concentrations more than two orders of magnitude larger than predicted by the model. This deviation near the nozzle is far larger than any estimated uncertainty, and strongly suggests that the gas re-circulation in the arcjet reactor (see Fig. 1) is an important contribution to the chemical composition of the arcjet plume. The radial distribution of the  $C_3$  forms a hollow cylinder about the center of the plume [16,21]. This radial distribution is another indicator that hydrocarbon radicals re-circulate from the shock structure in front of the substrate and are entrained in the

plume near the nozzle. Such a fluid flow provides a much longer residence time for the precursor chemistry.

## 7. Conclusions

LIF measurements of gas temperature and directed velocity are used to constrain a model of the gas phase chemistry of the freestream plume in a dc-arcjet reactor. The model predictions for H, CH,  $C_2$ , and  $C_3$  are compared with absolute radical concentrations measured with LIF. We find remarkable agreement between measured and predicted CH concentrations. The  $C_2$  and  $C_3$  concentrations near the nozzle indicate that re-circulation must be included in the transport model.

## Acknowledgement

We thank Mark Cappelli and Michael Loh of Stanford University for loan of the dc-arcjet. Gregory Smith and Elizabeth Brinkman provided the use of their chemical mechanism prior to publication. W. Juchmann is sponsored by Universität Heidelberg via Landesgraduiertenförderung. This work is supported by the Army Research Office and the Air Force Office of Scientific Research.

## References

- [1] D.G. Goodwin, *J. Appl. Phys.* 74 (1993) 6888–6895.
- [2] D. G. Goodwin, J. E. Butler, *Theory of Diamond Chemical Vapor Deposition*, in: *Handbook of Industrial Diamond and Diamond Films*, M. Prelas, G. Popovici, L. K. Bigelow (Eds), Marcel Dekker, New York, 1997, in press.
- [3] P. Bachmann, D. Leers, H. Lydtin, *Diamond Relat. Mater.* 1 (1991) 1.
- [4] W. Juchmann, J. Luque, J.B. Jeffries, *J. Appl. Phys.* 81 (1997) 8052–8056.
- [5] N. Ohtake, M. Yoshikawa, *J. Electrochem. Soc.* 137 (1990) 717.
- [6] R. Furukawa, H. Uyama, O. Matsumoto, *IEEE Trans. Plasma Sci.* 18 (1990) 930.
- [7] Z. P. Lu, L. Stachowicz, J. Heberlein, E. Pfender, in: A.J. Purdes, B.M. Meyerson, J.C. Angus, K.E. Spear, R.F. Davis, M. Yoder (Eds), *Diamond Materials*, The ElectroChemical Society Press, Pennington, NJ, 1991, Vols 91–98, pp. 99–105.
- [8] M.H. Loh, M.A. Cappelli, *Supersonic dc-Arcjet Plasma at Sub-Torr Pressures as a Medium for Diamond Film, Synthesis*, AIAA 92-3534, 1992.
- [9] G.P. Smith, J.B. Jeffries, *Gas phase chemistry in a diamond-depositing dc-arcjet*, in: A.J. Purdes, B.M. Meyerson, J.C. Angus, K.E. Spear, R.F. Davis, M. Yoder (Eds), *Diamond Materials*, The ElectroChemical Society Press, Pennington, NJ, 1991, Vols 91–98, pp. 194–201.
- [10] D.G. Goodwin, *Appl. Phys. Lett.* 59 (1991) 277.
- [11] M.E. Coltrin, D.S. Dandy, *J. Appl. Phys.* 74 (1993) 5803.
- [12] S.L. Girshick, C. Li, B.W. Yu, H. Han, *Plasma Chem. Plasma Proc.* 13 (1993) 169.

- [13] E.A. Brinkman, G.A. Raiche, M.S. Brown, J.B. Jeffries, *Appl. Phys. B* 64 (1997) 689–697.
- [14] J. Luque, W. Juchmann, J.B. Jeffries, *Appl. Opt.* 36 (1997) 3261.
- [15] W. Juchmann, J. Luque, J.B. Jeffries, manuscript in preparation.
- [16] J. Luque, W. Juchmann, J.B. Jeffries, *J. Appl. Phys.* 82 (1997) 2072–2081.
- [17] W. Juchmann, J. Luque, J.B. Jeffries, Two-photon laser-induced fluorescence of atomic hydrogen in a diamond depositing dc-arcjet. Western States Section of the Combustion Institute, Paper 97S-014, Livermore, CA, April, 1997.
- [18] D.M. Cooper, J.J. Jones, *J. Quant. Spectrosc. Radiat. Transfer* 22 (1979) 201.
- [19] R.J. Kee, J.F. Grcar, M.D. Smooke, J. Miller, Fortran program for modeling steady laminar one-dimensional flames. Sandia Report SAND85-8240, 1985.
- [20] C.T. Bowman, R.K. Hanson, W.C. Gardiner, Jr., V. Lissianski, M. Frenklach, M. Goldenberg, and G.P. Smith, GRI-Mech—an optimized detailed chemical reaction mechanism for methane combustion and NO formation and reburning. Refer to the GRI-Mech homepage at [http://www.me.berkeley.edu/gri\\_mech/](http://www.me.berkeley.edu/gri_mech/).
- [21] G.A. Raiche, J.B. Jeffries, *J. Appl. Phys. B* 64 (1997) 593.

## **APPENDIX F**

**EXCITED STATE DENSITY DISTRIBUTIONS OF H, C, C<sub>2</sub>, AND CH BY  
SPATIALLY RESOLVED OPTICAL EMISSION IN A DIAMOND DEPOSITING  
DC-ARCJET REACTOR, J. VACUUM SCI. AND TECH. A., 16 397 (1998).**

# Excited state density distributions of H, C, C<sub>2</sub>, and CH by spatially resolved optical emission in a diamond depositing dc-arcjet reactor

J. Luque, W. Juchmann,<sup>a)</sup> E. A. Brinkman,<sup>b)</sup> and J. B. Jeffries<sup>c)</sup>  
Molecular Physics Laboratory, SRI International, Menlo Park, California 94025

(Received 30 September 1997; accepted 12 December 1997)

Spatially resolved optical emission spectroscopy is used to investigate excited species in a dc-arcjet diamond depositing reactor. Temperature measurements indicate a cold plasma with electrons, excited states, and gas in nonthermal equilibrium. The H, C, C<sub>2</sub>, and CH excited state number densities decrease exponentially with the distance from the nozzle and have a pronounced increase in the shock structure above the substrate. The H emission increases throughout the boundary layer to the substrate surface, whereas emission from other species has a maximum in the boundary layer and then decreases again towards the substrate. The reconstructed radial distribution of excited state concentrations are Gaussian, with the C and C<sub>2</sub> distributions broader than the H and CH ones. The optical emission is calibrated with either Rayleigh scattering or laser-induced fluorescence to furnish absolute number densities. We find all the excited species to be present in concentrations two or more orders of magnitude smaller than the corresponding ground states measured in the same reactor and conditions. We find that C<sub>2</sub>(*d-a*) emission intensity correlates well with laser-induced fluorescence measurements of C<sub>2</sub>(*a*) concentration in the arcjet plume. Ground state concentrations of the other species do not vary as their emission intensity except near the substrate, where the variations of CH(*A-X*), CH(*B-X*), and C<sub>2</sub>(*d-a*) emission intensities are good monitors of the corresponding concentration changes. © 1998 American Vacuum Society.  
[S0734-2101(98)06102-8]

## I. INTRODUCTION

Low-pressure dc-arcjet reactors are attractive sources of chemically reactive gas flows for spray coating and chemical vapor deposition (CVD). Arcjet reactors have demonstrated diamond growth with rates approaching 1 mm/h,<sup>1</sup> at least ten times faster than in other reactors.<sup>2</sup> This rapid growth rate is a consequence of the large fraction of dissociation of the hydrogen feedstock gases in the reactive gas flow from the arcjet discharge.<sup>3</sup>

Gas mixtures containing argon, hydrogen, and methane are commonly used to produce diamond films in plasma reactors. The chemistry in most diamond CVD is dominated by charge neutral reactions of ground state radicals and atoms formed in the discharge, and there are models predicting C atoms and CH<sub>3</sub> radicals<sup>4,5</sup> as well as C<sub>2</sub> and C<sub>2</sub>H<sub>2</sub><sup>6,7</sup> as the dominate precursors to diamond growth. In order to characterize the reactive environment for diamond CVD, experiments to determine the ground state concentration of H,<sup>8-10</sup> C,<sup>11</sup> C<sub>2</sub>,<sup>12,13</sup> C<sub>3</sub>,<sup>13</sup> CH,<sup>13-17</sup> CH<sub>3</sub>,<sup>11,14,15,18-20</sup> and C<sub>2</sub>H<sub>2</sub><sup>20</sup> have been undertaken using nonintrusive optical diagnostics techniques in a wide variety of diamond producing reactors. Although this research has increased our understanding of diamond CVD,<sup>21</sup> the methodology is of limited use for real-time industrial process control, as such careful, quantitative, laser-based measurements require expensive, high maintenance equipment with highly trained technicians. Optical emission

spectroscopy (OES) is another nonintrusive method, with quite simple data collection and straightforward automation. Unfortunately optical emission arises only from atoms and molecules in electronically excited states, and interpretation of the optical emission signal requires an understanding of the link between excited and ground state concentrations. In spite of these limitations, OES is widely used for real-time monitoring in plasma processing.

The diamond film quality varies dramatically with deposition method and conditions and a large body of research has been undertaken to develop a simple relationship between OES from a species, the ground concentration of that species, and the quality of deposited diamond film. Klein-Douwle *et al.*<sup>22</sup> found a correlation between C<sub>2</sub> emission and the diamond film quality for material grown in a oxyacetylene flame. In a microwave plasma reactor, Lang *et al.*<sup>23</sup> found the diamond film quality to correspond to H atom actinometry<sup>24</sup> measurements. Gruen *et al.*<sup>25</sup> found OES signals from C<sub>2</sub> emission in a microwave plasma correlate with the growth rate, but not the emission from either H or CH. In a hot filament reactor, Cui *et al.*<sup>26</sup> observed emission from H and CH<sup>+</sup> relate to high quality diamond, and CH emission to indicate the presence of amorphous carbon films.

In CVD dc-arcjet reactors, the diamond film grows-on temperature controlled substrates from hydrogen arcjet plumes with a trace (<1%) of hydrocarbon. Although, optical emission from the reactive plumes of dc arcjets has been studied, all of the published work focuses on temperature determination from the rotational and vibrational distributions of the excited molecules. Raiche and Jeffries<sup>27</sup> report emission from CH(*A-X*), CH(*B-X*), CH(*C-X*), C<sub>3</sub>(*A-X*),

<sup>a)</sup>Permanent address: Physikalisch Chemisches Institut, Universität Heidelberg, Germany

<sup>b)</sup>Permanent address: IBM, San Jose, California

<sup>c)</sup>Electronic mail: Jeffries@mplvax.sri.com



and C<sub>2</sub>(*d-a*) in a dc arcjet (1 kW, 220 Torr), and do not find thermalization between excited and ground states of C<sub>2</sub>. Reeve and Weimer<sup>28</sup> observe CH(*A-X*) and C<sub>2</sub>(*d-a*) emission, and find quite different vibrational and rotational temperatures in CH(*A*) and C<sub>2</sub>(*d*). The OES study by Cubertaon *et al.*<sup>29</sup> reports a rotational temperature of CH(*B*) near 2700 K along the plume of their arcjet (3–5 kW, ~50 Torr) which is nearly three times less than their C<sub>2</sub> vibrational temperature of 7500 K. They also find quite different vibrational and rotational temperatures from the excited C<sub>2</sub>(*d*). Brinkman *et al.*<sup>30</sup> find nearly the same C<sub>2</sub>(*d*) rotational and vibrational temperatures as Cubertaon in their arcjet (1.6 kW, ~25 Torr). Analysis of the spatial distributions of the emission intensities led them to suggest that the excited C<sub>2</sub>(*d*) was formed by chemical reactions and CH(*A*) by electron impact.

In this work, we present spectroscopic observations from a dc-arcjet reactor during diamond CVD using the same operating conditions<sup>30</sup> where diamond film grows at 50 μm/h on a water cooled molybdenum substrate. The diamond film is well faceted with primarily (111) morphology, and the Raman spectrum of the film shows no trace of graphite content. We have characterized the arcjet plume in previous laser-based and probe measurements. Using quantitative laser-induced fluorescence (LIF), we determined the number densities and spatial distributions of CH, C<sub>2</sub>, C<sub>3</sub> radicals<sup>13,31,32</sup> and H atoms in the ground state.<sup>10</sup> The gas temperature<sup>13,30</sup> distribution was previously determined from LIF measurements of rotational distributions of ground state molecules. The flow velocity<sup>10</sup> was measured from the Doppler shift of LIF from NO seeded into the flow. Langmuir probe was used to determine the electron temperature and ion density.<sup>33</sup> We report here the quantitative, spatially resolved optical emission of H, C, C<sub>2</sub>, and CH. From these measurements, we determine excited state concentration, correlate the excited state concentration distribution with the respective ground state distribution and discuss the chemical roles and excitation mechanisms.

## II. EXPERIMENTAL METHOD

The CVD reactor, diamond deposition, and details about laser measurements have been described previously.<sup>10,13,30,33,34</sup> An arc (1.6 kW, 12 A, 140 V) is struck in a mixture of H<sub>2</sub>/Ar (0.9:1 at 6.9 slm total flow and six atmospheres pressure); the effluent from this arc expands through a converging/diverging nozzle into a low-pressure reactor (typically 25 Torr). Methane (~0.5% of the H<sub>2</sub> flow) is injected in the flow in the diverging section of the nozzle. The expanding gas forms a luminous plume approximately 1 cm in diameter which impinges on a water cooled molybdenum substrate 38.2 mm from the nozzle. Diamond grows at nearly 1 μm/min with a well faceted (111) morphology with a Raman spectrum free from graphitic features.<sup>10</sup>

The optical emission from the arcjet plume is collected with a lens *f*/6, spatially filtered with a 1 mm aperture, and focused with another lens identical to the first one into a monochromator selected to fit the requirements of the mea-

surement. For rotationally resolved scans, a Heath monochromator is used (*f*/7, 0.35 m focal length, 250 or 500 nm blaze gratings). Laser-based measurements require a detection bandpass with equal response for any rotational level in the selected vibrational band; here we construct a trapezoidal bandpass with 30 nm full width at half maximum (FWHM) from a Bausch–Lomb high intensity monochromator (*f*/6, 0.2 m focal length, 500 nm blaze grating) using a narrow front slit and a wide back slit. The signal is detected by a 1P28 photomultiplier, preamplified (×10), and averaged with a boxcar integrator (Stanford Research Systems SRS-250). During the calibration procedures of the emission signal, the voltage in the photomultiplier power supply and boxcar settings were kept identical to those used for the optical emission measurements. A SC Technology Plasma Chemistry Monitor 401, consisting of a spectrograph with a gated, intensified, photodiode array of 512 elements, is used as an optical multichannel analyzer to obtain emission spectra simultaneously in the range from 200 to 1000 nm with a 4 nm bandwidth. The relative spectral response of this instrument is calibrated using standard lamps (Optronics Laboratories), tungsten in the visible and deuterium in the ultraviolet. The two different lamps provide an overlapping region from 300 to 350 nm where we find good (<5%) agreement between the two independent calibration measurements.

The absolute intensity of the optical emission is calibrated by both Rayleigh scattering and laser-induced fluorescence of a known gas concentration and composition. A XeCl excimer laser (Lambda Physik EMG 103) pumping a dye laser (Lambda FL 2002) is the source of vertically polarized laser light to excite CH(*B-X*) or provide a Rayleigh scattering source. The 14 ns laser pulses have a spectral bandwidth of 0.20 ± 0.02 cm<sup>-1</sup> at 430 nm, measured with a monitor etalon. Some measurements around 315 nm, were made with a frequency doubled PDL-1 dye laser (bandwidth ~1 cm<sup>-1</sup>, pulse length ~7 ns), pumped by a Quanta Ray GCR-3 Nd:yttrium–aluminum–garnet (YAG) laser. A high precision energy meter (Rj-7200, Laser Precision Corp.) monitors the laser pulse energies from 10 nJ to 1 mJ.

## III. QUANTITATIVE OPTICAL EMISSION

The optical emission signal of a given electronic transition between an excited state *u* and the ground state *g* during a time interval *t<sub>g</sub>*, is equal to

$$S_{\text{OES}} = A_{\text{ug}} \cdot n_{\text{exc}} \cdot V_{\text{fl}} \cdot \frac{\Omega}{4\pi} \cdot \epsilon \cdot \eta \cdot t_{\text{g}}, \quad (1)$$

where *A<sub>ug</sub>* is the Einstein emission coefficient of the observed vibrational band (s<sup>-1</sup>), *n<sub>exc</sub>* is the steady state number density of excited species (cm<sup>-3</sup>), and *V<sub>fl</sub>* is the observed volume. The remaining factors are given by the optics and electronics in the detection of the fluorescence; where *Ω* is the solid angle, *ε* is the transmission efficiency of the optics, and *η* the photoelectric conversion. The emission from the total production of electronically excited species, *n<sub>nascent</sub>*, is reduced by collisional quenching and predissociation; the steady state concentration of excited species is

$n_{\text{exc}} = n_{\text{nascant}} \Phi$ , where  $\Phi = A/(A + Q + P)$  is the quantum yield,  $Q$  the quenching rate ( $\text{s}^{-1}$ ), and  $P$  the predissociation rate ( $\text{s}^{-1}$ ). We note the  $n_{\text{exc}}$  is the excited state number density which is measured in absorption.

One of the main problems related to OES absolute measurements is the limited spatial resolution of optical emission. When a single lens or a fiber optic are utilized to collect the emission from the reactor, the volume  $V_{\text{fl}}$  is defined by the lens  $f$  number or the fiber optic acceptance angle, and in both cases gives poor results. Using optical spatial filters, we obtain a line of sight measurement of the emission. However, only when the spatial distribution of emitters is homogeneous and the size of the plasma is known ( $d$ , in cm), the number density in the line of sight volume is

$$n_{\text{exc}} = \frac{1}{d} \int_0^{\infty} n_{\text{exc}}(x) dx = \frac{N_{\text{exc}}}{A_{\text{fl}} \cdot d}, \quad (2)$$

where  $N_{\text{exc}}$  is the number of emitters,  $V_{\text{fl}} = A_{\text{fl}} d$ ,  $A_{\text{fl}} = \pi r^2$  is the collection cross section given by the spatial filter,  $d$  is the plasma length. The plasma size and emitter distribution are usually unknown, and we can only obtain integrated column densities (emitters/cm<sup>2</sup>). This is the same problem that occurs for absorption measurements, and it is solved for geometry with cylindrical symmetry through Abel's inversion. The arcjet plume is cylindrically symmetric and the spatial distribution of the different species can be reconstructed from the set of measurements taken along the perpendicular axes to the line of sight. There are many proposed methods for the computation of Abel's inversion. In this work, we have followed the method proposed by Buie *et al.*,<sup>35</sup> which fits the data to a polynomial with even powers. The parameters are the input to an analytically derived form of the Abel inversion. We will find below that all the species have Gaussian radial distributions in the arcjet plume. The peak number densities are fit by Eq. (2) with the parameter  $d$  equal to the FWHM of the reconstructed Gaussian distribution.

The instrumental factors ( $\Omega, \epsilon, \eta$ ) in Eq. (1) can be determined by other optical measurements which include the same set of parameters. For example, Rayleigh scattering of a gas with the same optical collection given by<sup>36</sup>

$$S_{\text{Ray}} = n \cdot \frac{E_L}{h c \nu} \cdot \left( \frac{\partial \sigma}{\partial \Omega} \right) \Omega \cdot \epsilon \cdot \eta \cdot \frac{V}{A_L}, \quad (3)$$

where  $n$  is the number density of the gas,  $\nu$  is the frequency of the scattered photon ( $\text{cm}^{-1}$ ),  $(\partial \sigma / \partial \Omega)$  is the averaged cross section,  $E_L$  is the laser energy (J),  $V$  is the collection volume, and  $A_L$  is the laser cross section, set by apertures approximately equal to  $A_{\text{fl}}$ . From the plot of Rayleigh scattering signal versus the product of laser energy and pressure, we determine the experimental factor  $\Omega \epsilon \eta V / A_L$ .

The optical emission can also be calibrated by comparison to the signal from a known excited state number density. LIF can be used if the ground state number density of one of the plasma species is known as well. With low laser spectral irradiance to insure linear excitation and full time integration

of the fluorescence signal, the relationship between the detected LIF signal  $S_{\text{LIF}}$  and the molecular number density  $n_0$  is given by<sup>31,34</sup>

$$S_{\text{LIF}} = n_0 \cdot f_B \cdot \frac{B}{c} \cdot E_L \cdot \frac{\Gamma}{\Delta \nu} \cdot \frac{\tau_{\text{eff}}}{\tau_0} \cdot F_{\text{fl}} \cdot \frac{\Omega}{4 \pi} \cdot \epsilon \cdot \eta \cdot \frac{V}{A_L}. \quad (4)$$

$f_B$ , the Boltzmann factor, is the fraction of molecules in the probed quantum state and is calculated from the temperature determined by LIF excitation scans.  $B$  is the absorption coefficient for the rotational transition excited ( $\text{cm}^2 \text{J}^{-1} \text{s}^{-1}$ ),  $E_L$  is the laser energy (J),  $\Gamma$  is the lineshape overlap integral,  $\Delta \nu$  is the laser bandwidth ( $\text{cm}^{-1}$ ), the ratio  $\tau_{\text{eff}} / \tau_0$  is the fluorescence quantum yield with  $\tau_{\text{eff}}$  as the effective lifetime including collisional quenching, and  $\tau_0$  is the radiative lifetime.  $F_{\text{fl}}$  is the fraction of the fluorescence collected in the spectral bandwidth of the detector.

The LIF signal is produced only in the laser probed volume and can be related to the OES volume. Assuming the LIF measurement excites a rotational line in the same electronic transition observed in optical emission

$$\frac{S_{\text{LIF}}}{S_{\text{OES}}} = \frac{n_0}{n_{\text{exc}}} \cdot \frac{\tau_{\text{eff}}}{t_g} \cdot \frac{f_B \cdot E_L \cdot B \cdot \Gamma}{2 r \cdot d \cdot \Delta \nu \cdot c}. \quad (5)$$

The analogous expression for Rayleigh calibration

$$\frac{S_{\text{Ray}}}{S_{\text{OES}}} = \frac{n}{n_{\text{exc}}} \cdot \frac{4 \pi \cdot \tau_0}{t_g} \cdot \frac{E_L \cdot \left( \frac{\partial \sigma}{\partial \Omega} \right)}{2 r \cdot d \cdot h \cdot c \cdot \nu \cdot F_{\text{fl}}} \quad (6)$$

at a given laser energy  $E_L$ , and with integration time  $t_g$  long enough to integrate the whole laser-induced fluorescence signal or the Rayleigh signal, we can estimate the steady state number density of the corresponding excited state ( $n_{\text{exc}}$ ).

#### IV. RESULTS AND DISCUSSION

The wavelength resolved optical emission spectra from the arcjet plume varies dramatically as the feedstock gas is changed. When the feedstock is pure argon, we see strong emission features from the Ar and weak lines from Ar<sup>+</sup>. With a mixture of argon and hydrogen, we see a few of the strongest Ar lines, but the dominant emission is from the Balmer series of atomic hydrogen (Fig. 1); we are not able to detect the vacuum ultraviolet Lyman  $\alpha$  to compare its emission intensity. Adding just 0.5% methane to the flow again alters the emission from the plasma plume, we find significant atomic emission from H atoms in the Balmer series, C atoms, and very weak Ar I lines. There is strong emission from CH(A-X), CH(B-X), CH(C-X), and C<sub>2</sub>(d-a) bands. The remaining structure in the spectra is assigned to molecules as well. Emission from two other C<sub>2</sub> electronic systems is assigned: the C<sub>2</sub>(D-X) Mulliken bands at 232 nm and the C<sub>2</sub>(C-A) Deslandres-D'Azambuja bands near 360 nm.

The molecular emission becomes more dominant downstream from the expansion nozzle; Fig. 2 shows the spectrum at  $z = 20$  mm which is roughly halfway between the nozzle and the substrate. The optical emission spectrum also varies

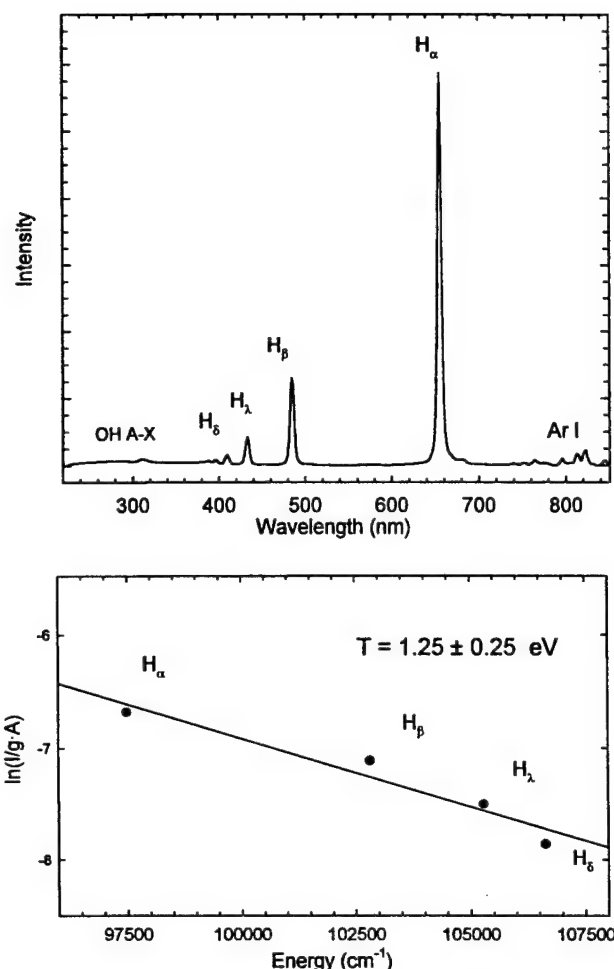


FIG. 1. Upper panel: Optical emission spectrum (4 nm FWHM), taken near the nozzle in a dc arcjet with 25 Torr reactor pressure, and 55% Ar and 45% H<sub>2</sub> feedstock at 1.6 kW. Lower panel: Electron temperature from atomic hydrogen Balmer series.

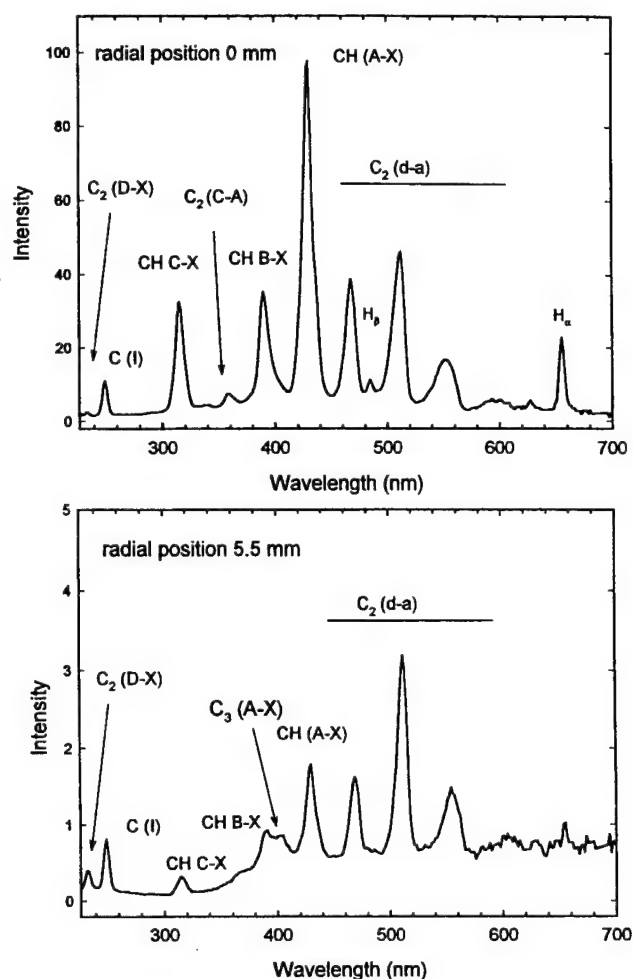


FIG. 2. Optical emission spectra (4 nm FWHM), taken 20 mm downstream from the arcjet nozzle with the standard conditions. Upper panel. Center of plasma plume. Lower panel. At a radius of 5.5 mm from the center.

with radial position in the plume; the upper panel shows the spectrum from the center of the plume which is dominated by CH emission with only a small underlying broadband visible background. Figure 2 lower panel is taken at a radius of 5.5 mm where the total emission intensity scale has been multiplied by 20. Here we see the dominant structured emission is from the C<sub>2</sub> Swan bands (*d-a*). In addition, the broadband visible background contains most of the emission intensity. The C<sub>3</sub> radical ground state has its maximum intensity at large radius in the cylindrically symmetric plume,<sup>32</sup> similarly at large radius near the edge of the plume, we identify C<sub>3</sub> emission as the 405 nm feature of the C<sub>3</sub>(A-X) (000)-(000) band, and we infer C<sub>3</sub> as the source of the less structured background emission between 330 and 500 nm. In addition to C<sub>3</sub> emission, the visible background likely includes contributions from other hydrocarbon fragment like C<sub>2</sub>H<sup>37</sup> or carbon clusters C<sub>4</sub> and C<sub>5</sub> by analogy to observations in neon matrices.<sup>38</sup> This speculation is further reinforced by *ab initio* calculations;<sup>38,39</sup> of both radicals which find electronic bands in the visible region, near 500 nm. However, C<sub>4</sub> and C<sub>5</sub> have not been spectroscopically identi-

fied in gas phase yet. In addition, we observe light from OH(A-X) and NH(A-X) at 308 and 336 nm, respectively; these molecules are present in the plume either from impurities in the feedstock gases or minor leaks in the vacuum system. The only ion observed is emission assigned to CH<sup>+</sup>(A-X) as it can be seen in Fig. 3. Details of the most important species and transitions identified can be found in the Table I.

### A. Temperatures

The energy distribution in the plasma is an important characterization parameter. We determine excited state temperatures from the rotational (or vibrational) distribution of molecular optical emission, the ground state (gas) temperature from LIF measurements of the ground state rotational distribution, and electron temperature from the atomic hydrogen excited state distribution. Atomic hydrogen emission lines are a good measure of the electron temperature when electron impact is the excitation mechanism and the excitation energies are all in the tail of the electron energy distribution. Assuming the various atomic hydrogen excited states

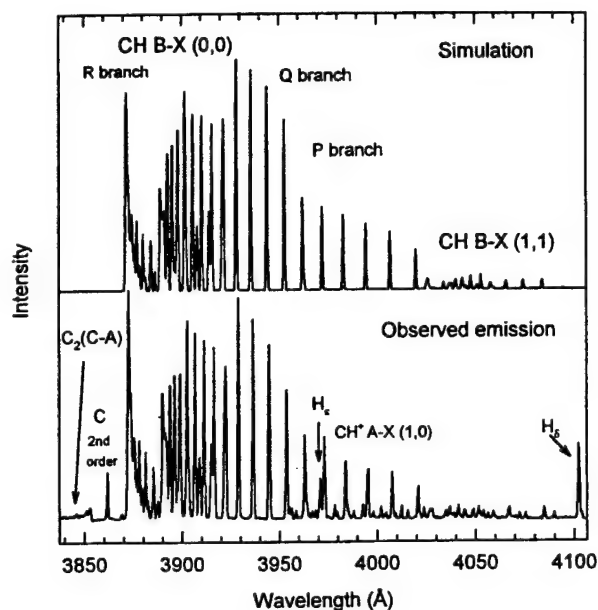


FIG. 3. Optical emission spectrum from the plasma plume on the centerline with  $z = 20$  mm (0.1 mm FWHM) showing emission from CH(B), CH<sup>+</sup>(A), C<sub>2</sub>(C), and atomic C and H in the lower panel. Upper panel shows simulation of CH(B) with a rotational temperature of 2500 K, and vibrational of 2100 K.

have similar excitation cross sections and collisional quenching rates, the atomic hydrogen emission intensity from each level is proportional to the number density of electrons at that energy. The lower panel in Fig. 1 shows the Boltzmann plot of the atomic hydrogen Balmer series. The relationship between the line intensities  $I_i$  and temperature  $T$  is

$$\ln\left(\frac{I_i}{g_i A_{ij}}\right) = -\frac{E_i}{kT} + C, \quad (7)$$

where  $g_i$  is the degeneracy of the state  $i$ ,  $A_{ij}$  the emission coefficient, and  $E_i$  the energy.<sup>40</sup> When we calculate an emission temperature for the H <sub>$\alpha$</sub> , H <sub>$\beta$</sub> , H <sub>$\gamma$</sub> , and H <sub>$\delta$</sub>  with a feed-

stock mixture of only Ar and H we obtain a temperature of  $1.25 \pm 0.25$  eV near the nozzle (Fig. 1, bottom), in good agreement with earlier Langmuir probe measurements of electron temperature.<sup>33</sup> Although some slight systematic deviations from a linear Boltzmann plot are observed in Fig. 1, these are minor and can be attributed to either quenching effects or nonequilibrium features of the plasma.<sup>41</sup> The addition of methane lowers the temperature to  $\sim 1$  eV ( $\sim 11$  600 K).

We examine the rotational distribution in the excited CH(B) and CH(C) and compare the results to our previous results<sup>30</sup> for excited CH(A) and C<sub>2</sub>(d). The emission is analyzed by spectral simulation with LIFBASE,<sup>42</sup> including both predissociation and collisional quenching. These corrections are important to determine the nascent population distributions, especially in the case of the CH(C). From time resolved LIF, we measure the quenching of the CH(B)<sup>31</sup> to be  $1 \mu\text{s}^{-1} \text{Torr}^{-1}$ , and found no rotational dependence of this collisional quenching rate. There is no data for the CH(C) state, but there is evidence of its quenching with H<sub>2</sub> that is faster than the quenching of the CH A and B states,<sup>43,44</sup> and we estimate a quenching rate of  $\sim 2 \mu\text{s}^{-1} \text{Torr}^{-1}$ . Predissociation is strong in CH(B,  $v' = 0$ ,  $N' > 15$ ), CH(B  $v' = 1$ ,  $N' > 6$ ),<sup>45</sup> and for all levels of CH(C),<sup>46,47</sup> varying with rotational and vibrational quantum numbers.

Emission from CH(B) is prominent in the wavelength dispersed optical emission in the region 384–410 nm shown in the lower panel of Fig. 3. This emission is collected 20 mm downstream of the nozzle from the center of the plume. The upper panel is a simulation of the CH(B) (0,0) and (1,1) bands with a rotational temperature of 2500 K. We find the excited CH(B,  $v' = 0$ ) state is well fit by rotational temperatures between 2300 and 2700 K. These temperatures are substantially lower to the ones measured<sup>30</sup> in CH(A) and C<sub>2</sub>(d), and in good agreement with measurements of CH(B) of Cubertaon *et al.*<sup>29</sup> in a similar reactor. In addition, the rotational distributions of CH(B) produced by electron impact on CH<sub>4</sub> and C<sub>2</sub>H<sub>2</sub> near the appearance potential ( $\sim 14$  eV)

TABLE I. Summary of the identified species, electronic transitions, and their dominant band or line positions. Also, a comparison of the ground and excited states number densities in the middle of the arcjet plume at 20 mm from the nozzle.

Species	Transition	Line positions (nm)	Emission coefficient (s <sup>-1</sup> )	Excited state number density (cm <sup>-3</sup> )	Ground state number density (cm <sup>-3</sup> )
H	3n-2n	656	4.4 × 10 <sup>7</sup> (Ref. 40)	10 <sup>7</sup>	3 × 10 <sup>16</sup> (Ref. 10)
	4n-2n	486	8.4 × 10 <sup>6</sup>	10 <sup>7</sup>	
C	<sup>1</sup> P <sup>0</sup> - <sup>1</sup> D	193	2.4 × 10 <sup>8</sup> (Ref. 40)	5 × 10 <sup>6</sup>	not measured
	<sup>1</sup> P <sup>0</sup> - <sup>1</sup> S	247	3.4 × 10 <sup>7</sup>		
CH	A-X( <sup>2</sup> Δ- <sup>2</sup> Π) Δv=0	431	1.8 × 10 <sup>6</sup> (Ref. 47)	1.2 × 10 <sup>9</sup>	
	B-X( <sup>2</sup> Σ <sup>-</sup> - <sup>2</sup> Π) Δv=-1,0	387	3 × 10 <sup>6</sup> (Ref. 47)	3 × 10 <sup>8</sup>	3.5 × 10 <sup>12</sup> (Ref. 13)
	C-X( <sup>2</sup> Σ <sup>+</sup> - <sup>2</sup> Π) Δv=0	314	1 × 10 <sup>7</sup> (Ref. 64)	6 × 10 <sup>7</sup>	
CH <sup>+</sup>	A-X( <sup>1</sup> Π- <sup>1</sup> Σ <sup>+</sup> ) Δv=1,0	396, 423	2.5 × 10 <sup>6</sup> (Ref. 65)	~3 × 10 <sup>7</sup>	not measured
C <sub>2</sub>	d-a( <sup>3</sup> Π <sub>g</sub> - <sup>3</sup> Π <sub>u</sub> ) Δv=1,0,-1	465, 480, 515	1 × 10 <sup>7</sup> (Ref. 13)	2 × 10 <sup>8</sup>	3 × 10 <sup>10</sup> (Ref. 13)
	D-X( <sup>1</sup> Σ <sub>g</sub> <sup>+</sup> - <sup>1</sup> Σ <sub>g</sub> <sup>+</sup> ) Δv=0	231	5.5 × 10 <sup>7</sup> (Ref. 66)	~5 × 10 <sup>5</sup>	
	C-A( <sup>1</sup> Π <sub>g</sub> - <sup>1</sup> Π <sub>u</sub> ) Δv=1,0,-1	360, 385, 410	3.2 × 10 <sup>7</sup> (Ref. 66)	~2 × 10 <sup>6</sup>	
C <sub>3</sub>	A-X( <sup>1</sup> Π <sub>u</sub> - <sup>1</sup> Σ <sub>g</sub> <sup>+</sup> )	405	5 × 10 <sup>6</sup> (Ref. 13)	<10 <sup>8</sup>	~3 × 10 <sup>12</sup> (Ref. 13)

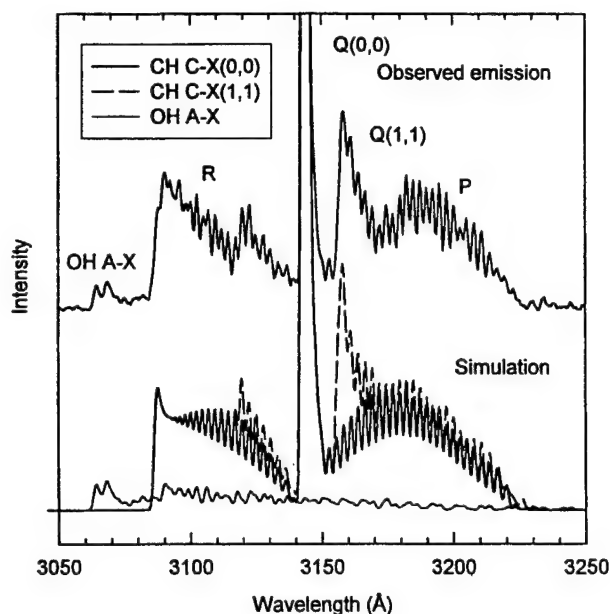


FIG. 4. Optical emission from the plasma plume on the centerline with  $z = 20$  mm (0.2 nm FWHM), comparing emission from CH(C) in the upper trace with a simulation at 5500 K in the lower trace. Note the experimental spectrum also shows emission from OH (A-X) near 308 nm, and its simulation is set to  $T = 4000$  K.

have been reported in the literature, with temperatures in  $v' = 0$  of  $\sim 2600$  and  $\sim 2300$  K, respectively,<sup>48,49</sup> reinforcing the hypothesis that CH(A) and CH(B) are products of electron impact dissociation.

Figure 4 compares the wavelength resolved emission for CH(C) with our simulation using a rotational and vibrational temperature of 5500 K. All of the CH electronic states have different rotational temperatures, 5500 K for CH(C), 2500 K for CH(B), and 3500 K for CH(A). Figure 5 shows the LIF excitation spectrum of CH(C-X) taken in the same position in the plume which compares well with the simulation at a temperature of 2200 K in good agreement with previous ground state LIF measurements<sup>13,30,31</sup> with the same reactor conditions. These earlier experiments found the LIF rotational distribution of ground state CH to be a good measure of the gas temperature. Thus, we find the dc-arcjet plume is a nonequilibrium plasma with different thermal distributions for the electrons, molecular excited states, and the bulk gas.

## B. Excited state number densities

The number densities are proportional to the ratio between band areas and emission coefficients in spectrally corrected scans like the ones in Fig. 2. The optical detection is calibrated to determine quantitative excited state number densities from the optical emission. We use Rayleigh scattering to calibrate the optical emission signal collection. The scattering was produced with a laser wavelength of 388 nm, in the same spectral region where the CH(B-X) emission occurs. The calibration of the emission signal is performed 20 mm downstream from the nozzle, with the plasma jet off

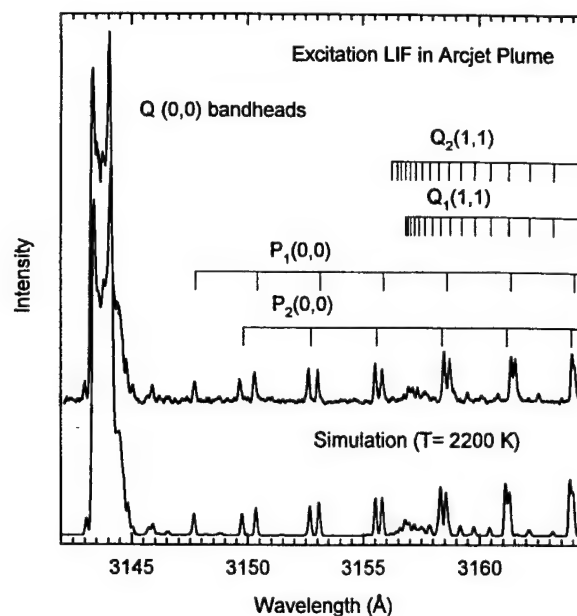


FIG. 5. Laser-induced fluorescence spectrum exciting CH(C)-CH(X) in the plasma plume on the centerline with  $z = 20$  mm in the lower trace (0.012 nm FWHM). The lower trace is a simulation spectrum at 2200 K.

and the chamber filled with argon to a pressure between 10 and 100 Torr. The number density of CH X is known from earlier measurements,<sup>31</sup> and LIF on  $R_1(10)$  CH(B-X) (0,0) was used as a secondary calibration standard. We found both methods in agreement within 15%, but the LIF calibration is less reliable because it is an indirect measurement, which requires calibration as well. For the excited state number density measurements reported here, the errors are dominated by the mismatch of the calibrated detection volume and the actual emission volume, and we expect overall 25%–50% uncertainty.

Once the ratio between optical emission and calibration signal is obtained, the number density of CH(B) is corrected by the radial profile to account for line of sight integration of the emission signal. Table I shows the number densities of excited state species after normalizing to the CH B value, the emission coefficients, and ground state number densities whenever they are available. The excited state number densities estimated are in the  $10^5$ – $10^9$  mol/cm<sup>3</sup> range, and are all several orders of magnitude less than the respective ground state number density. Those values are reasonable in a system where the chemistry is dominated by ground state species.

The highest ratio of excited to ground state concentration is found for  $C_2(d)/C_2(a) \sim 0.01$ . Even higher ratios, with population inversion between  $C_2(d)$  and  $C_2(a)$  have been measured by absorption spectroscopy in an arc plasma during the deposition of amorphous hydrogenated carbon coatings.<sup>67</sup> Excited  $C_2(d)$  appears readily in these systems, but it is not accompanied by a large amount of  $C_2$  ground state; for example, Gruen *et al.*,<sup>25</sup> observe bright emission during hydrogen free diamond growth in a microwave



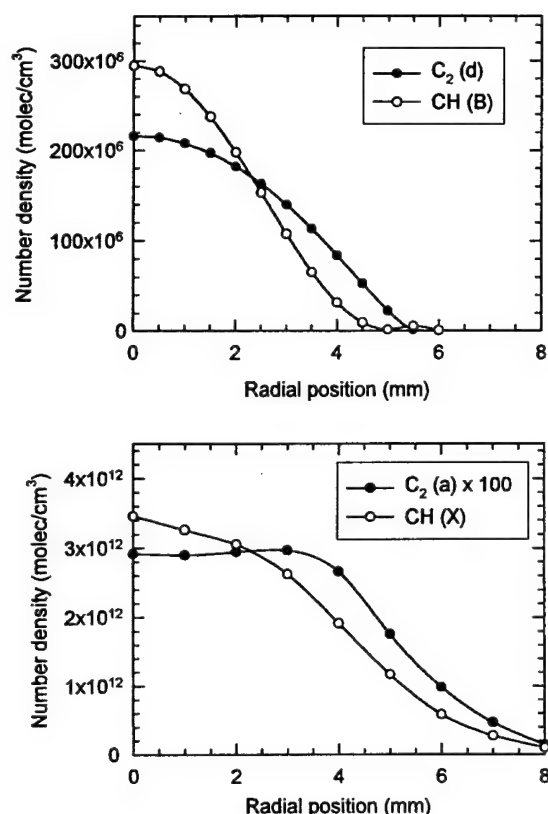


FIG. 6. Upper panel: Radial distribution of excited state number density at  $z = 20$  mm in the freestream of the plasma plume. Note the  $C_2(d)$  structure is wider than that for  $CH(B)$ . Lower panel: Radial distribution from Ref. 13 of ground states from LIF measurements in the same arcjet conditions.

plasma reactor and they infer  $C_2$  is an important reactant for diamond growth. In the dc arcjet, a strong chemiluminescence does not correlate with a large amount of  $C_2$ , and the total number density of this radical is too small to support the observed diamond growth rate.

### 1. Spatial distributions

Radial distributions of the excited state concentrations of H, C,  $CH(A)$ ,  $CH(B)$ ,  $CH(C)$ ,  $C_2(d)$ , and  $C_2(D)$  states have been obtained by the Abel transform, and measurements of  $CH(A)$  and  $C_2(d)$  at  $z = 20$  mm from the nozzle are shown in the upper panel of Fig. 6. We find the recovered distributions to have a Gaussian-like shape, and the  $C_2$  distribution is wider than for  $CH(A)$  (7 mm vs 5 mm FWHM), which is consistent with observed differences between their respective ground states. Nonetheless, the excited states are observed in a region of the plume significantly narrower than for the ground states,<sup>13</sup> where we find the radial distributions with a FWHM greater than 10 mm (Fig. 6, lower panel). We find two distinct radial distributions with excited H,  $CH(A)$ ,  $CH(B)$ , and  $CH(C)$  have narrow distributions, and C,  $C_2(d)$ , and  $C_2(D)$  have wide distributions.

Figure 7 is a contour map of the cylindrically symmetric excited state distribution for  $CH(B)$ ; the top and center of the figure is the nozzle exit and the substrate is at 38.2 mm.

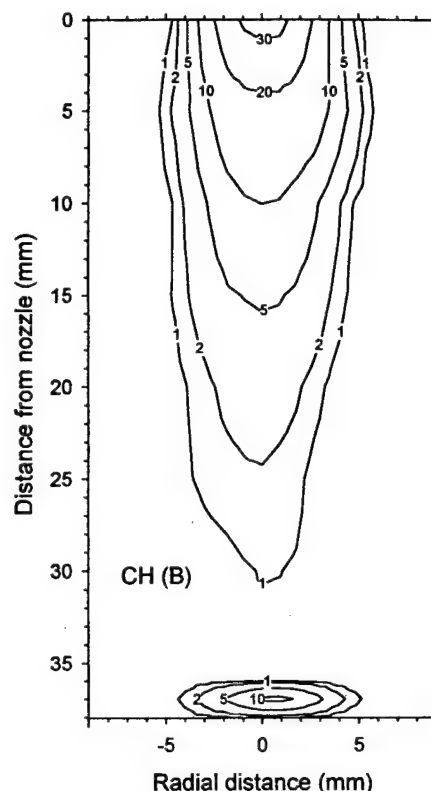


FIG. 7. Contour plot of the spatially resolved concentrations of  $CH(B)$  between the nozzle and the substrate; note the increased emission in the boundary layer above the substrate. Number densities are in units of  $10^8$  molecules/cm<sup>3</sup>.

Along the centerline in the plume, we see the number density decreases noticeably, before rising again just above the substrate. However, the radial distribution does not change between the nozzle exit and the shock structure just above the substrate. Figure 8 shows the distribution of excited  $C_2(d)$ , where the vertical gradient is not so large, and again the radial distribution does not change between the nozzle and the substrate. Emissions from H, C,  $CH(A)$ , and  $CH(C)$  also have maxima on the centerline of the plume. However, the emission from  $C_3$  and larger hydrocarbons does not peak on the centerline as seen in the radial variation of the broadband visible background in Fig. 2.

There is a large variation of the optical emission intensity as a function of distance from the nozzle. The upper panel of Fig. 9 plots the excited state number density along the centerline of the plume versus distance from the nozzle for atomic carbon ( $^1P$ ),  $CH(A)$ , atomic hydrogen ( $n=3$ ),  $C_2(D)$ , and  $C_2(d)$ ;  $CH(B)$ , and  $CH(C)$  are omitted because they have a similar behavior to  $CH(A)$ . The lower panel of Fig. 9 contrasts the excited state concentrations on the centerline of the arcjet plume with the ground state concentrations measured earlier by laser-induced fluorescence.<sup>13,52</sup> Note the excited state number densities are several orders of magnitude smaller than the respective ground states. Both atomic hydrogen and CH radical ground state concentrations are nearly constant with distance from the nozzle while their

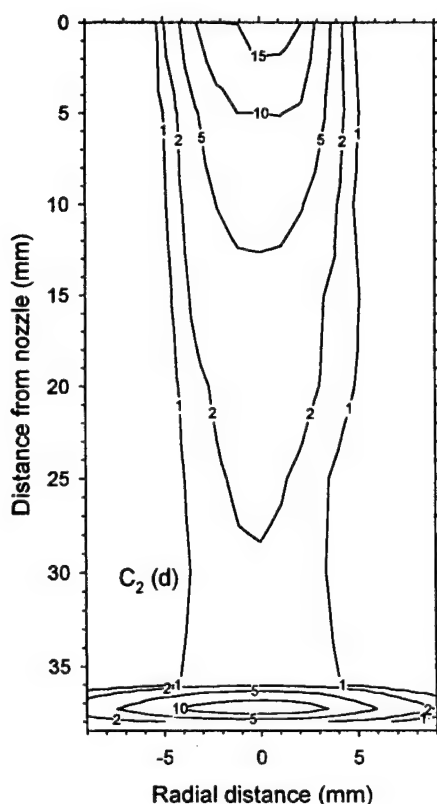


FIG. 8. Contour plot of the spatially resolved concentrations for C<sub>2</sub>(d). Number densities are in units of 10<sup>8</sup> molecules/cm<sup>3</sup>.

excited state concentrations decline rapidly. Whereas the C<sub>2</sub>(d) and C<sub>2</sub>(a) state concentrations have quite similar variation with distance from the nozzle.

The excited state number density for all of the species decreases with distance from the nozzle until the shock heated boundary layer just above the substrate surface. The plume velocity is greater than the sound speed, therefore a shock is created when this supersonic plume impinges on the substrate. The shock, called a normal shock because the flow velocity is normal to the substrate, creates a pressure and temperature rise in the boundary layer. The excited state number density for all the species except atomic hydrogen rises and shows a peak between the shock and the substrate. Excited atomic hydrogen also rises in the shock heated boundary layer; however, instead of peaking in the boundary layer and decreasing near the surface, the excited H atoms continue to increase with a maximum at the surface.

In the freestream, the region of the plume flow before the shock, the excited state number density exponentially decreases, as evident from the linear semilogarithmic plots in Fig. 9; all of the excited state concentrations decrease by more than a factor of 100 except the factor of 8 for the decrease of C<sub>2</sub>(d). The variation in excited state number density is much more dramatic than the decline of less than a factor of 2 observed for the ground state CH<sup>31</sup> and atomic hydrogen.<sup>52</sup> The data in Fig. 9 show that each of the different excited species has a different exponential decay with dis-

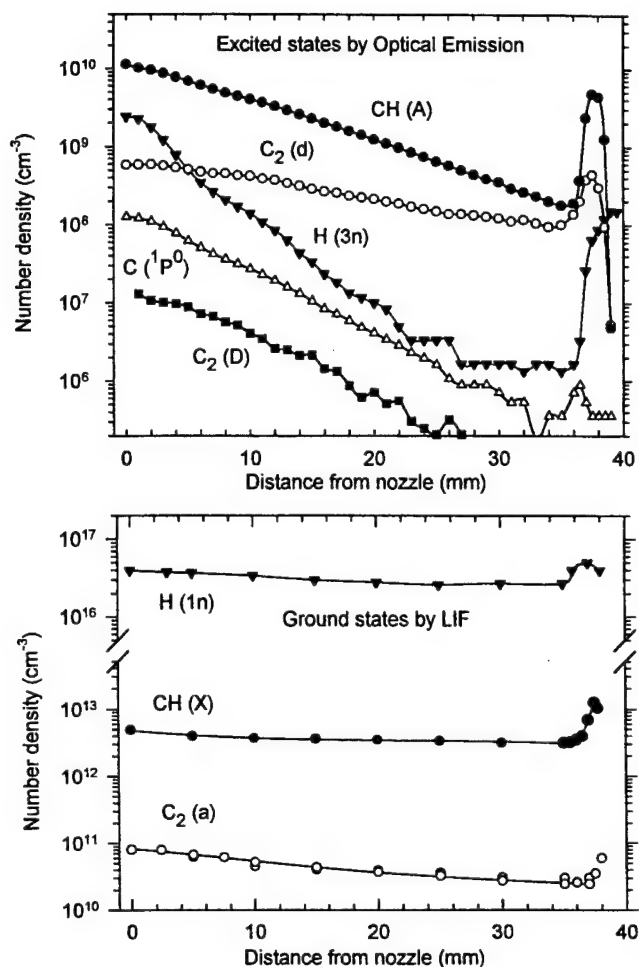


FIG. 9. Centerline number density of CH(A), C<sub>2</sub>(d), C<sub>2</sub>(D), C, and 3n hydrogen atoms as a function of distance from the nozzle with a substrate at 38.2 mm in the upper panel contrasted with LIF measurements of CH(X), C<sub>2</sub>(a), and ground state hydrogen atoms from Refs. 13 and 52 in the lower panel.

tance, or in the semilogarithmic plots a different slope  $\beta$ :

$$n_{\text{exc}}(d) = n_{\text{exc}}(0) \cdot e^{-\beta \cdot d}. \quad (8)$$

We can use the rapid decrease in optical emission with distance from the nozzle and the variation of the  $\beta$  to unravel excitation mechanism of the optical emission.

The radiating species are excited in the plume and emit their optical emission without moving very far from position of excitation. The distance from the nozzle in Fig. 9 is related to time via the plume velocity. For the conditions reported here, we have measured<sup>10</sup> the plume velocity to be  $\sim 2.5$  km/s; therefore, the transit time between the exit of the nozzle and the boundary layer above the substrate is  $\sim 15$   $\mu$ s. This time is very long compared to the excited state lifetimes; we measured collisionally shortened effective lifetimes of CH(A,B) and C<sub>2</sub>(d) to be 30–45 ns. Therefore, even at the supersonic plume velocity, the excited species are produced and deactivated within a distance of only 0.1 mm. There are four excitation mechanisms which might produce excited atoms and molecules in the arcjet plume: radiative transfer from the discharge inside the nozzle, thermal exci-

tation, electron impact, and chemiluminescent reactions. We can quickly eliminate radiative transfer and thermal excitation as important sources of optical emission from the arcjet plume.

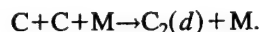
Radiative transfer from optical emission in the discharge region inside the nozzle can produce an exponential decay of excited state population with distance from the nozzle only if the lower-state densities in the optical transition are large enough for the plume to be optically thick. Previous quantitative LIF measurements<sup>13</sup> show that CH(X) and C<sub>2</sub>(a) have number densities of 10<sup>12</sup> and 10<sup>10</sup> cm<sup>-3</sup>, respectively. Thus, the CH and C<sub>2</sub> transitions can not be optically thick. Ground state atomic hydrogen has a density of greater than 10<sup>16</sup> cm<sup>-3</sup> and the plume is optically thick for Lyman transitions which terminate on the ground state. However, we find the number density of H(*n*=3) to be in the range of 10<sup>6</sup>–10<sup>9</sup> cm<sup>-3</sup> and Balmer transitions are optically thin in the arcjet plume. Atomic carbon is similarly optically thin. Therefore, the H, C, CH, and C<sub>2</sub> excitation mechanisms in the arcjet plume are not radiative transfer from the discharge inside the nozzle.

Thermal excitation is not important in the plume either. The temperature is nearly constant between the nozzle and the boundary layer;<sup>30,31</sup> therefore, thermal excitation would not produce the exponential decline in excited state population with distance from the nozzle. In addition, thermal equilibrium calculations with temperature of 2200 K predict a ratio of 10<sup>-7</sup>–10<sup>-5</sup> for CH (A or B) or C<sub>2</sub>(d) and the respective ground states, much smaller than the ratio of 10<sup>-2</sup>–10<sup>-3</sup> observed.

Chemiluminescent chemical reactions are an important excitation mechanism in many reacting flows; for example, chemiluminescent reactions are the primary production pathway for the formation of excited CH(A), CH(B), and C<sub>2</sub>(d) in flames. However, the number density and the spatial distribution of most of the excited species in the arcjet plume are inconsistent with a chemiluminescent reaction mechanism.

Most of the combustion reactions which produce emission from CH require oxygen containing reactants.<sup>50</sup> In the arcjet plume, oxygen is only present as an impurity; thus, these chemiluminescent reactions are unlikely to produce the bright emission from CH(A), CH(B), and CH(C) observed from the arcjet plume. The possible chemiluminescent reaction excitation mechanisms are also constrained by the large decrease in optical emission intensity with distance from the nozzle. Fast chemical reaction rate coefficients are 10<sup>11</sup> cm<sup>3</sup>/s, and the plume feedstock consists of only hydrogen, argon, and less than 1% hydrocarbon. Therefore, the chemical composition of the freestream is in nearly frozen, and we do not expect large gradients in concentrations along the centerline of the freestream of the plume.<sup>5,51</sup> Our measurements of the ground state concentrations of the reactive intermediates H,<sup>52</sup> CH, C<sub>2</sub>, and C<sub>3</sub><sup>13</sup> find only modest concentration variations between the nozzle and the boundary layer (Fig. 9, lower panel); H, CH, and C<sub>2</sub> decrease less than a factor of 2 and C<sub>3</sub> increases approximately a factor of 2.

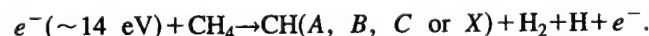
Except for C<sub>2</sub>(d), all of the excited state concentrations in Fig. 9 decrease at least a factor of 100 between the nozzle exit and the boundary layer. Thus, chemiluminescent reaction can be the dominant excitation pathway only for the C<sub>2</sub> swan band (d-a) emission. The most likely reaction to explain the chemiluminescence of C<sub>2</sub>, as suggested by Brinkman<sup>30</sup> and Wakisaka,<sup>53</sup> is the formation of C<sub>2</sub>(d) by three body recombination:



This is consistent with the predictions,<sup>5,51</sup> that in the arcjet plume with its large molefraction of atomic hydrogen, atomic carbon is the most abundant carbon species.

Electron impact is an important excitation mechanism for much of the optical emission in the plume. The electron number density is the only plasma parameter with a significant variation along the vertical axis, with ~10<sup>12</sup> electron/cm<sup>3</sup> at 12 mm downstream from the exit plane of the nozzle which decreases by an order of magnitude at 32 mm downstream.<sup>33</sup> Measurements and models of electron densities in dc arcjets show the electron number density is much higher inside the nozzle than in the plume.<sup>41</sup> Thus, the electron density declines rapidly with distance from the nozzle exit similar to the decrease in optical emission, and the high electron density in the nozzle region contributes to enhance the dissociation of methane.

Electron impact dissociation of methane can have excited CH products when the electron energy is greater than the appearance potential of approximately 14 eV



At higher electron energies, excited H, C, and CH<sup>+</sup> species as products are possible.<sup>49,54–57</sup> Hydrocarbon fragments can also be dissociated or excited by direct electron impact.<sup>58</sup> For example, the CH radical can be directly excited by low energy electrons



The most abundant two-carbon hydrocarbon in the arcjet plume was measured and predicted to be C<sub>2</sub>H<sub>2</sub>.<sup>59</sup> Its electron impact dissociation has been studied<sup>48,56,57,60</sup> and the electronically excited fragments detected, in addition to the ones observed from methane, are the C<sub>2</sub>(d), C<sub>2</sub>(C), and C<sub>2</sub>(D).<sup>56,60</sup> We find emission from all of these radicals in the dc-arcjet plume. Collisions of metastable argon atoms could contribute to the excitation mechanism. However, argon metastables are very rapidly deactivated by molecular hydrogen,<sup>61</sup> and we estimate a lifetime in the plume of less than 0.5 μs. Even at the fast directed plume flow of 2.5 km/s, the argon metastables are collisionally deactivated in the nozzle or in the first few mm of the freestream plume.

Assuming the number density of electrons in the plume decreases with distance with a constant electron temperature, we should observe the same gradient in the excited state emission for all the species produced by electronic impact. However, we find a different slope β for each excited species, and Fig. 10 shows the correlation of β with the excitation energy. We see a remarkable linear correlation between



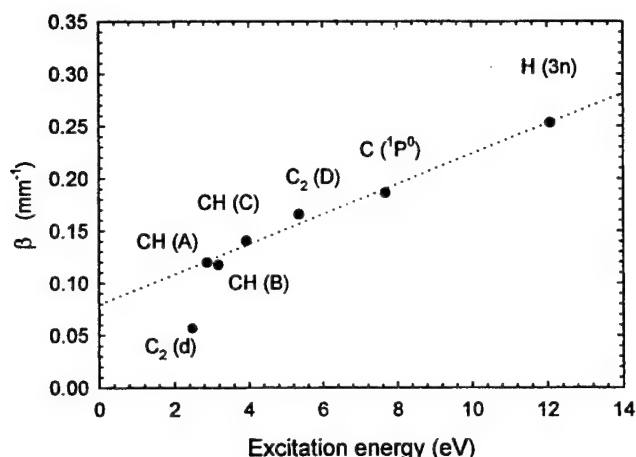


FIG. 10. Variation of the exponential factor  $\beta$  vs excitation energy of the corresponding radical or atom.

$\beta$  and the excitation energy, with only  $C_2(d)$  falling off this line. We find a similar correlation between the appearance potential for electron impact dissociation to produce excited  $CH(A)$ ,  $CH(B)$ , and  $CH(C)$  from methane, excited  $C_2(D)$  from  $C_2H_2$ , and excited H from  $H_2$ . Thus, we could explain the spatial distribution of optical emission for all the species except  $C_2(d)$  with an electron impact excitation mechanism if the high energy tail of the distribution depletes with distance from the nozzle in addition to the drop in electron density. Such a decrement is consistent with the Langmuir probe observation<sup>33</sup> that the high energy component to the electron distribution was greatly reduced by the addition of hydrocarbon molecules into the plume.

## 2. Effect of methane addition

The amount of methane in the gas mixture is one of the most critical parameters controlling the growth rate and quality of the deposited diamond films. Methane addition also reduces the electron temperature and number density in the plume of the dc-arcjet plasma. We found feedstock mixtures of Ar and  $H_2$  without added methane had bimodal electron energy distributions characterized by temperatures  $\sim 2$  and  $\sim 8$  eV, respectively,<sup>33</sup> when methane is added, the high energy component disappears. This observation is common to other plasma reactors with  $H_2$  and  $CH_4$  mixtures.<sup>62</sup> The addition of methane, a polyatomic collision partner with many low-energy vibrational modes and overtones, provides efficient relaxation of the high energy electrons in the plasma plume.<sup>63</sup> Thus, as seen in Fig. 11, the addition of methane significantly reduces the H atom optical emission, consistent with an electron impact excitation mechanism.

Figure 11 shows excited state densities deduced from the optical emission near the nozzle, in the arcjet plume, and in the shock heated boundary layer as a function of methane addition. Near the nozzle, the addition of methane produces a strong decrease in the H atom concentration, and the rise of emission from carbon containing species from electronic impact dissociation of hydrocarbons; above 1% of methane addition, this increase slows. In the arcjet plume, the atomic hydrogen emission decreases with methane addition; the emission increases for the C species up to 0.5% of added methane, but beyond this value, emission from all the C species except  $C_2(d)$  decreases. The  $C_2(d)$  behavior is consistent with the hypothesis of a chemiluminescent production mechanism from atomic carbon recombination. The rise and fall of the other species is related to the depletion of electron

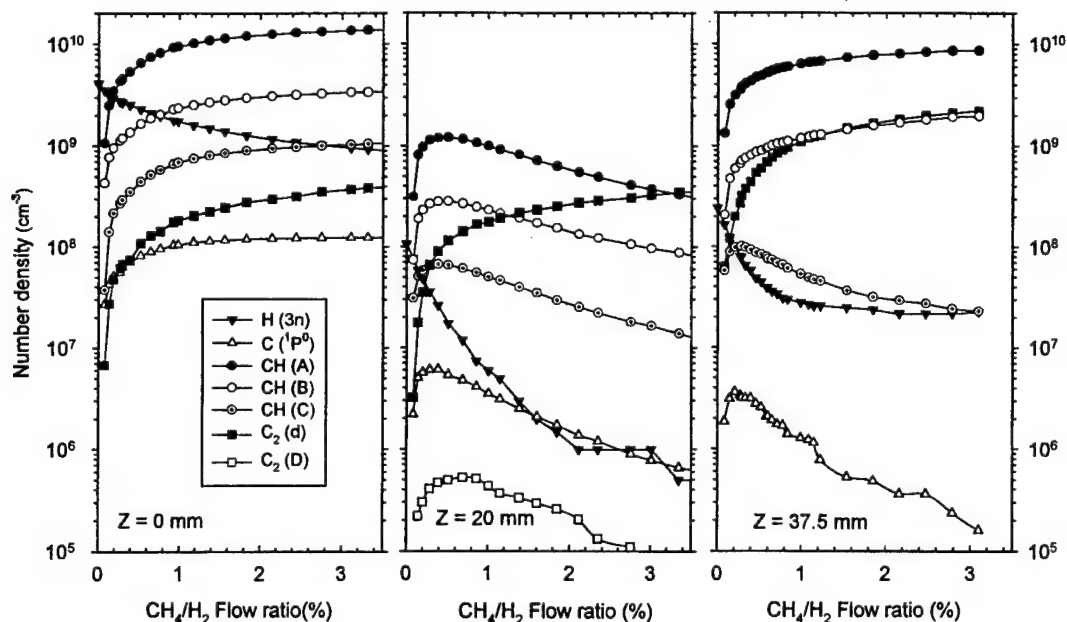


FIG. 11. Variation of excited state number density vs methane addition near the nozzle ( $z=0$ ), in the freestream of the plume ( $z=20$  mm), and in the shock heated boundary layer ( $z=57.5$  mm).

energy and number density, similar to the reduction in emission with distance seen in Fig. 9 for constant methane addition. Finally, in the shock heated boundary layer, where the temperature and pressure are higher than in the other regions, there are more paths for the radical production. Excitation of H, C, and CH(C) by electron impact is still likely, but CH(A), CH(B), and C<sub>2</sub>(d) are proportional to the methane flow and more likely to be produced by chemiluminescent reactions. At this point, we do not know which reactions are responsible for CH(A) and CH(B) production, nor why the CH(C) is not chemically produced.

## V. SUMMARY AND CONCLUSIONS

In the arcjet plume, the predominant production mechanism of electronically excited H\*, C\*, CH(A), CH(B), CH(C), CH<sup>+</sup>(A), C<sub>2</sub>(C), and C<sub>2</sub>(D) is electronic impact excitation, whereas C<sub>2</sub>(d) is the product of chemiluminescent reactions. The excited state populations are several orders of magnitude lower than the ground state, with peak concentrations near the nozzle, where the electron density is higher. The spatial variation of excited state number density is quite different than the spatial distribution of the ground state atoms and radicals. The number density of excited states is sufficiently low that excited state chemistry is unlikely to play any important role in the overall chemistry of diamond CVD.

## ACKNOWLEDGMENTS

This work is supported by ARPA via contract with the Naval Research Laboratory, the Army Research Office, and the Air Force Office of Research. W. Juchmann is sponsored by Universität Heidelberg via Landesgraduiertenförderung. We thank Professor Mark Cappelli of Stanford University for the loan of an arcjet and his assistance in the design of the diamond CVD reactor.

<sup>1</sup>N. Ohtake and M. Yoshikawa, *J. Electrochem. Soc.* **137**, 717 (1990).

<sup>2</sup>J. E. Butler and R. L. Woodin, *Philos. Trans. R. Soc. London* **342**, 209 (1993).

<sup>3</sup>D. G. Goodwin, *J. Appl. Phys.* **74**, 6888 (1993).

<sup>4</sup>D. G. Goodwin, *Appl. Phys. Lett.* **59**, 277 (1991).

<sup>5</sup>M. E. Coltrin and D. S. Dandy, *J. Appl. Phys.* **74**, 5803 (1993).

<sup>6</sup>P. C. Redfern, D. A. Horner, L. A. Curtiss, and D. M. Gruen, *J. Phys. Chem.* **100**, 11654 (1996).

<sup>7</sup>M. Frencklach and H. Wang, *Phys. Rev. B* **43**, 1520 (1991).

<sup>8</sup>L. L. Connell, J. W. Fleming, H. N. Chu, J. D. J. Vesteyck, E. Jensen, and J. E. Butler, *J. Appl. Phys.* **78**, 3622 (1995).

<sup>9</sup>K. Donnelly, D. P. Dowling, T. P. O'Brien, A. O'Leary, T. C. Kelly, R. Cheshire, K. F. Al-Assadi, W. G. Graham, T. Morrow, V. Kornas, V. S.-V. d. Gathern, and H. F. Doble, *Diamond Relat. Mater.* **4**, 324 (1995).

<sup>10</sup>W. Juchmann, J. Luque, and J. B. Jeffries, *J. Appl. Phys.* **81**, 8052 (1997).

<sup>11</sup>M. A. Childs, K. L. Menningen, L. W. Anderson, and J. E. Lawler, *J. Chem. Phys.* **104**, 9111 (1996).

<sup>12</sup>C. Kaminski and P. Ewart, *Appl. Phys. B: Photophys. Laser Chem.* **61**, 585 (1995).

<sup>13</sup>J. Luque, W. Juchmann, and J. B. Jeffries, *J. Appl. Phys.* **82**, 2072 (1997).

<sup>14</sup>M. A. Childs, K. L. Menningen, H. Toyoda, L. W. Anderson, and J. E. Lawler, *Europhys. Lett.* **25**, 729 (1994).

<sup>15</sup>K. L. Menningen, M. A. Childs, H. Toyoda, Y. Ueda, L. W. Anderson, and J. E. Lawler, *Contrib. Plasma Phys.* **35**, 359 (1995).

<sup>16</sup>F. Hummerbrum, H. Kempkens, A. Ruzicka, H. D. Sauren, C. Schiffer, J. Uhlenbusch, and J. Winter, *Plasma Sources Sci. Technol.* **1**, 221 (1992).

<sup>17</sup>W. Jacob, M. Engelhard, and W. Moller, *Appl. Phys. Lett.* **64**, 971 (1994).

<sup>18</sup>P. Zalicki, Y. Ma, R. N. Zare, J. R. Dadamio, E. H. Wahl, T. G. Owano, and C. H. Kruger, *Chem. Phys. Lett.* **234**, 269 (1995).

<sup>19</sup>P. Zalicki, Y. Ma, R. N. Zare, E. H. Wahl, T. G. Owano, and C. H. Kruger, *Appl. Phys. Lett.* **67**, 144 (1995).

<sup>20</sup>S. Kim, D. P. Billesbach, and R. Dillon, *J. Vac. Sci. Technol. A* **15**, 2247 (1997).

<sup>21</sup>D. G. Goodwin and J. E. Butler, in *HandBook of Industrial Diamond and Films*, edited by M. Prelas, G. Popovicii, and K. K. Bigelow (Marcel Dekker, New York, 1997).

<sup>22</sup>R. J. H. Klein-Douwle, J. J. L. Spaanjaars, and J. J. ter Meulen, *J. Appl. Phys.* **78**, 2086 (1995).

<sup>23</sup>T. Lang, J. Stiegler, Y. v. Kaenel, and E. Blank, *Diamond Relat. Mater.* **5**, 1171 (1996).

<sup>24</sup>H. C. Barshilla and V. D. Vankar, *J. Appl. Phys.* **80**, 3694 (1996).

<sup>25</sup>D. M. Gruen, C. D. Zuiker, A. R. Krauss, and X. Pan, *J. Vac. Sci. Technol. A* **13**, 1628 (1995).

<sup>26</sup>J. Cui and R. Fang, *J. Appl. Phys.* **81**, 2851 (1997).

<sup>27</sup>G. A. Raiche and J. B. Jeffries, *Appl. Opt.* **32**, 4629 (1993).

<sup>28</sup>S. W. Reeve and W. A. Weimer, *J. Vac. Sci. Technol. A* **13**, 359 (1995).

<sup>29</sup>J. C. Cubertafon, M. Chenevier, A. Campargue, G. Vervan, and T. Priem, *Diamond Relat. Mater.* **4**, 350 (1995).

<sup>30</sup>E. A. Brinkman, G. A. Raiche, M. S. Brown, and J. B. Jeffries, *Appl. Phys. B: Photophys. Laser Chem.* **64**, 689 (1997).

<sup>31</sup>J. Luque, W. Juchmann, and J. B. Jeffries, *Appl. Opt.* **36**, 3261 (1997).

<sup>32</sup>G. A. Raiche and J. B. Jeffries, *Appl. Phys. B: Photophys. Laser Chem.* **65**, 593 (1997).

<sup>33</sup>E. A. Brinkman, K. R. Stadler, and J. B. Jeffries, *J. Appl. Phys.* **81**, 1093 (1997).

<sup>34</sup>J. Luque and D. R. Crosley, *Appl. Phys. B: Photophys. Laser Chem.* **63**, 91 (1996).

<sup>35</sup>M. J. Buie, J. T. P. Pender, J. P. Holloway, T. Vincent, P. L. G. Ventek, and M. L. Brake, *J. Quant. Spectrosc. Radiat. Transf.* **55**, 231 (1996).

<sup>36</sup>J. T. Salmon and N. M. Laurendeau, *Appl. Opt.* **24**, 65 (1985).

<sup>37</sup>J. C. Han, C. Ye, M. Suto, and L. C. Lee, *J. Chem. Phys.* **90**, 4000 (1989).

<sup>38</sup>W. R. Graham, K. I. Dismuke, and W. Weltner, *Astrophys. J.* **204**, 301 (1976).

<sup>39</sup>G. Pacchioni and J. Koutecký, *J. Chem. Phys.* **88**, 1066 (1988).

<sup>40</sup>W. L. Wiese, M. W. Smith, and B. M. Glennon, *Atomic Transition Probabilities* (National Bureau of Standards, 1966).

<sup>41</sup>P. V. Storm and M. A. Cappelli, *J. Quant. Spectrosc. Radiat. Transf.* **56**, 901 (1996).

<sup>42</sup>J. Luque and D. R. Crosley, LIFBASE 1.1 edition, SRI International Report MP 96-001, 1996 (<http://www.SRI.com/CEM/LIFBASE>).

<sup>43</sup>J. L. Cooper and J. C. Whitehead, *J. Chem. Soc. Faraday Trans.* **1992**, 2323 (1992).

<sup>44</sup>M. Martin and M. Castillejo, *Chem. Phys. Lett.* **266**, 111 (1997).

<sup>45</sup>J. Luque, *Chem. Phys. Lett.* **206**, 185 (1996).

<sup>46</sup>W. Ubachs, G. Meyer, J. J. ter Meulen, and A. Dymanus, *J. Chem. Phys.* **84**, 3032 (1986).

<sup>47</sup>J. Brzozowski, P. Bunker, N. Elander, and P. Erman, *Ap. J.* **207**, 414 (1976).

<sup>48</sup>K. Furuya, A. Matsuo, M. Tokeshi, and T. Ogawa, *J. Phys. Chem.* **99**, 13722 (1995).

<sup>49</sup>K. Furuya, T. Ueda, M. Tokeshi, and T. Ogawa, *Chem. Phys.* **221**, 303 (1997).

<sup>50</sup>K. Devriendt, H. V. Look, B. Ceusters, and J. Peeters, *Chem. Phys. Lett.* **261**, 450 (1996).

<sup>51</sup>G. P. Smith and J. B. Jeffries, in *Diamond Materials*, edited by A. J. Purdes, J. C. Angus, R. F. D. Iles, B. M. Meyerson, K. E. Spear, and M. Yoder (Electrochemical Society Press, Pennington, NJ, 1991), pp. 194–201.

<sup>52</sup>W. Juchmann, J. Luque, and J. B. Jeffries (unpublished).

<sup>53</sup>A. Wakisaka, J. J. Gaumet, Y. Shimizu, and Y. Tamori, *J. Chem. Soc. Faraday Trans.* **89**, 1001 (1993).

<sup>54</sup>K. Motohashi, H. Soshi, M. Ukai, and S. Tsurubuchi, *Chem. Phys.* **213**, 369 (1996).

<sup>55</sup>D. E. Donohue, J. A. Schiavone, and R. S. Freund, *J. Chem. Phys.* **67**, 769 (1977).

<sup>56</sup>C. I. M. Beenakker and F. J. d. Heer, *Chem. Phys.* **7**, 130 (1975).

- <sup>57</sup>M. Tokeshi, K. Nakashima, and T. Ogawa, *Chem. Phys.* **203**, 257 (1996).
- <sup>58</sup>L. E. Kline, W. D. Partlow, and W. E. Bies, *J. Appl. Phys.* **65**, 70 (1989).
- <sup>59</sup>S. W. Reeve, W. A. Weimer, and F. M. Cerio, *J. Appl. Phys.* **74**, 7521 (1993).
- <sup>60</sup>C. I. M. Beenakker and F. J. d. Heer, *Chem. Phys.* **6**, 291 (1974).
- <sup>61</sup>J. E. Velazco, J. H. Kolts, and D. W. Setzer, *J. Chem. Phys.* **69**, 4537 (1978).
- <sup>62</sup>R. I. Cherry and T. D. Whitmore, *Diamond Relat. Mater.* **4**, 524 (1995).
- <sup>63</sup>A. Jelenak, J. V. Jovanovic, S. A. Bzenic, S. B. Vrhovac, S. S. Manola, B. Tomcik, and Z. L. Petrovic, *Diamond Relat. Mater.* **4**, 1103 (1995).
- <sup>64</sup>J. Hinze and G. C. Lie, *Ap. J.* **196**, 621 (1975).
- <sup>65</sup>J. Brzozowski, N. Elander, P. Erman, and M. Lyra, *Ap. J.* **193**, 741 (1974).
- <sup>66</sup>L. Curtis, B. Engmam, and P. Erman, *Phys. Scr.* **13**, 270 (1976).
- <sup>67</sup>D. K. Otorbaer, A. J. M. Buuron, J. W. Gielew, M. C. Vander Sanden, and D. C. Schran, *Diamond Relat. Mater.* **4**, 908 (1995).

## **APPENDIX G**

**ATOMIC HYDROGEN CONCENTRATION IN A DIAMOND DEPOSITING DC-ARCJET DETERMINED BY CALORIMETRY, J. APPL. PHYS. 81, 8052 (1997).**

# Atomic hydrogen concentration in a diamond depositing dc arcjet determined by calorimetry

W. Juchmann,<sup>a)</sup> J. Luque, and J. B. Jeffries

Molecular Physics Laboratory, SRI International, 333 Ravenswood Avenue, Menlo Park, California 94025

(Received 17 January 1997; accepted for publication 17 March 1997)

The fraction of hydrogen dissociated in the plume of a dc arcjet used for diamond deposition is determined by calorimetry to be  $0.33 \pm 0.12$ . A dc arc is struck in a mixture of argon and hydrogen at 90 psi and the effluent is expanded through a converging/diverging nozzle into a reactor maintained at 25 Torr. Methane ( $< 1\%$ ) is added to the luminous gas plume in the diverging nozzle. This supersonic jet impinges on a water cooled molybdenum substrate, and diamond thin film grows from the reactive mixture. The electrical power input of the arcjet (1.6 kW) is balanced by the power losses due to cooling of the nozzle, enthalpy change in the gas, ionization of the gas, dissociation of  $H_2$ , and the directed velocity of the gas phase. The gas temperature is determined by linear laser-induced fluorescence (LIF) measurements of several rotational lines of NO seeded to the gas plume. The velocity of the gas plume is obtained via the Doppler shift between LIF signals measured simultaneously in a stationary reference cell and in the arcjet. The atomic hydrogen fraction increases as a function of the feedstock  $H_2/Ar$  ratio and with increasing input power to the arcjet. © 1997 American Institute of Physics. [S0021-8979(97)04112-1]

## I. INTRODUCTION

Thin films of diamond deposited by chemical vapor deposition (CVD) are used in a variety of industrial applications such as thermal management, wear resistant tool coatings, and optical windows. Over the past ten years, a great deal of research has been undertaken to understand the basic chemistry and physics of thin film diamond, and results of this research were recently summarized by Goodwin and Butler.<sup>1</sup> CVD diamond is grown in a wide variety of reactor designs with a plethora of feedstock gas recipes; however, nearly all these techniques can be reduced to the growth of CVD diamond from a small amount of hydrocarbon added to a hydrogen plasma.

A mechanistic view of CVD diamond growth has evolved from the insight of many researchers.<sup>1-7</sup> Atomic hydrogen plays a crucial role in this mechanism; gas-surface abstraction reactions of atomic hydrogen produce active radical sites on the growing diamond surface, carbon containing radicals bind to these sites, and recombination reactions terminate the surface carbon to maintain  $sp^3$  bonding. Using this mechanistic view of diamond growth, Goodwin<sup>8</sup> and Bachmann *et al.*<sup>9</sup> developed scaling laws for growth rates and material quality that depend strongly on the amount of atomic hydrogen.

High quality diamond film can be grown in a dc-arcjet reactor with deposition rates of up to  $100 \mu m/h$ , among the fastest of any growth rates reported.<sup>10-12</sup> In an arcjet reactor, a dc arc is struck in the feedstock gas, this effluent is expanded through a converging/diverging nozzle into the reactor, and diamond grows from the stagnation point flow of reactive gas onto a substrate. These reactors are attractive candidates<sup>13-16</sup> for testing the models of diamond CVD because of the well-defined gas residence time in the reactive

plume and rapid growth rate. The gas phase chemical composition of a dc-arcjet plume is strongly dependent on the atomic hydrogen concentration. Coltrin and Dandy<sup>15</sup> parameterize their model results as a function of the hydrogen dissociation for the very wide range between 0.05 and 0.95. To further understand the CVD process and to test the existing models, it is therefore necessary to determine the absolute concentration of atomic hydrogen in dc-arcjet reactors.

Atomic hydrogen has been measured in hot filament reactors using nonintrusive, *in situ* optical detection techniques including laser-induced fluorescence,<sup>17</sup> resonance enhanced multiphoton ionization,<sup>18</sup> and third-harmonic generation.<sup>19</sup> It has also been measured by mass spectroscopy of the molecular beam sampled through a hole in the substrate.<sup>20,21</sup> Indirect probe measurements have determined atomic hydrogen content in hot filament reactors by measuring the heat input to a probe from the heterogeneous recombination of atomic hydrogen to form  $H_2$ .<sup>22,23</sup> However, measurements<sup>24-26</sup> of atomic hydrogen in arcjet plumes have been limited to very low pressure reactors (few mTorr) to study arcjet thrusters and none of these measurements was performed during diamond deposition.

We report the determination of the atomic hydrogen mole fraction in the reactive plume of a dc-arcjet reactor using a detailed power balance. The electrical input power is balanced with the power losses due to arcjet-nozzle cooling, radiation, ionization, enthalpy change, and directed velocity of the gas phase species. From this balance the hydrogen dissociation rate can be determined.

## II. EXPERIMENT

In our CVD reactor, schematically shown in the inset in Fig. 1, a 0.7 MPa (90 psi) mixture of  $H_2/Ar$  (0.8:1, 7 slm total flow) is activated by a dc discharge and expands through a converging/diverging water-cooled nozzle into a reactor maintained at constant pressure (nominally 3.3 kPa or

<sup>a)</sup>Permanent address: Physikalisch Chemisches Institut, Universität Heidelberg, Germany.

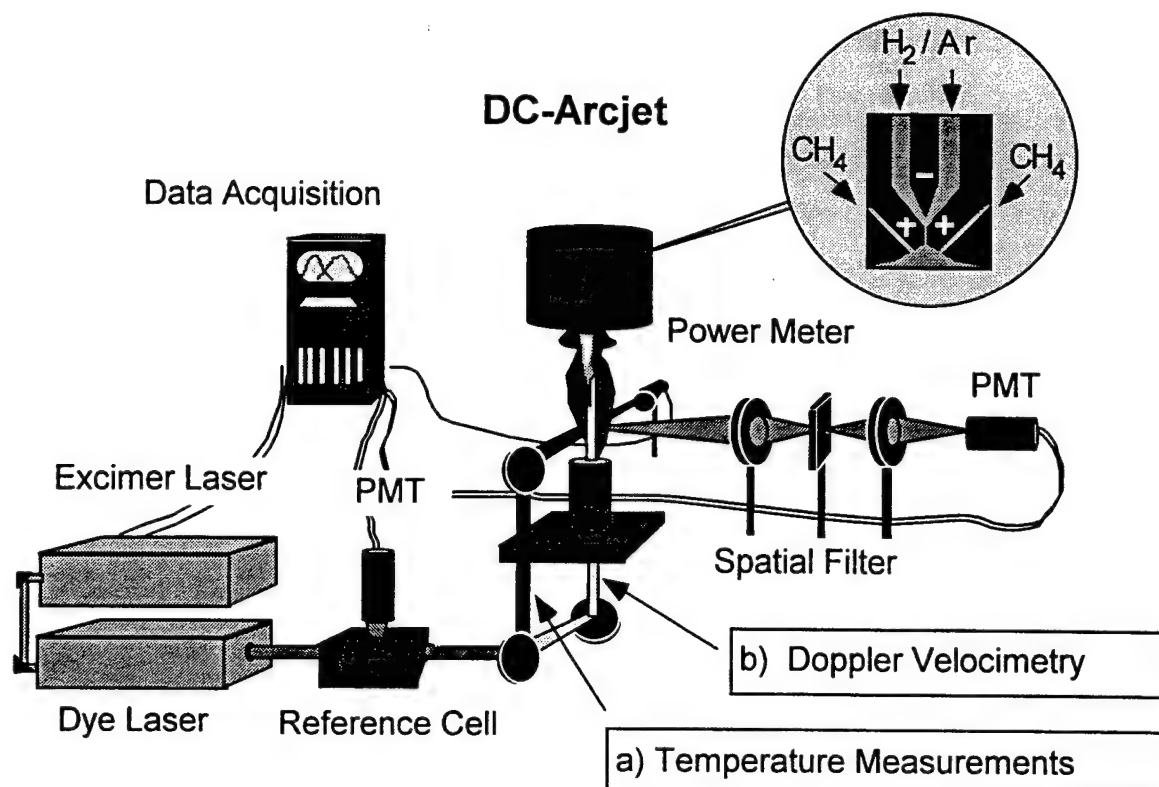


FIG. 1. Experimental setup for gas temperature measurements (case a) and Doppler velocimetry (case b) in a dc arcjet using laser induced fluorescence.

25 Torr). Methane ( $\sim 0.5\%$  of the H<sub>2</sub> flow) is injected into the flow in the diverging section of the nozzle. The luminous, chemically reactive gas mixture forms a supersonic stagnation point flow onto a water-cooled molybdenum substrate (38 mm from the nozzle exit), where diamond grows at an average growth rate of approximately 50  $\mu\text{m}/\text{h}$ . The extremely high quality diamond deposited using our standard conditions is demonstrated in Figs. 2 and 3. A scanning electron micrograph (Fig. 2) of the surface morphology shows the (111) texture of a free-standing 500- $\mu\text{m}$ -thick diamond plate, and Fig. 3 shows a Raman spectrum of the same diamond sample. This spectrum was taken using a cw argon ion

laser with an unfocused 300  $\mu\text{m}$  spot size. It shows a characteristic diamond peak at  $1332\text{ cm}^{-1}$ , which is more than 20 times the nonresonant background luminescence. There are no signs of graphitic impurities. The  $2.2\text{ cm}^{-1}$  full width at half-maximum (FWHM) of the diamond Raman line is indistinguishable from the linewidth observed in this Raman spectrometer from natural type IIa diamond.

#### A. Calorimetry

We determined the amount of dissociation of feedstock hydrogen using a detailed power balance:

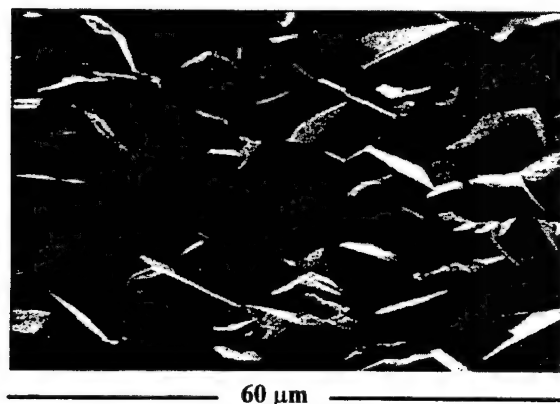


FIG. 2. Scanning electron micrograph of the CVD diamond deposited in the arcjet.

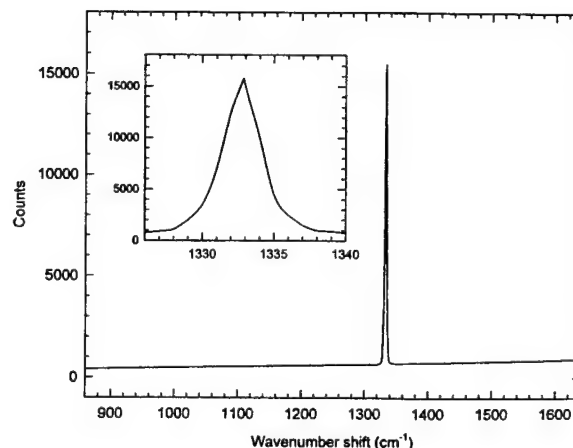


FIG. 3. Raman spectrum of the CVD diamond in Fig. 2.



$$P_{H_2 \text{ dissociation}} = P_{in} - (P_{cooling} + P_{radiation} + P_{ionization} + P_{heating} + P_{accelerating}). \quad (1)$$

The voltage drop in the arc and the arc current were measured to determine the input power. This is balanced with the power losses of the nozzle water cooling, radiation from activated gases, gas ionization, the temperature rise in the gas, and the power to accelerate the gases and produce the directed velocity of the plume.

Values for all these terms except gas temperature and gas velocity can be monitored routinely. At our standard conditions the arc current is 11.4 A and the voltage drop is 140 V for a power input of 1600 W. The converging/diverging nozzle is water cooled, and the flow and temperature rise of this coolant are monitored; at standard conditions 485 W are lost to the cooling water. The plume of the arcjet has atomic line and molecular band emission leading to a loss term due to radiation. We integrate this emission and estimate a blackbody radiation loss with a generous upper bound of 50 W. Langmuir probe measurements<sup>27</sup> show that the ion density in the plume is less than  $10^{13}$  ions/cm<sup>3</sup>, resulting in a negligible power loss (1 W) to gas ionization. In the high pressure arc, the ion density is much larger than this value. However, most of the ions and electrons apparently recombine on the tungsten surface of the converging/diverging nozzle, producing part of the large heat load to the nozzle. Very similar ion densities were measured in a radiation cooled arcjet thruster.<sup>26</sup>

## B. Gas temperature and velocity measurements

We use laser-induced fluorescence (LIF) of NO seeded into the gas plume (0.11% of total flow) to determine the gas temperature and velocity. LIF is a well established probe of gas temperature and velocity in combustion systems.<sup>28,29</sup> NO is relatively unreactive in this environment and therefore is not expected to change the gas temperature or the flow dynamics. LIF measurements of CH in the arcjet plume during diamond deposition and NO seeded into the flow give identical gas temperatures.<sup>30</sup> Even though the Langmuir probe measurements<sup>27</sup> show an increase in the ion density when NO is added to the flow, this is a negligible perturbation to the power balance. Having 7 slm of gas flowing through a 10 mm-diameter into a 25 Torr reactor, we expect the NO molecules to have reached the mean velocity of the other species by the time they pass the nozzle exit, where the velocity is measured.

A tunable, pulsed excimer-pumped dye laser (10 ns pulse width,  $\sim 0.3$  cm<sup>-1</sup> bandwidth, frequency doubled with a BBO crystal) produces the light to excite the NO  $A^2\Sigma^+ - X^2\Pi$  transition near 226 nm. The laser beam, with energies around 1  $\mu$ J to avoid saturation of the spectroscopic transitions, is constricted with a 1-mm-diam aperture and aligned through the arcjet plume perpendicular to the directed velocity. The fluorescence is collected perpendicular to both plume and laser beam. The collected light is spatially filtered with an aperture to 1 mm resolution and is detected broadband using a solar blind photomultiplier (Hamamatsu R166H) with an UG-5 colored glass filter (Schott). The spec-

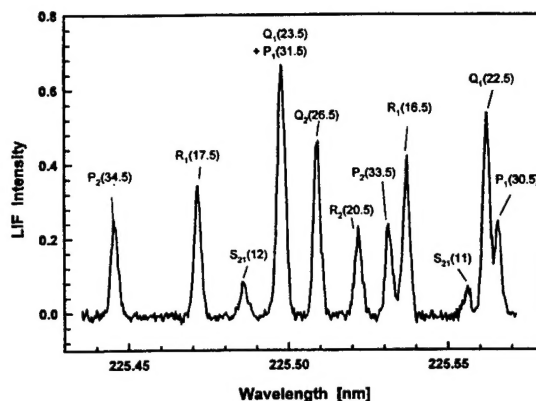


FIG. 4. Excitation LIF of seeded NO A-X (0,0) for gas temperature measurements in a dc arcjet.

tral bias introduced by the filter was less than 3%. A boxcar is used to time integrate the fluorescence. A section of the excitation spectrum of the (0,0) band of the NO A-X transition is shown in Fig. 4. The gas temperature is determined from the rotational temperature derived by Boltzmann analysis of such spectra. We find the gas temperature to be 2200 K at the exit of the nozzle in the middle of the arcjet plume with a statistical uncertainty of 100 K. These results are in good agreement with rotational temperature measurements on CH B-X previously reported.<sup>31</sup> Storm and Cappelli found similar gas temperatures in 1 kW radiatively cooled arcjets.<sup>32</sup>

The directed gas velocity of the arcjet plume is determined from Doppler shift measurements of LIF of NO seeded into the gas flow. The laser beam is aligned through a 3-mm-diam hole in the substrate into the counter-propagating gas plume as shown in Fig. 1. Before the laser beam enters the CVD reactor, it passes through a reference cell filled with NO ( $\sim 1$  Torr). A second detection system collects the NO LIF signal from the stationary reference. The LIF signal from both the reference and the arcjet are shown in Fig. 5 for excitation of the  $R_1(17.5)$  of the NO A-X (0,0) transition. Both spectra are fit to a Gaussian shape using a Lavenberg-Marquadt least-squares algorithm. The Doppler shift of the two line centers gives the directed velocity  $v = c\Delta\lambda/\lambda$ , where  $c$  is the speed of light,  $\Delta\lambda$  represents the

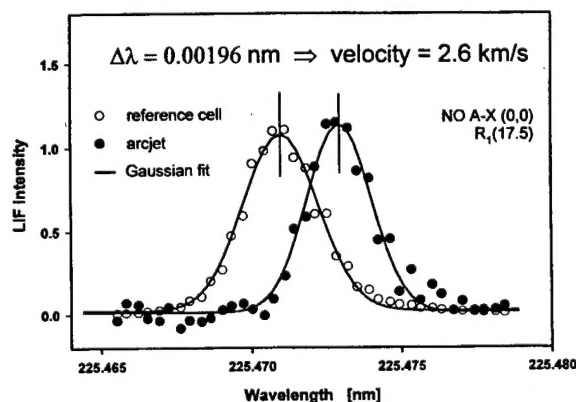


FIG. 5. LIF of seeded NO in the reference cell (open circles) and in the arcjet (closed circles) fitted to a Gaussian (line) for Doppler velocimetry.

TABLE I. Power balance to determine the fraction of hydrogen dissociation.

<b>Power into the arcjet</b>	
Power supply:	1600±32 W
<b>Power losses</b>	
Cooling water	485±55 W
Accelerating the gases	410±82 W
Heating the gases	330±50 W
Radiative loss (estimated)	<50 W
Ionization	<1 W
<b>Power to dissociate</b>	
÷ Energy to dissociate H <sub>2</sub>	4.35×10 <sup>5</sup> J/mol
Rate of atomic hydrogen	7.3×10 <sup>-4</sup> mol/s
⇒ Fraction of dissociation	0.33±0.12

Doppler shift, and  $\lambda$  is the excitation wavelength. We find the directed velocity of the plume to be  $v = 2600 \pm 100$  m/s in the center of the plume at the exit plane of the nozzle. The bandwidth of the laser dominates the linewidth in Fig. 5 for the reference cell data and is a significant contribution to the linewidth observed in the arcjet plume. The single scan measurement of both the Doppler shifted signal and the reference signal avoids any calibration uncertainty in wavelength. Great care was taken to avoid problems in the linearity of the laser step size due to backlash in the stepper motor when scanning back and forth. Since the directed velocity is greater than the speed of sound in this system ( $v_{\text{sound}} = 1.2$  km/s), the free stream velocity is not perturbed by the hole in the substrate. Of course, any measurements near the substrate would be influenced.

### C. Determination of atomic hydrogen

We can now use Eq. (1) to determine the fraction of the feedstock hydrogen that is dissociated in the arcjet plume. We define the dissociation fraction,  $X = 0.5(n_{\text{H}}/n_{\text{H}_2})$ , where  $n_{\text{H}}$  is the number of moles for atomic hydrogen and  $n_{\text{H}_2}$  is the initial number of moles of molecular hydrogen in the feedstock gas. If all hydrogen molecules are dissociated, the fraction of dissociation is  $X = 1$ . The hydrogen heat of formation is 43.5 kJ/mole; we determine  $X$  from

$$\begin{aligned}
 P_{\text{in}} &= P_{\text{cooling}} - P_{\text{radiation}} - P_{\text{ionization}} \\
 &= (C_p^{\text{Ar}} \cdot \Delta T + \frac{1}{2} v^2 \cdot 39.95 \times 10^{-3}) n_{\text{Ar}}, \\
 &= (C_p^{\text{H}_2} \cdot \Delta T + \frac{1}{2} v^2 \cdot 2.016 \times 10^{-3}) (1 - X) n_{\text{H}_2}, \\
 &= (C_p^{\text{H}} \cdot \Delta T + \frac{1}{2} v^2 \cdot 1.008 \times 10^{-3}) 2X \cdot n_{\text{H}}, \quad (2)
 \end{aligned}$$

where  $C_p$  is the specific heat capacity,  $v$  the directed gas velocity,  $\Delta T$  the difference between room temperature and gas temperature, and  $n$  the gas flow is in mol/s.

We find the fraction of hydrogen dissociated is  $0.33 \pm 0.12$  at our standard diamond deposition conditions; the power balance data are summarized in Table I. The value of 0.33 is a lower limit because we assume the maximum temperature and velocity to be constant over the entire exit plane of the nozzle. If we calculate the fraction of dissociation for the average temperatures and velocity at the exit plane of the nozzle, we find a dissociation fraction of 0.51, in good agree-

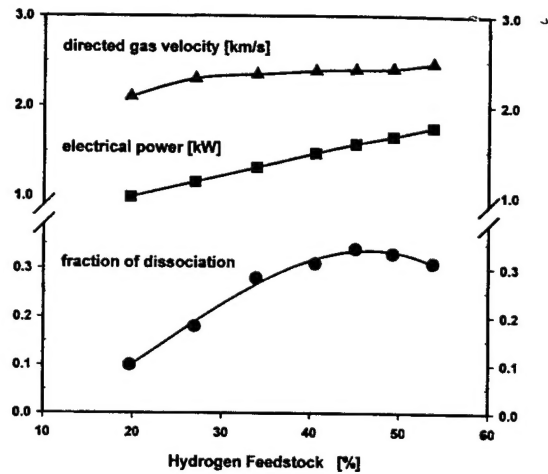


FIG. 6. Power, velocity, and fraction of atomic hydrogen vs hydrogen feedstock gas.

ment with the results of Probst *et al.*<sup>24</sup> who find a dissociation fraction of  $\sim 0.50$  for a 1 kW arcjet thruster operating on pure hydrogen feedstock in a reactor at pressures of a few mTorr.

As the ratio of hydrogen to argon in the feedstock is varied, we find a maximum in the hydrogen dissociation. The variation of arcjet power, gas velocity, and hydrogen dissociation is shown in Fig. 6 as a function of the fraction of hydrogen in the feedstock. The gas temperature remains constant within 5% for this range of reactor conditions. The velocity increases steadily with increasing molecular hydrogen feedstock. As the fraction of hydrogen in the feedstock increases, the arc voltage increases for a given current, thereby increasing the operating power. This is a typical current-voltage characteristic of a supersonic dc arcjet due to the negative impedance of the arc column.<sup>33</sup> At 50% hydrogen feedstock, the dissociation fraction in Fig. 6 shows a maximum. A similar relationship was measured<sup>30</sup> for the CH concentration as a function of the H<sub>2</sub>/Ar ratio; the CH concentration increased with increased hydrogen. This correlation between H atoms and CH molecules agrees with the model predictions<sup>13-15</sup> that H and CH are in partial equilibrium in the free stream of the arcjet plume.

The method presented is adequate for measuring large dissociation fractions of hydrogen in plasma reactors and has some very important advantages over quantitative spectroscopic techniques in the case of supersonic gas jets. A problem related with compressible flows is the uncertainty of the local pressure at the nozzle exit, which usually does not correspond to the background pressure. As a consequence, knowing the degree of dissociation requires the number density determination of both H and H<sub>2</sub>, and the error associated with the two independent concentration measurements is at least of the same order as in the power balance method.<sup>24</sup>

### III. SUMMARY

A detailed power balance determines the dissociation fraction of hydrogen in the plume of a diamond depositing dc arcjet. The gas temperature at the nozzle exit is measured



by LIF on seeded NO to be 2200 K, and the directed gas velocity is determined to be 2600 m/s by Doppler velocimetry. We find hydrogen dissociation fraction to be 0.33 and 0.5 if peak or average velocities and temperatures are chosen.

## ACKNOWLEDGMENTS

This work was supported by AFOSR and by DARPA through a contract with the Naval Research Laboratory. One of the authors (W.J.) is supported by the Universität Heidelberg through Landesgraduiertenförderung. The authors thank Ingrid Wysong at the Air Force Philips Laboratory for pointing out the importance of the directed velocity for the power balance, Elizabeth Brinkmann for some early measurements in the arcjet, James Butler and Daniel Vestyck, Jr. for the SEM and Raman measurements, and Mark Cappelli and Michael Loh at Stanford University for loan of the dc arcjet diamond growth technology.

- <sup>1</sup>D. G. Goodwin and J. E. Butler, in *Handbook of Industrial Diamond and Diamond Films*, edited by M. Prelas, G. Popovici, and L. K. Bigelow (Dekker, 1997).
- <sup>2</sup>J. C. Angus, Y. Wang, and M. Sunkara, *Annu. Rev. Mater. Sci.* **21**, 221 (1991).
- <sup>3</sup>M. Frenklach and H. Wang, *Phys. Rev. B* **43**, 1520 (1991).
- <sup>4</sup>M. Frenklach, *J. Chem. Phys.* **97**, 5794 (1992).
- <sup>5</sup>J. E. Butler and R. L. Woodin, *Philos. Trans. R. Soc. London* **342**, 209 (1993).
- <sup>6</sup>S. J. Harris and D. G. Goodwin, *J. Phys. Chem.* **97**, 23 (1993).
- <sup>7</sup>K. E. Spear and M. Frenklach, *J. Am. Ceram. Soc.* **72**, 171 (1994).
- <sup>8</sup>D. G. Goodwin, *J. Appl. Phys.* **74**, 6888 (1993); *J. Appl. Phys.* **74**, 6895 (1993).
- <sup>9</sup>P. K. Bachmann, D. Leers, and H. Lydtin, *Diam. Relat. Mater.* **1**, 1 (1991).
- <sup>10</sup>N. Ohtake and M. Yoshikawa, *J. Electrochem. Soc.* **137**, 717 (1990).

- <sup>11</sup>R. Furukawa, H. Uyama, and O. Matsumoto, *IEEE Trans. Plasma Sci.* **18**, 930 (1990).
- <sup>12</sup>Z. P. Lu, L. Stachowicz, J. Heberlein, and E. Pfender, in *Diamond Materials*, edited by A. J. Purdes, B. M. Meyerson, J. C. Angus, K. E. Spear, R. F. Davis, and M. Yoder (The Electrochemical Society, Pennington, NJ, 1991), Vol. 91-8, pp. 99-105.
- <sup>13</sup>G. P. Smith and J. B. Jeffries, in Ref. 13, pp. 194-201.
- <sup>14</sup>D. G. Goodwin, *Appl. Phys. Lett.* **59**, 277 (1991).
- <sup>15</sup>M. E. Coltrin and D. S. Dandy, *J. Appl. Phys.* **74**, 5803 (1993).
- <sup>16</sup>S. L. Girshick, C. Li, B. W. Yu, and H. Han, *Plasma Chem. Plasma Proc.* **13**, 169 (1993).
- <sup>17</sup>L. Schaefer, C. P. Klages, U. Meier, and K. K. Höinghaus, *Appl. Phys. Lett.* **58**, 571 (1991).
- <sup>18</sup>F. G. Celii and J. E. Butler, *Appl. Phys. Lett.* **54**, 1031 (1989).
- <sup>19</sup>L. L. Connell, J. W. Fleming, H. N. Chu, D. J. Vestyck, Jr., E. Jensen, and J. E. Butler, *J. Appl. Phys.* **78**, 3622 (1995).
- <sup>20</sup>W. L. Hsu, *J. Appl. Phys.* **72**, 3102 (1992).
- <sup>21</sup>W. L. Gardner, *J. Vac. Sci. Technol. A* **14**, 1938 (1996).
- <sup>22</sup>S. J. Harris and A. M. Weiner, *J. Appl. Phys.* **74**, 1022 (1993).
- <sup>23</sup>R. Gat and J. C. Angus, *J. Appl. Phys.* **74**, 5981 (1993).
- <sup>24</sup>J. A. Probst, I. J. Wysong, R. A. Spores, IEPC-95-28, 24th International Electric Propulsion Conference, Moscow, Russia, 19-23 September 1995.
- <sup>25</sup>P. V. Storm and M. A. Capelli, 95-1960, 26th AIAA Plasmadynamics and Laser Conference, 1995.
- <sup>26</sup>J. G. Liebeskind, R. K. Hanson, and M. Capelli, *Appl. Opt.* **32**, 6117 (1993).
- <sup>27</sup>E. A. Brinkman, K. R. Stalder, and J. B. Jeffries, *J. Appl. Phys.* **81**, 1093 (1997).
- <sup>28</sup>M. P. Lee, B. K. McMillen, and R. K. Hanson, *Appl. Opt.* **32**, 5379 (1993).
- <sup>29</sup>J. H. Reisel and N. M. Laurendeau, *Combust. Sci. Technol.* **98**, 137 (1994).
- <sup>30</sup>J. Luque, W. Juchmann, and J. B. Jeffries, paper 96F-065, Fall Meeting of the Western States Section Combustion Institute, Los Angeles, CA, Nov. 1996.
- <sup>31</sup>J. Luque, W. Juchmann, and J. B. Jeffries, *Appl. Opt.* (in press, 1997).
- <sup>32</sup>P. V. Storm and M. A. Capelli, *Appl. Opt.* **35**, 4913 (1996).
- <sup>33</sup>M. H. Loh and M. A. Capelli, 92-3534, 28th AIAA Joint Propulsion Conference, Nashville, TN, 1992.

AIR FORCE OFFICE OF SCIENTIFIC  
RESEARCH (AFOSR)  
NOTICE OF TRANSMITTAL TO DTIC. THIS  
TECHNICAL REPORT HAS BEEN REVIEWED  
AND IS APPROVED FOR PUBLIC RELEASE  
IWA AFR 190-12. DISTRIBUTION IS  
UNLIMITED.  
YONNE MASON  
STINFO PROGRAM MANAGER